OCTOBER 1961

VOLUME 13 (1961) No. 3

GREGG M. SINCLAIR LIBRARY
UNIVERSITY OF HAWAII
8-7-63

NUCLEAR INSTRUMENTS & METHODS

A JOURNAL ON ACCELERATORS, INSTRUMENTATION AND TECHNIQUES IN NUCLEAR PHYSICS

EDITOR: K. SIEGBAHN - UPPSALA

LAST NUMBER OF THIS VOLUME

CONTENTS

H. W. WILSON, R. MUNRO, R. W. D. HARDY and N. R. DALY, A two stage mass spectrometer for nuclear physics applications 269

S. GORODETZKY, A. MUSER, J. ZEN et R. ARMBRUSTER, Sur un circuit rapide de mise en forme à seuil règlable utilisant des diodes tunnel 282

L. JARCZYK, H. KNOEPFEL, J. LANG, R. MÜLLER and W. WÖLFLI, The nuclear reactor as a high intensity source for discrete gamma rays up to 11 MeV 287

H. U. GERSCH, Berechnung der Polschuhoberflächen eines magnetischen Teilchenspektrometers 297

R. CEDARLUND, A. HORN and M. SCOLNICK, Solid-state detector for monitoring 14-MeV neutron production 305

C. W. PETERS and A. L. SNYDER, Optimum location of BF_3 counters in a neutron moderator 309

F. W. K. FIRK, G. G. SLAUGHTER and R. J. GINTHER, An improved Li^6-loaded glass scintillator for neutron detection 313

D. R. SWEETMAN, The achievement of very high pumping speeds in the ultra-high vacuum region 317

GURBAX SINGH and N. K. SAHA, A new design of a multiple-wire spark counter and some studies with the single wire-plate spark counter 321

G. J. SPROKEL, An automatic sample changer 330

A. SEPTIER et J. VAN ACKER, Les lentilles quadrupolaires électrostatiques 335

ECKART MATTHIAS and TORSTEN LINDQVIST, Precision measurements of nuclear *g*-factors by the time-to-pulse-height converter method 356

J. R. ERSKINE and C. P. BROWNE, Inexpensive target chamber with port movable through zero degrees under vacuum 359

Author Index 361

Subject Index 363

NORTH-HOLLAND PUBLISHING COMPANY — AMSTERDAM

NUCLEAR INSTRUMENTS AND METHODS

A journal on accelerators, instrumentation and techniques in nuclear physics

EDITOR: K. SIEGBAHN, UPPSALA

EDITORIAL BOARD:

J. B. ADAMS (CERN)
F. A. ALSINA (Buenos Aires)
E. AMALDI (Rome)
H. L. ANDERSON (Chicago)
K. T. BAINBRIDGE (Cambridge Mass.)
P. R. BELL (Oak Ridge)
R. E. BELL (Montreal)
A. BERTHELOT (Saclay)
H. BRINKMAN (Groningen)
E. H. COOKE-YARBOROUGH (Harwell)
S. DE BENEDETTI (Pittsburgh)
M. DE HEMPTINNE (Louvain)
A. DE-SHALIT (Rehovoth)
M. DEUTSCH (Cambridge Mass.)
S. DU TOIT (Pretoria)
B. S. DŽELEPOV (Leningrad)
W. GENTNER (Heidelberg)
P. C. GUGELOT (Amsterdam)
H. HALBAN (Paris)
O. HAXEL (Heidelberg)
P. HUBER (Basel)
S. KIKUCHI (Tokyo)
J. KOCH (Copenhagen)
M. S. KOZODAEV (Moscow)
S. LIVINGSTON (Cambridge Mass.)
E. M. MCMILLAN (Berkeley)
M. G. MEŠČERJAKOW (Moscow)
P. B. MOON (Birmingham)
M. L. OLIPHANT (Canberra)
W. PAUL (Bonn)
A. S. RAO (Bombay)
G. SALVINI (Rome)
P. SAVIĆ (Belgrade)
P. SCHERRER (Zürich)
CH. SCHMELZER (CERN)
R. TANGEN (Oslo)
D. TAYLOR (Northampton)
V. I. VEKSLER (Moscow)
G. VON DARDEL (CERN)
O. WERNHOLM (Stockholm)
R. R. WILSON (Cornell)
S. D. WINTER (Saclay)

INSTRUCTIONS FOR CONTRIBUTORS

Contributions may be sent to the Editor, Professor K. Siegbahn, Institute of Physics, University of Uppsala, Sweden, either directly or through the intermediation of one of the members of the Editorial Board. Contributions may be written in English, French or German but should always, except for very short papers, be supplied with a brief abstract in English. Figures should be in inked original drawings or glossy prints and they should be sufficiently large. Contributors should make sure that important details in drawings and photographs will show up clearly in the diminished copy used by the publisher.

Books for review should be sent to Professor Siegbahn.

Objective and descriptive material on endeavours and product developments from the industry for the section "Spotlight on Industry" should be sent directly to the publishers, North-Holland Publishing Company, P.O. Box 103, Amsterdam.

Nuclear Instruments and Methods is published monthly. The subscription price of a volume of 360 pages is $ 17.00 (130s), postage free.

Subscriptions should be sent to the publishers, North-Holland Publishing Company, P.O. Box 103, Amsterdam, or to any subscription-agent.

No part of this issue may be reproduced in any form, by print, photoprint, microfilm or any other means without written permission from the publisher.

THE HEART OF AN ACCELERATOR IS ITS ION SOURCE

The old complaint, "I can put a lot of current in, but it doesn't come through the accelerator," is becoming all too common. Gas economy, high beam current-density, and careful attention to little details make a BIG DIFFERENCE.

Ion Sources
ORTEC sources are factory-tested for high output, gas economy and discharge purity. Performance data accompany each unit. 800 μa of 90% protons or 400 μa of helium ions obtained from standard source.

Magnet Coil and Power Supply
By conserving electrons, the magnet intensifies the discharge in the extraction region.

Extractor Voltage Supply
Compact, reliable supply with 5 Kv.—20 ma. output.

R. F. Oscillator and Power Supply
Carefully matched for optimum ion density in extraction region.

Available separately, or as a complete terminal assembly, the components shown above are matched together to perform reliably in this most critical service.

ORTEC

For further information write to:

OAK RIDGE TECHNICAL ENTERPRISES CORPORATION

P. O. Box 485 Oak Ridge, Tennessee
Phone 483-8455, Area Code 615

NC-1B

SCINTILLATION COUNTING

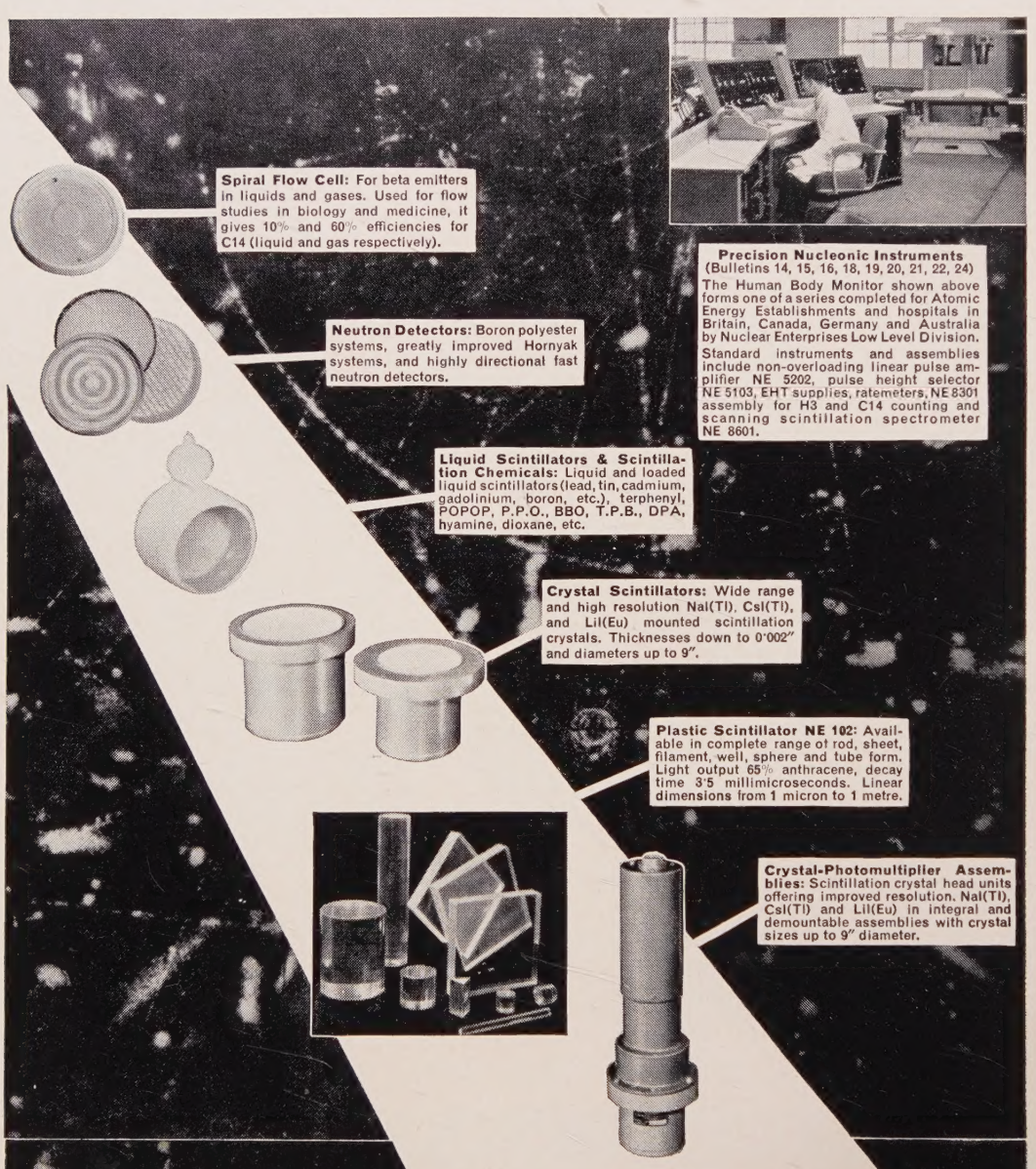

Spiral Flow Cell: For beta emitters in liquids and gases. Used for flow studies in biology and medicine, it gives 10% and 60% efficiencies for C14 (liquid and gas respectively).

Neutron Detectors: Boron polyester systems, greatly improved Hornyak systems, and highly directional fast neutron detectors.

Liquid Scintillators & Scintillation Chemicals: Liquid and loaded liquid scintillators (lead, tin, cadmium, gadolinium, boron, etc.), terphenyl, POPOP, P.P.O., BBO, T.P.B., DPA, hyamine, dioxane, etc.

Crystal Scintillators: Wide range and high resolution NaI(Tl), CsI(Tl), and LiI(Eu) mounted scintillation crystals. Thicknesses down to 0·002" and diameters up to 9".

Plastic Scintillator NE 102: Available in complete range of rod, sheet, filament, well, sphere and tube form. Light output 65% anthracene, decay time 3·5 millimicroseconds. Linear dimensions from 1 micron to 1 metre.

Crystal-Photomultiplier Assemblies: Scintillation crystal head units offering improved resolution. NaI(Tl), CsI(Tl) and LiI(Eu) in integral and demountable assemblies with crystal sizes up to 9" diameter.

Precision Nucleonic Instruments (Bulletins 14, 15, 16, 18, 19, 20, 21, 22, 24)

The Human Body Monitor shown above forms one of a series completed for Atomic Energy Establishments and hospitals in Britain, Canada, Germany and Australia by Nuclear Enterprises Low Level Division.

Standard instruments and assemblies include non-overloading linear pulse amplifier NE 5202, pulse height selector NE 5103, EHT supplies, ratemeters, NE 8301 assembly for H3 and C14 counting and scanning scintillation spectrometer NE 8601.

SCINTILLATORS

The unique scintillation service afforded by Nuclear Enterprises (G.B.) Ltd. includes the highly efficient NE 102 plastic scintillator, liquid scintillators, neutron detectors, scintillation chemicals and an extensive range of crystals & crystal-photomultiplier assemblies.

New:

NE 150 plastic phosphor for pulse shape discrimination techniques and NE 160 a special high temperature plastic scintillator.

For full details write for Technical Bulletins (Nos. 9, 11, 12, 13, 23, and 25) and Catalogue to the Sales Division.

*Write for **NEW** 56 page 1961/62 Catalogue.*

Nuclear Enterprises (G.B.) Ltd

Sighthill, Edinburgh 11, Scotland. Tel: Craiglockhart 5262

Associate Company: Nuclear Enterprises Ltd., 550 Berry St., Winnipeg, 21, Canada.

*What's good for nuclides in New Haven is good for those in New Zealand**

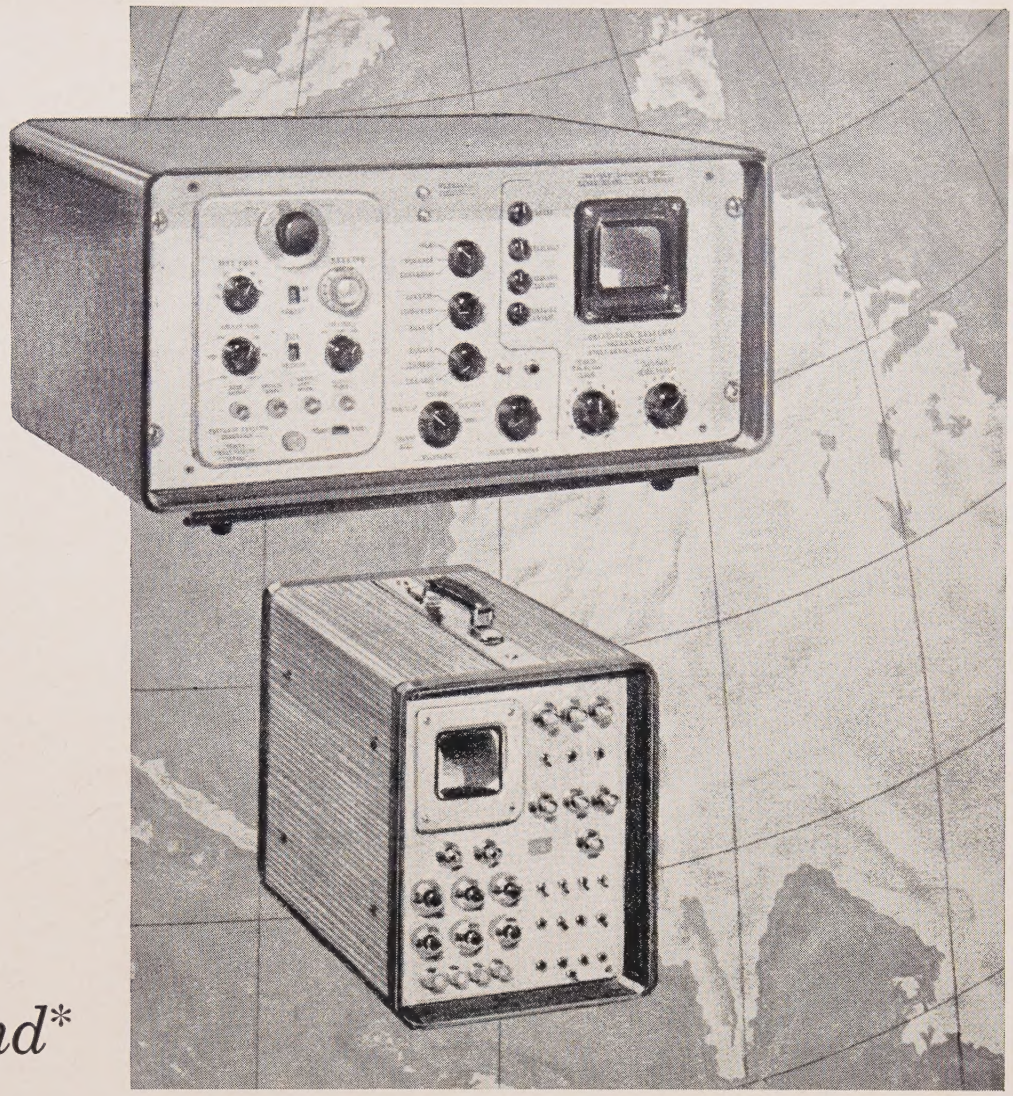

We think the reason people all over the world buy TMC pulse analyzers is pretty much the same reason they're widely purchased and used here: competently designed, bug-free circuits . . . straightforward operation with the same performance and stability today as yesterday . . . easy access to sub-assemblies and uncomplicated servicing if needed. Another way of putting it is the instruments give the user the information he wants in *his* work — with predictable behavior—regardless of where his site, lab or plant may be located. Here are two current examples:

The TMC CN-110 256 channel analyzer offers 7 interchangeable plug-in logics, including pulse height, time of flight, pulsed neutron, multiscaler, mass spectrometer, and coincidence pair. This widely used and thoroughly proven analyzer (over 100 units have been delivered) employs all-transistorized circuitry. Analog, binary, octal and decimal readout may be used. Data can be recorded on strip chart or X-Y recorders, printed paper tape, punched paper tape, or punched cards.

The Model 404 is a compact, 400-channel analyzer you can use anywhere there's a wall outlet and one square foot to put it down. It has a magnetic core memory that can be used in sub groups of two or four; four separate inputs and associated amplifiers; internal pulse routing circuitry; pushbutton data transfer and display overlap; power requirement of *only 25 watts*, and many "system" advantages. While its versatility is a little less than the CN-110's, so are its size, price and purpose quite different from the 110's. Each does its *own* job well.

**Also wherever TMC Pulse Analyzers are used... in Canada, Brazil, Australia, Japan, Yugoslavia, France, Italy, Germany, Belgium, Sweden, Denmark, Switzerland, Israel, Formosa . . . as well as the United States.*

WRITE FOR LITERATURE.

TMC **TECHNICAL MEASUREMENT CORPORATION**

441 WASHINGTON AVE., NORTH HAVEN, CONN. • CE 9-2501

AEI INSTRUMENTATION INFORMATION SERVICE

Transistorized....
4-5 litre ionization chamber
AEI GAMMA MONITORS

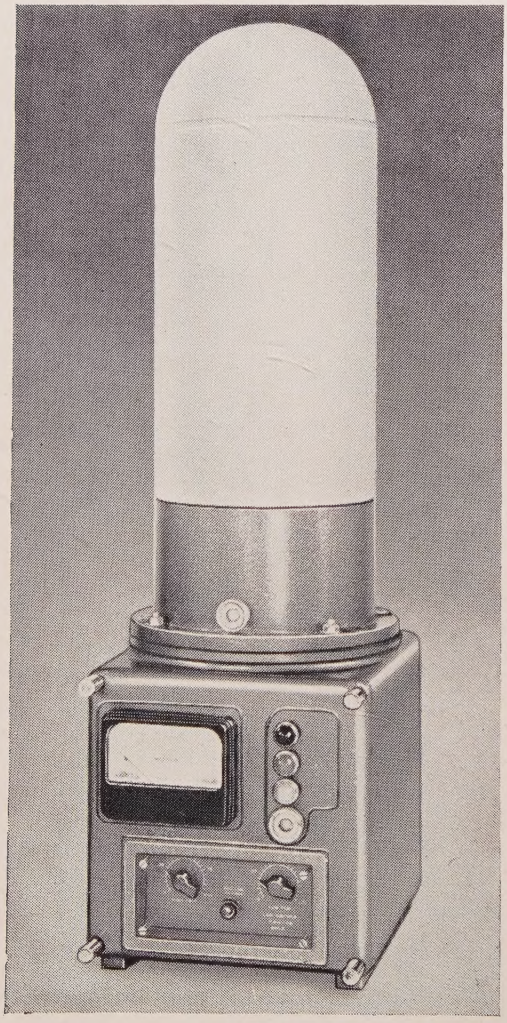

Designed for area radiation monitoring, the type GM2 logarithmic gamma monitor has a 5-decade scale with a maximum sensitivity of 100μ R/hr. The large and sensitive ionization chamber is filed with argon/air to ensure optimum flatness of gamma energy responce. Circuitry is transistorized apart from the electrometer input stage which is used as a cathode follower feeding directly into a negative feedback amplifier to obtain maximum stability. An instrument failure alarm is incorporated and over-rides the trips to prevent spurious radiation alarms. Also available as a linear monitor type GM1.

Full details of types GM1 and GM2 monitors are given in Publication 2454-1 available from
AEI Instrumentation Division,
Process Control Department,
P.O. Box One, Harlow, Essex, England.

◀ GM2 logarithmic gamma monitor with ion chamber mounted on the splash proof case ; it can also be mounted remotely.

AEI | Instrumentation Division
Associated Electrical Industries Limited

SC/136

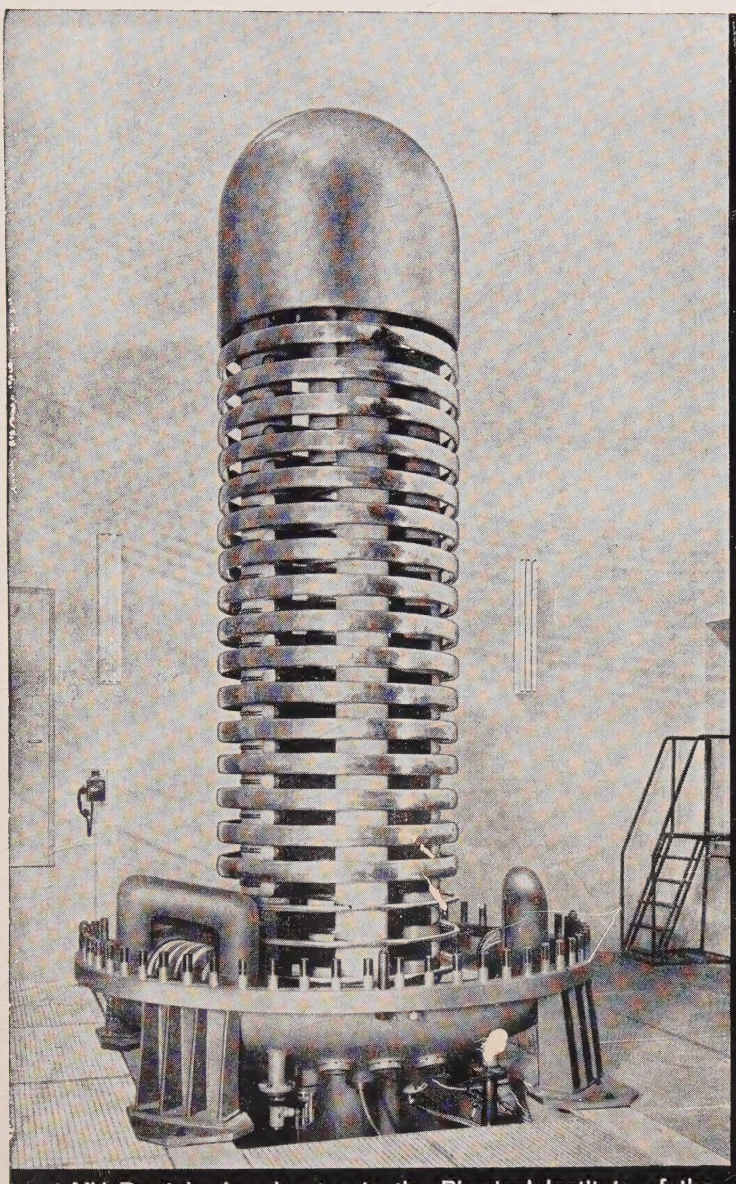

4 MV Particle Accelerator in the Physical Institute of the University of Basel (Switzerland)

HAEFELY

Particle Accelerators
up to 4 MV
with high beam intensity

for basic nuclear research

for industrial radiation processing

Continuous irradiation of plastics

Sterilisation of drugs and preservation of foods

X-ray equipment for non-destructive product inspection

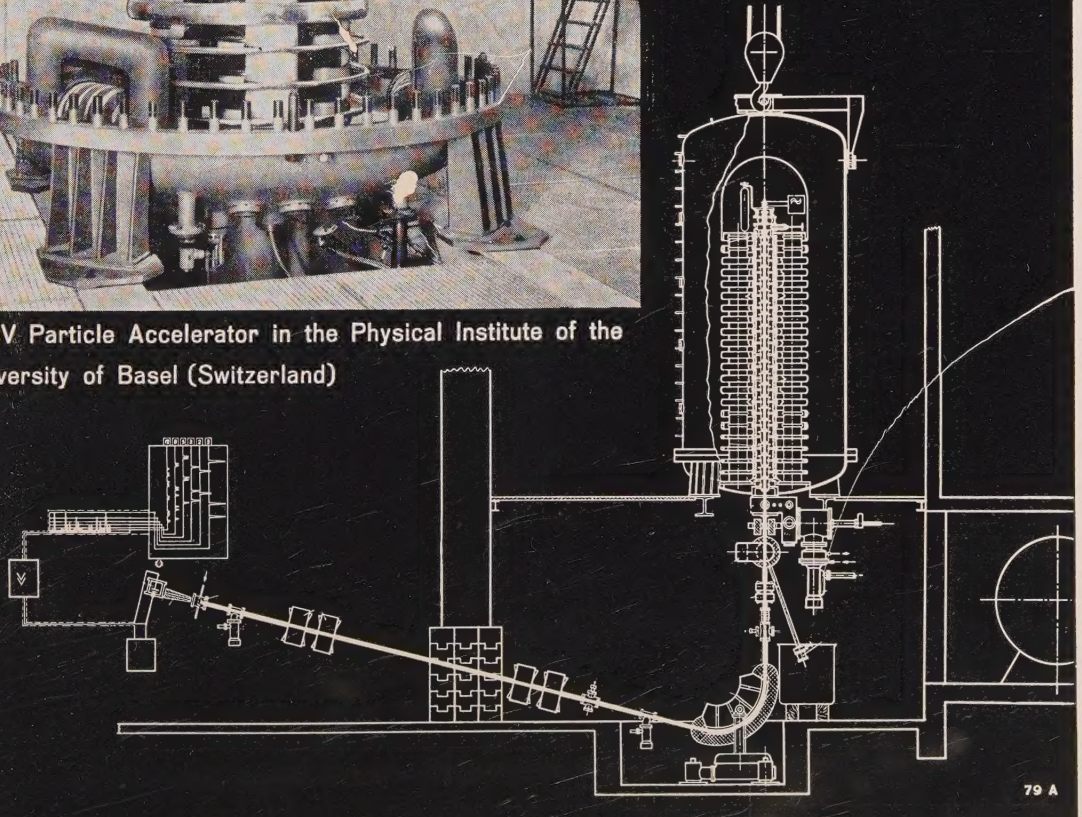

79 A

EMILE HAEFELY & CO LTD BASEL-SWITZERLAND

MODEL 412 MERCURY RELAY

PRECISION SLIDING PULSER

for Precise Calibration of Single & Multi-Channel Pulse Height Analyzers

Determines Window Widths Using Principle of *Constant Angular Velocity*

AUTOMATICALLY
10 × more accurately
40 × faster than conventional pulsers

Incorporates Both Manual Control and Precision Motor Drive

Simulates Pulses from Scintillation, Proportional or Geiger Counters

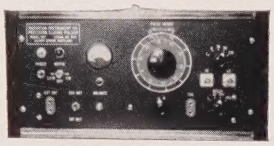

MERCURY PULSER, Model 401

Featuring Versatility and Precision

Specifically designed for the Nuclear Physics Laboratory

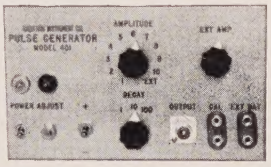

Fast rise and exponential decay simulates scintillation, proportional or geiger counter pulses for test and calibration of amplifiers, pulse height analyzers, scalers, etc.

MODEL 412 . . . $ 450.00 — MODEL 401 . . . $ 125.00

RADIATION INSTRUMENT CO.

P. O. BOX 733, SILVER SPRING, MARYLAND, U.S.A.

NORTH-HOLLAND BOOKS

Paul Ehrenfest

COLLECTED SCIENTIFIC PAPERS

XII + 632 pages

Guilders 45,00 (90s.)

This volume makes widely scattered publications readily available. All Dutch articles appear here in English; the German publications are in the original language.

Sole Agency for U.S.A.:

Interscience Publishers Inc. — New York

NORTH-HOLLAND PUBLISHING COMPANY - AMSTERDAM

NORTH-HOLLAND BOOKS

Imperfections in Crystals

by H. G. VAN BUEREN, *Philips Laboratories, Eindhoven*

CONTENTS

Part I: General properties of lattice imperfections

Part II: Imperfections in metals

Part III: Imperfections in non-metallic crystals

Just out second revised edition

XVIII + 675 PAGES, NUMEROUS PHOTOGRAPHS - GUILDERS 55.— (10 S.)

ASK YOUR BOOKSELLER OR:

NORTH-HOLLAND PUBLISHING COMPANY - AMSTERDAM

SOLE DISTRIBUTION IN U.S.A.: INTERSCIENCE PUBLISHERS INC. - NEW YORK

600 kV Generator

Research Centres and Industry alike find the modern, polished solution to the problem of continued high voltage in the

SAMES ELECTROSTATIC GENERATOR

Electrostatic Painting with the STATRON

HIGH VOLTAGE GENERATORS

* 50 kV to 600 kV
* 20 W to 3 kW
* Positive or negative polarity
* Medium or high stability for
* Electrostatic precipitation
* Electrical testing
* Electronic optics
* X-rays
* Nuclear Physis, etc.

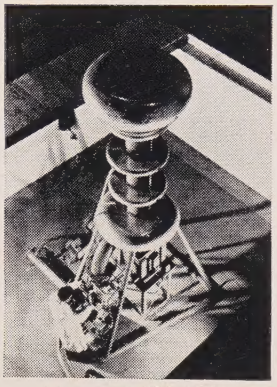

Vertical 600 kV
Accelerator at the Centre d'Etudes Nucléaires de Grenoble

ELECTROSTATIC PAINTING

The STATRON is a portable equipment for electrostatic painting, featuring

* 90 kV voltage
* Complete safety, owing to use of electrostatic generator.
* Paint output: 15 litres/hour
* Supply: 110 or 220 V, single phase.
* Consumption: 110 Watts

PARTICLE ACCELERATORS

Type	Acceleration Voltage	Particles Accelerated	Application
J	150 kV	ions	Neutron Generator by D/T or D/D reaction
L	300 kV	ions	
S	600 kV	ions or electrons	All applications

SOCIETE ANONYME DE MACHINES ELECTROSTATIQUES

21, RUE JEAN MACÉ, P.O. BOX 150, TEL: 44.77.64 GRENOBLE, FRANCE

REPRESENTATIVES

GENERATORS AND ACCELERATORS

Austria: AUSTRONIK, Salzburg – Belgium: CENTRONICS, Brussels – Chinese People's Republic: Cie OLIVIER, Paris – Denmark: DANSK SCIENTA, Copenhagen – Great Britain: MILES HIVOLT LTD., Shoreham by Sea – Italy: SECI, Milan – Netherlands: PROJECTO, Amsterdam – Norway: LEHMKUHL, Oslo – Portugal: A.G.M.E., Lisbon – Spain: CRESA, Barcelona – Sweden: SCIENTA SCANDIA, Gothenburg – Switzerland: OMNIRAY, Zurich – Western Germany: DR. NAMUR, Darmstadt – Bulgaria, Czechoslovakia, Eastern Germany, Hungary, Poland, Rumania, U.S.S.R.: CIFAL, Paris.

ELECTROSTATIC PAINTING EQUIPMENT

Algeria: FAMPA, Algiers – Austria: PETER PETERSEN, Vienna – Belgium: DURMECO, Brussels – Chinese People's Republic: Cie OLIVIER, Paris – Denmark: DANKS SCIENTA, Copenhagen – Eire: HODGES & SONS, Dublin – Great Britain: AEROSTYLE LDT., London – Italy: TRASMETAL, Milan – Netherlands: STUURMAN, Wormerveer – Norway: LEHMKUHL, Oslo – Portugal, RAMADA, Ovar – Spain: INSTITUTO ELECTROQUIMICO, Barcelona – Sweden: SCIENTA SCANDIA, Gothenburg – Switzerland: REGSA, Lausanne – Western Germany: A. WIRTH, Reutlingen – Bulgaria, Czechoslovakia, Eastern Germany, Hungary, Poland, Rumania, U.S.S.R.: CIFAL, Paris.

High Voltage Engineering Corporation . . .

"CHARGED PARTICLES"

Nuclear Radiations and Materials Evaluation

Chemists and metallurgists have been quick to adopt experimental techniques first used for fundamental nuclear physics research. Today, they are exploiting the characteristics of intense ion beams and neutron fluxes for applied research, engineering and analysis. Already, important results have been obtained using nuclear radiations for trace analysis, wear studies, semiconductor modification and similar applications where interactions of positive ions or neutrons create desired, predictable and measurable effects.

Although a number of positive-ion accelerators have been installed specifically for this kind of developmental work, we believe that the use of particle beams for *materials evaluation* is just getting started, and that many programs are dormant because of the cost and skill-requirement of owning and operating an accelerator facility.

Ion Beams and Neutrons for Hire

We think we have an answer to this problem for those who wish to explore activation analysis or research involving accelerated positive ions or neutrons. Here in Burlington, we have a fully-equipped and expertly-staffed *Positive Ion Service Facility*, employing a 2-Mev Van de Graaff accelerator and neutron source as the central research instrument. *Both the facility and the assistance of the staff are now available for independent research and analyses by outside organizations on a rental or contract basis.*

The Van de Graaff is our Model AN-2000. It offers 0.3 to 2.0 Mev hydrogen or deuterium ion beams with currents up to 100 microamperes in continuous or pulsed operation. A 90° mass analyzing magnet and feedback system stabilizes the voltage. A large fraction of the accelerated ion beam is emitted with a homogeneity within 1 part per 1000 for monoenergetic neutron experiments.

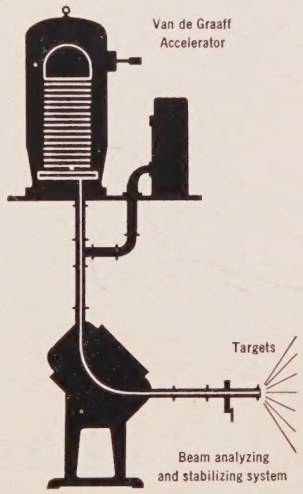

The facility is fully instrumented, including a 200-channel pulse height analyzer for scintillation spectrometry and decay-scheme studies, a remotely-operated sample changer, and neutron moderator.

You may want to use the facility to carry out specific analyses . . . or investigate the feasibility of a certain technique . . . or solve a knotty materials-evaluation problem. Other research possibilities are: *particle interactions; neutron-induced reactions; production of short-lived isotopes; instrument calibration; environmental research; radiation damage and shielding parameters; solid state surface studies; radiobiology.*

Users plan and evaluate all work. We provide an operator. If it bothers you to carry out what may be proprietary development programs in somebody else's house, have no fear. If the use of accelerators is encouraged, we are content. You may draw the shades tightly on any techniques used, and, of course, the results are strictly your own business. If, however, you would like to take advantage of some knowledge we have, a staff physicist is on hand to help.

If the requirement is perfectly straightforward, such as routine analysis, ship us the sample, and we'll do the work. We will supply cost estimates for any program contemplated on a project or continuous use basis. For more information, write for our Bulletin N-1.

Reaction	Neutron Energy (Mev)	Neutron Yield (n/sec)
D-D	1.5-6*	5×10^9
D-Be	0.6-5†	4×10^{10}
D-T	14-15*	5×10^8

*monergic †polyergic

Neutron Yield From 2-Mev Van de Graaff

Of course, if the rentee gets carried away with the possibilities of this work and wants to buy an accelerator, that's all right. Van de Graaffs are available from 0.4 to 4 Mev, producing up to 400 microamperes of current for monoenergetic neutron production. For really high neutron fluxes, the microwave linear accelerator excels. We can recommend a package of suitable instrumentation and would be glad to give counsel on installation and shielding.

HIGH VOLTAGE ENGINEERING CORPORATION
BURLINGTON, MASSACHUSETTS, U.S.A.
•
APPLIED RADIATION CORPORATION
•
HIGH VOLTAGE ENGINEERING (EUROPA) N.V.

NUCLEAR INSTRUMENTS AND METHODS **13** (1961) 269–281; NORTH-HOLLAND PUBLISHING CO.

A TWO STAGE MASS SPECTROMETER FOR NUCLEAR PHYSICS APPLICATIONS

H. W. WILSON, R. MUNRO, R. W. D. HARDY and N. R. DALY

Atomic Weapons Research Establishment, Aldermaston, Berkshire, England

Received 29 July 1961

The design of the mass spectrometer described in this paper makes it very useful in a number of nuclear physics applications. Two 90° magnetic stages, each of 15″ radius, are used together with an accelerating voltage of 15kV. Scanning is by variation of the accelerating potential, the magnetic fields being held constant to one part in 10^5 by nuclear magnetic resonance. Organic materials are excluded with consequent reduction in "hydrocarbon" background. The design of the spectrometer is described and the performance discussed. A later paper will describe the electronic side of the machine.

1. Introduction

In the field of isotopic abundance measurements, properties important in a mass spectrometer are adequate resolution, sensitivity, abundance sensitivity (as defined below), freedom from background, accuracy and stability. The order in which these desiderata are placed depends on the particular application of the instrument. In the case of the spectrometer to be described, all were of importance and in the design attention was paid to each.

The spectrometer was designed at the Atomic Weapons Research Establishment and, for the most part, was built there. This paper describes this machine in some detail and includes the results of certain experiments carried out either to test its performance when completed or in the source of subsequent operation. A description of the electronic details is given in another paper[1]).

The spectrometer went into operation at the end of 1957 and has operated satisfactorily since then. In the light of experience certain modifications have been made and these are described briefly under the heading "Later Improvements".

2. The Two Stage Principle

The two stage principle requires the use, in effect, of two mass spectrometers in series[2,3]). This principle was adopted primarily because of the promise which it offered of excellent abundance sensitivity, that is to say, the contribution to the height of a small peak arising from the tail of an adjacent large peak (the "contribution factor") is very small That this promise was fulfilled will be evident from the experimental results quoted later. Here it will suffice to state that, in the tantalum region, the "contribution factor" at one mass away from the main peak is of the order of 2×10^{-7}. This property is important in many aspects of the work for which the machine was designed. One of the principal applications of the spectrometer is the detection and measurement of isotopes of very small abundance, especially those arising from nuclear reactions. Very often the product of such a reaction is radioactive and may be detected by nuclear counting methods but, if it is stable or very long lived, then the use of the two stage principle is extremely valuable.

As has been indicated the height of the small peak to be measured is limited by the tail arising from the supposed adjacent large peak. Assuming that the various aberrations are small (as is the case in this machine) the tail arises principally from gas scattering and from scattering from the tubes, slits and so on. An ion scattered in this manner and passing through the central slit of the spectrometer will not, in general, pass through the final detector slit. Thus, if the contribution factor is $1:x$ after

[1]) W. A. P. Young, D. E. P. Silver and H. W. Wilson, to be published.

[2]) M. G. Inghram and D. C. Hess, described by M. G. Inghram and R. J. Hayden, Mass Spectroscopy. Nuclear Science Series, Report No. **14** (1954) 24.

[3]) F. A. White and T. L. Collins, App. Spec. **8**, No. 4 (1954) 169.

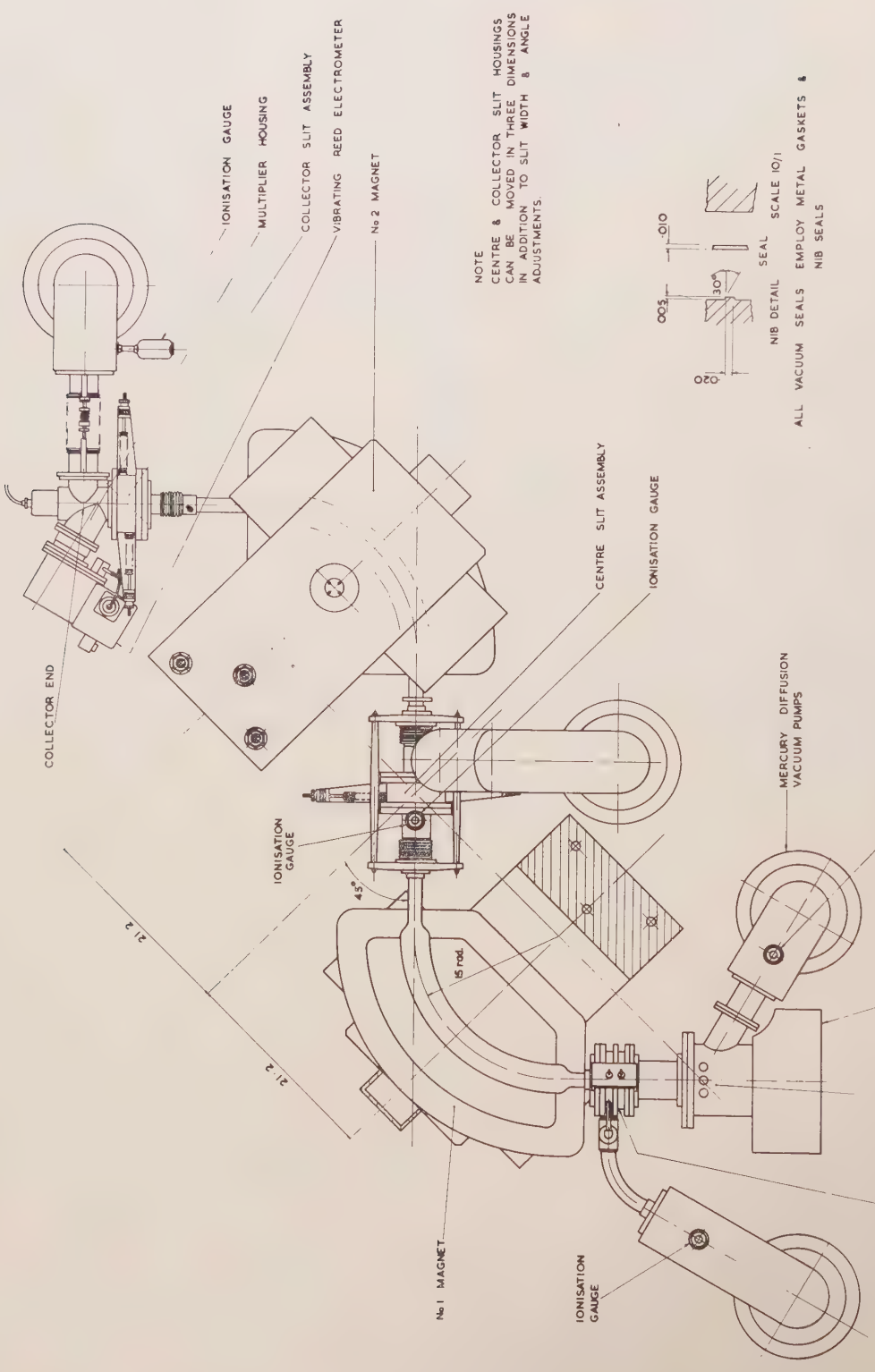

Fig. 1. Layout of mass spectrometer M.S.X. in its original form.

passing through the first stage it should, theoretically at least, be reduced to $\sim 1 \cdot x^2$ after passing through the second stage. Experiments show that the abundance sensitivity is in fact increased by a factor of the order of 1000.

price of a much reduced transmission. In fact, experiments show that the additional loss in passing through the second stage is only of the order of 50%. Compared to the overall efficiency of a typical spectrometer, this loss is unimportant.

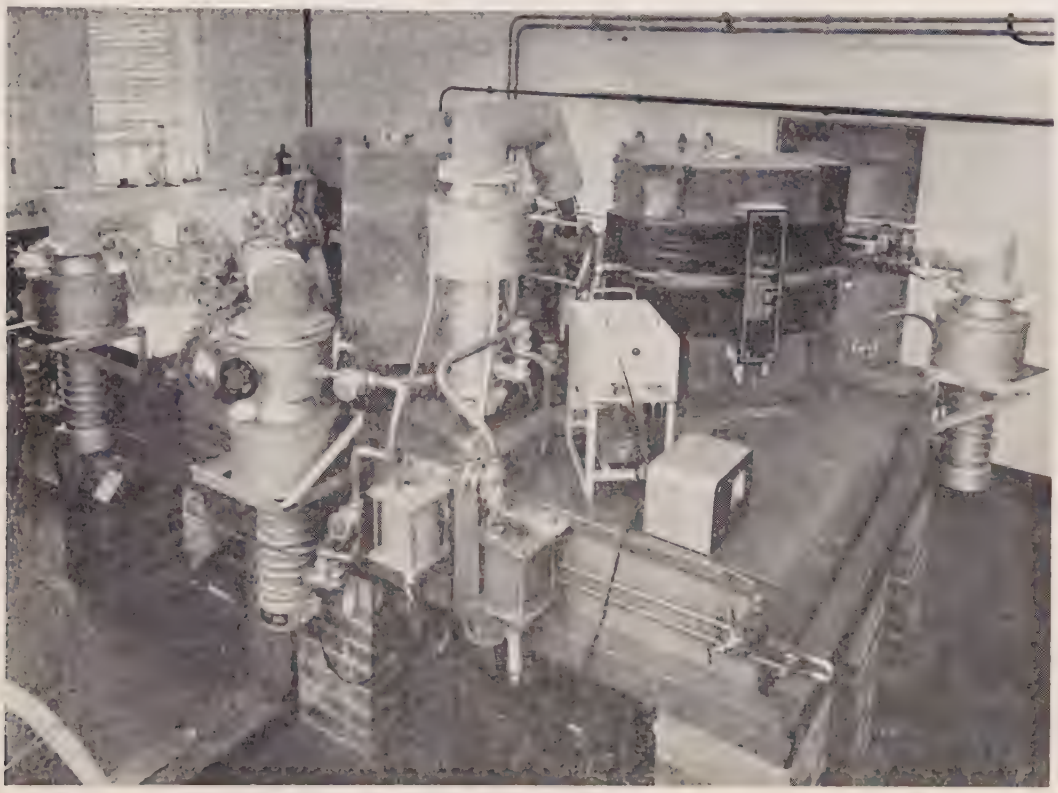

Fig. 2. Photograph of M.S.X.

It might be supposed that an alternative approach would be merely to reduce the pressure in a single stage machine. Apart from the fact that this would not affect the scattering at solid surfaces, it is easy to show that the required improvement in vacuum is considerable. This is due to the slow variation of scattering with pressure[4]). Thus if we assume a linear law, then a reduction by a factor of 10^3 in pressure would be required to achieve the performance of the two stage spectrometer. In fact, such a decrease in pressure would not yield this sensitivity, as scattering at solid surfaces—tube, slit edges and so on—would still limit the performance. It is important to note that the vastly increased abundance sensitivity is not bought at the

3. General Description of the Spectrometer

The lay-out of the machine is shown in fig. 1 and a photograph of it in fig. 2. Ions, accelerated to 15 keV, pass through two magnetic stages each of 15″ radius of curvature and are detected by an electron multiplier. If it is required to measure the beam at the centre, a Faraday bucket collector can be raised to intercept the beam. The principal use of this facility is in the setting up and alignment of the first stage. As no multiplication is involved in the centre collector, it is used only for beams in excess of 10^{-14} amps, whereas the multiplier is capable of detecting single ions.

[4]) F. A. White, T. L. Collins and J. C. Sheffield KAPL-873 10th Dec. 1952 (Appendix by G. M. Roe).

The high vacuum part of the spectrometer is constructed throughout of non-organic materials. This reduces the pressure in the machine and the background which would arise from organic materials. Certain sources of background are also reduced by resolution of the background peaks from those being measured. The spectrometer is normally operated at a resolution of the order of 1200. This is adequate to resolve out the so-called "hydrocarbon" background which sometimes appears at every mass. In this machine it happens, however, that "hydrocarbon" background is rarely present. A more serious source of background, on the other hand, is the existence of peaks at masses 234 and 236 due to the molecules K_6^{39} and $K_5^{39}K_1^{41}$. In most solids machines these peaks interfere with the measurement of small absolute abundances of U^{234} and U^{236}. In this spectrometer, however, these peaks are completely resolved. This resolution is obtained without loss of sensitivity as a result of the use of a fairly large radius (15″) and high accelerating potential (15 kV).

The exclusion of all organic materials from the vacuum system raised problems in the design of an adjustable slit system and of a valve to isolate the source region from the rest of the spectrometer. Details of these are given in a subsequent section.

The whole spectrometer is mounted on a large surface table of area 10 ft × 6 ft which happened to be available at the time. The surface table is mounted on six brick piers and was carefully levelled to ± 0.001″ after being placed in position. It provided a very useful platform on which to build and an accurate datum surface from which to measure. The value of this will be appreciated from the fact that the whole ion path had to be built in one plane to an accuracy of a few thousandths of an inch. The magnets are supported on small upturned surface tables and are moved by floating these tables on a thin film of oil forced under pressure between them and the large surface table as will be described later.

The magnetic fields are controlled by proton resonance to a stability of about one part in 10^5. The 15 kV accelerating potential is stable to about five parts in 10^5 per hour, this stability being necessary when detection is by counting methods rather than by scanning the ion beams across the detector slit. If scanning is employed, detection is by an Applied Physics Coroporation Vibrating Reed Electrometer followed by a Honeywell-Brown $\frac{1}{4}$ sec chart recorder. As the magnets are held to a fixed field by a crystal controlled oscillator, the scanning is accomplished by varying the accelerating potential. Greater sensitivity can, however, be achieved by ions counting methods. In this case the accelerating voltage is held constant so that the ion beam of the mass concerned passes through the detector slit for a fixed period and the individual ions counted by a scaler and recorded by a print out device. At the end of the fixed period (1 sec–1 min) the accelerating voltage switches automatically to the next mass and the ions counted for another predetermined period, not necessarily the same. In this way two, three or four beams can be compared in turn, the cycle being carried out some ten to thirty times. The details of the electronic circuitry involved are given in the paper to which reference has already been made[1]).

4. The Ion Source

The details of the ion source are shown in fig. 3. Essentially of the Nier type, it is very similar to that used by Stevens[5]), to whom we are indebted for its basic design although the method of construction is different. 15 kV acceleration potential is used and the triple filament method of Chupka and Inghram[6]) is generally employed for the analysis of solids. The use of a high accelerating potential is of considerable value, firstly, because of the increased source efficiency which it affords and, less importantly, because of the relatively smaller chromatic aberration arising from the initial finite energy spread of the ions.

The source is constructed in two accurately aligned sections (a) the accelerating section and (b) the collimating section. There is no direct mechanical connection between the two sections, minimising the possibility of H.T. breakdown where the largest voltage drop occurs. We have in fact experienced no difficulty due to electrical breakdown.

[5]) C. M. Stevens, private communication.

[6]) M. G. Inghram and W. A. Chupka, Rev. Sci. Instr. **24** (1953) 518.

All slit plates are made of stainless steel, carefully polished with all edges radiused. Alignment of the plates is by ground quartz rods fitting in jig bored holes. Ground quartz spacers give the necessary separation while temperature resistant particularly in the vertical plane where non-uniformity of emission and filament misalignment can give reduced intensities.

A window at the back of the source provides a means of measuring filament temperature

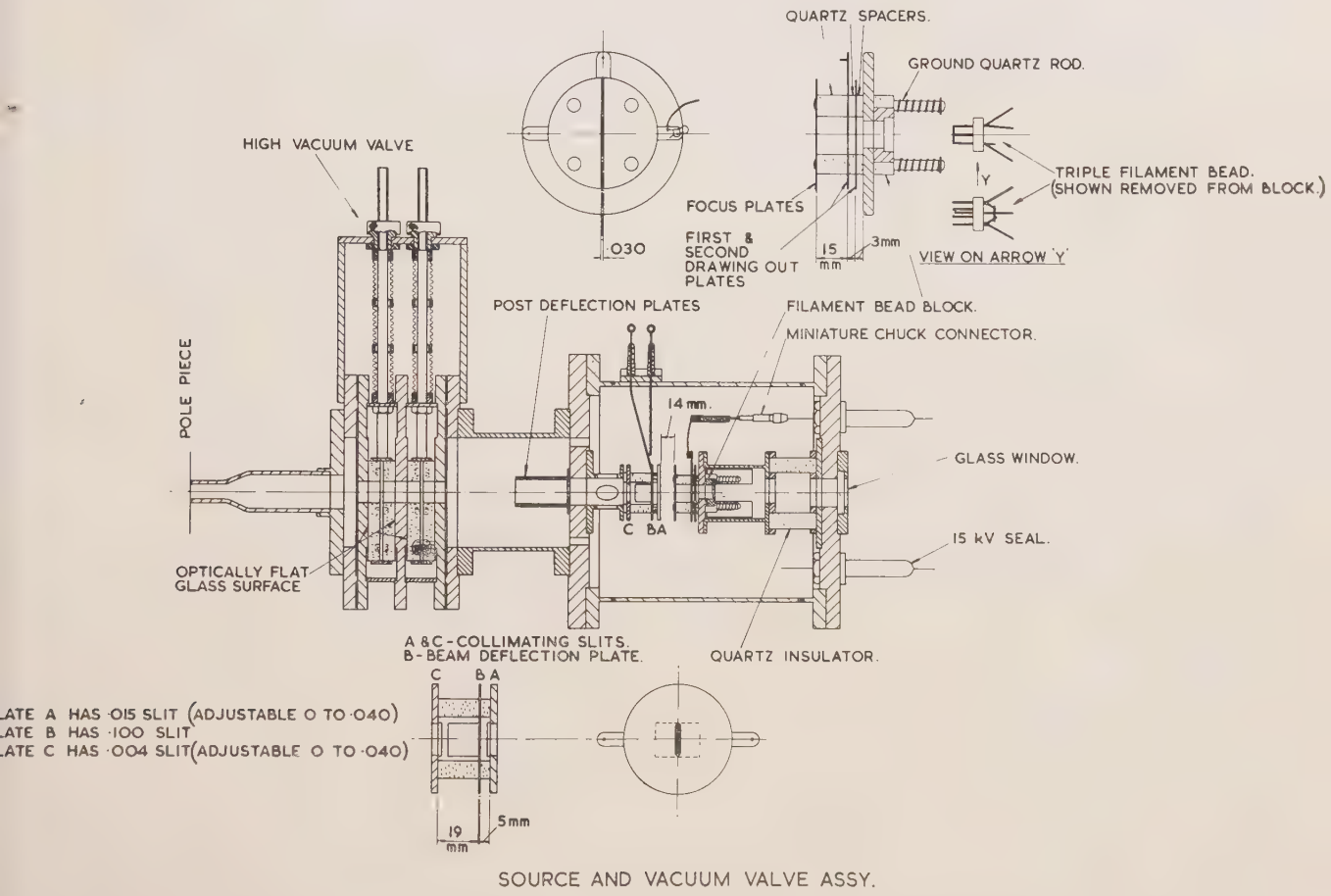

Fig. 3. Diagram of source and valve. Dimensions are in inches except when otherwise indicated.

coiled springs hold the assembly together. The accelerating section is mounted on a rigid platform built up on insulating quartz pillars.

H.T. connections to the source plates are made with copper wire formed into coils to provide flexibility. Glass-Kovar lead-in seals are used.

Beyond the exit collimating slit are four electrodes termed "post deflection plates". These provide beam direction control in the horizontal and vertical planes prior to entering the analyser region. This control has been found most useful, and, in general, of observing the source region.

When changing samples, the whole accelerating section with backing plate is removed. The slit plates with the filament bead and holder are then removed from the insulated platform and replaced by a similar set of slits with a new sample on a fresh bead. The source is thus ready to pump down in several minutes. All slits and spacers near the filament are cleaned after each analysis by boiling in concentrated nitric acid and distilled water.

4.1. THICK LENS SOURCE

A Nier thick-lens source of a similar pattern to that described by Dietz[7]) and employing a single V, or canoe, type surface ionisation filament has also been built and tested. This was constructed in a similar manner to the previous source with accurately ground quartz spacers and rods fitting in jig bored alignment holes. In this case, however, the whole source could be mechanically tilted in the vertical plane about the final collimating slit. This provides an alternative method of tuning for maximum intensity to compensate for nonuniform emission along the length of the filament.

The thick lens source combined with the V-type filament has not given the hoped for increase in sensitivity over the triple filament source though this may be due, in part, to our longer experience of the latter. Preference, at present, has been given to the triple filament method since the sample burn-up is much more controllable. The V-type source would appear to produce slightly less aberration than the triple filament source. The magnitude of the difference however is not considered to be of significant importance in the types of analysis at present being carried out on the machine where sensitivity and abundance sensitivity are the important requirements.

We have also used a variant of the triple filament source in which a somewhat larger central filament is placed parallel to and situated between the side filaments. This permits the comparison of an unknown sample on one side filament with a standard sample on the other by heating the side filaments alternatively. This technique, which will be described separately[8]), appears to give no reduction in sensitivity and possibly a slight gain.

5. The Vacuum System

The design of the vacuum system was based on two criteria: (a) The exclusion of all organic material and (b) the best vacuum obtainable with an unbaked system. Lead or gold gaskets with nib seals are used throughout the whole system which is made entirely of metal and glass and is pumped by four 600 litre/sec mercury diffusion pumps. The backing pump lines are all made of stainless steel and liquid nitrogen traps have been positioned between the backing pumps and the diffusion pumps to minimise possible hydrocarbon background from the pump oil. Magnetic cut-off and air admittance valves in the backing lines reduce the hazard of backing pumps or power failures.

Pressure measurements are made by ionisation gauges at four points in the system and an automatic safety cut-out for the electron multiplier H.T. is coupled to the appropriate collector and gauge. An audio alarm provides a further pressure failure warning.

The pressure of the machine is generally of the order of $1\text{–}3 \times 10^{-7}$ mm Hg.

5.1. VACUUM ISOLATION VALVE

Speed in sample changing and in the subsequent pumping down demands that only the source space should be let up to atmosphere. The gate valve designed to isolate the source from the rest of the spectrometer is constructed entirely of glass and metal (figs. 3, 4). It consists essentially of four optically flat glass plates lightly spring loaded against optically flat stainless steel plates and made to slide by the action of a pusher rod operated through a bellows. In the open position, holes in the glass plate line up with holes in the stainless plates permitting a free path for the ion beam. In the closed position, the holes in the stainless plates are covered by the glass and present a very low conductance path for leakage. Only the three glass plates farthest from the source act in a sealing capacity, the fourth merely providing a balanced sliding system.

The interspace, in which are the two glass sliding plates farthest from the source, is pumped by a diffusion pump which also pumps the analyser tube when the valve is open. The other interspace is connected to the source region by holes through the stainless plate. These open the slider space to atmosphere while the source is being changed. The presence of these holes ensures that the interspace is pumped down simultaneously with the source thus permitting movement of the glass plates without risk of scratching under the pressure loading.

[7]) L. A. Dietz, Rev. Sci. Instr. **30** (1959) 235.
[8]) H. Patterson and H. W. Wilson, to be published.

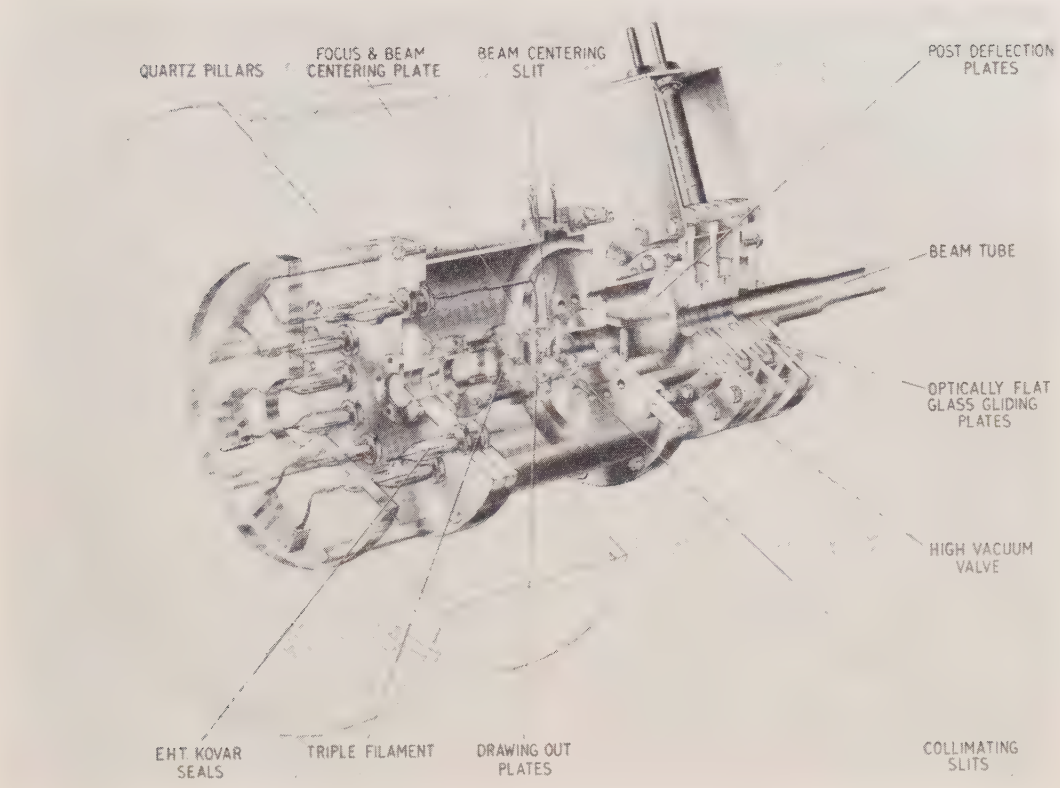

Fig. 4. Perspective view of source and slit.

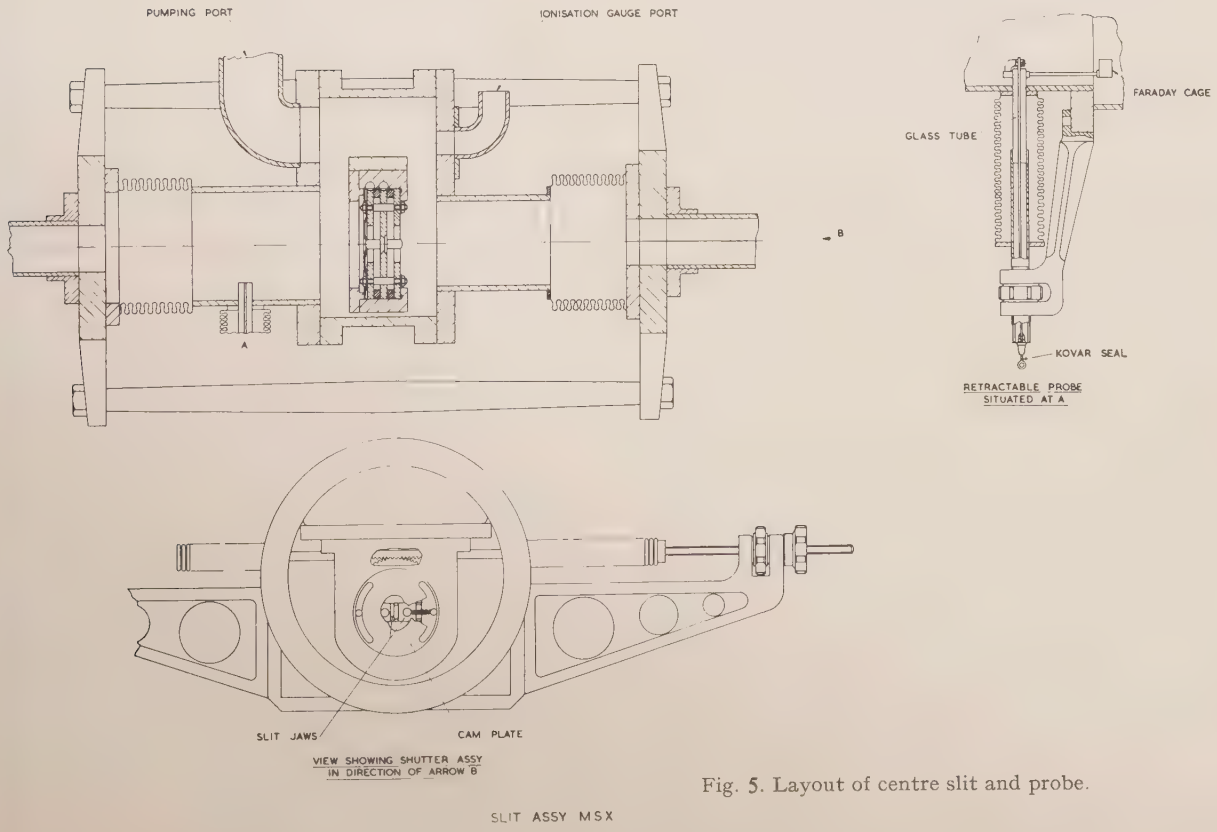

Fig. 5. Layout of centre slit and probe.

A balanced clamping arrangement ensures that the optically flat plates are not distorted under the action of bolt and atmospheric pressure loading.

The valve has been in use for some four years and no less in efficiency has been noted. No pressure rise is observed in the analyser region (at $1–3 \times 10^{-7}$ mm Hg) when the source is opened to atmosphere.

6. Centre and Collector Slit Assemblies

The centre slit and the original collector slit assembly are similar in their internal construction and the layout is shown in fig. 5. Differences in their external arrangement arise from differences in the position of pumping ports and in methods of mounting; also the centre slit is provided with a retractable probe which is shown sectioned on the right of fig. 5 and is described below.

The slits are formed by two similar shutters at the mating edges of which the thickness is reduced to about 0.030″. These shutters are mounted on V slides formed in a disc shaped carrier plate, as shown in the top half of the figure. This plate has gear teeth cut over a 90° arc in its periphery; these engage with a rack which can be moved in the plane of the plate by means of an external hand nut, thus providing angular movement of the slit about the axis of the ion beams. The toothed portion of the rack is split along its length into halves, the free half being moved by the fixed half through compression springs; this being a variant of the usual anti-backlash arrangements used in instrument gears. The slit shutters are fitted with short pegs normal to their plane which are held against equiangular spiral cams, by means of tension springs; these cams are machined in corresponding pairs in two discs of the same diameter as the slit carrier plate, one cam disc having 90° of gear teeth similar to those in the carrier plate engaging with a similar rack. Rotation of the cams discs opens and closes the slit approximately linearly, giving a maximum apterture of the order of 1 mm. The plain cam plate is driven and located in correspondence with the toothed plate, by means of studs passing through circular slots in the carrier plate. The three plates are mounted in a housing contained in a cylindrical casing. The whole assembly is made in stainless steel.

The plain stems of the racks pass through the wall of the casing and are sealed by bronze bellows whose ends are soft soldered to the casing. The entry and exit ports in the end plates of the casing are joined to the ion beam tubes by bellows as is also the pumping port to the large pump duct, so providing limited movement of the whole casing in three dimensions. The motions are provided by three slides at right angles. The ends of the tubes facing the centre slit are braced against atmospheric pressure by four duralumin struts screwed into the arms of two spiders bolted to the connecting flanges on the ends of the tubes.

The drawing is otherwise self explanatory but a detail which may be of interest and perhaps have applications in other fields is the glass tube which insulates and supports the wire connecting the Faraday bucket to the metal to glass seal shown on the right of the drawing. This glass tube is screwed into a hollow stainless steel shank screwed on its outside to take the hand nut controlling the movement. The tube is Pyrex capillary on which a screw thread is cut using a carborundum wheel dressed to the appropriate angle. The thread was taken out in one cut and chased to finished size with a split steel nut charged with silicon carbide powder. It was found that the glass tube could not be located by simply screwing down a lock nut, since there is no elasticity in the system. However, by slotting a $\frac{1}{16}$″ thick stainless steel washer along a radius and giving the lips of the slot a set of the order of 0.010″ this precision spring washer gave sufficiently elasticity to enable the glass tube to be located with a lock nut. The lock nut is not shown in the figure.

The whole collector slit assembly has recently been modified to a considerable extent as described in Section 10 "Later Improvements". However, the centre slit assembly remains unchanged.

7. Magnets

The magnets for the machine were designed to be identical, it being required that they impose a 15″ radius of curvature on the trajectory of singly ionised particles of mass 300 and energy of 15 kV, the change in the direction being 90° at each stage.

The incoming beam was assumed to be 1 cm high

with a horizontal included angle of spread of $\frac{1}{2}°$. Thus a gap of $\frac{3}{4}''$ was chosen as being large enough to give adequate clearance for the ion tube.

The construction of each magnet is quite conventional. The yoke consists of a spine to which two arms are attached by long studs and accurately located by a step in their inside faces. The pole pieces are located in the arms by means of shallow large diameter spigots and held into these by locating screws passing through the arms. The pole pieces and arms were assembled so that the entry and exit faces of the pole pieces lay in the same plane. The whole assembly is shown in fig. 6 and

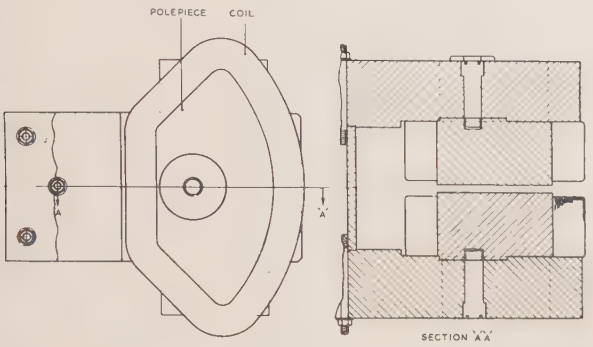

Fig. 6. Magnet design.

was made from Low Moor "Super Hyperm" Iron. The excellent magnetic properties of the iron allowed the flux path to be made much less heavy than would have been possible with mild steel and hence made for greater ease of movement of the entire magnet at the lining up stage.

The horizontal component of this movement was achieved by mounting the magnets on upturned surface plates whose faces had radial grooves machined in them, running to a central oilway, and resting upon a large surface table which served as a mounting platform for the entire machine; by pumping oil under pressure into these grooves the magnets could be raised upon a film of oil and moved very easily, fine adjustment being obtained by jacking screws attached to the base of upturned magnetic chucks. Vertical movement and levelling of the magnet was provided for by screw jacks between the lower faces of the bottom yoke arms and the under side of the inverted surface plates.

The magnets are energised by coils wound from 20 SWG enamelled copper wire. Each pole piece is surrounded by a coil of 11000 turns; each pair of coils has a resistance of the order of 1000 ohms and with a current of 750 mA gives a field of 7400 gauss in the uniform region of the gaps.

8. The Detection System

Since the two stage mass spectrometer was designed to analyse samples as small as 10^{-10} g it was necessary to have a detector capable of measuring currents as low as a few ions per second. For this reason an Allen type electron multiplier was chosen in the first instance. This was replaced later by a scintillation type detector[9]) as will be described in the next section on "Later Improvements".

The multipliers employed were made at Harwell and employed 11 stages of activated beryllium copper dynodes held between two quartz spacer plates. Pins extending from the dynodes fitted into accurately spaced holes in the quartz plates. This gave control both of the curvature and also of the spacing of dynodes. The dynode chain resistors were mounted inside the vacuum and the whole multiplier could be moved inside the bellows in such a way that the ion beam was made to impinge at the maximum gain position on the first dynode.

When new, the gain of these multipliers (which are still used in other machines in the group) is greater than 10^7 but it falls off with time, over many months, to possibly less than 10^5.

Two methods of recording are used. In the first, the current is integrated using a Cary Vibrating Reed Electrometer, the result being displayed on a $\frac{1}{4}$ sec Honeywell-Brown pen recorder. In this case a high load resistor of the order of 10^9 ohms is used at the multiplier output. In the second method ion counting is employed. The ion beam passes into the detector for a predetermined time. The pulses are amplified, passed to a scaler and the total count is recorded on a print out device. The accelerating potential is then switched to permit another mass to pass through the detector slit and counting is started for another, not necessarily equal, predetermined period. This switching, which is carried out automatically, can be extended to measure up

[9]) N. R. Daly, Rev. Sci. Instr. **31** (1960) 264.

to four separate ion beams in sequence, the times of count for each beam being independently adjustable. The circuitry involved will be described in Part II of this paper[1]).

Ion counting offers several advantages. If the total sample size is small, no time is wasted in scanning from one beam to the next, since the switching time is somewhat less than one second. (However it is possible to use switching in conjunction with the integration method.) More important is the fact that the efficiency is considerably higher using counting. In principle 10^4 ions of a small abundance isotope will permit a measurement of its abundance to 1%. However, if the integration method is employed this number of ions is spread over a number of peaks and the accuracy will be considerably less than 1%. In other words, to achieve 1% precision in this case, many ions and, therefore, more sample would be necessary.

The variation in velocity of incident ions of different mass give rise to a corresponding difference in the number of secondary electrons produced per incident ion. The effect of this is to give a mass discrimination when the integrated current method is employed. However this effect can be avoided if the counting method is employed, provided the detector is 100% efficient for ions. If the efficiency is less there will still be a residual effect but it will be considerably less than that associated with the integrated current method. The discrimination is reduced to the same value if the count rate is integrated and displayed on a count rate meter or pen recorder. The scintillation detector which was fitted later has effectively 100% efficiency of detection and thus there is no detection discrimination when the counting technique is employed. There remains, however, a source discrimination due to differing energies of ions of different mass. This is expected on theoretical grounds to be equal to the ratio of the masses measured and experiments support this. If the integrated current method is adopted a further detector discrimination of the same magnitude is also expected. (In the case of magnetic scanning, the value of discrimination is usually taken as the square root of the ratio of the masses, but it is better to measure it.)

9. Performance

9.1. CONTRIBUTION FACTOR

The contribution factor was measured in the tantalum region using a tantalum filament. Whilst Ta^{181} is the principal isotope of tantalum there exists also a very small abundance isotope Ta^{180} to the extent of 0.012%. Thus this small isotope can be used as a ruler to measure the height of the tail

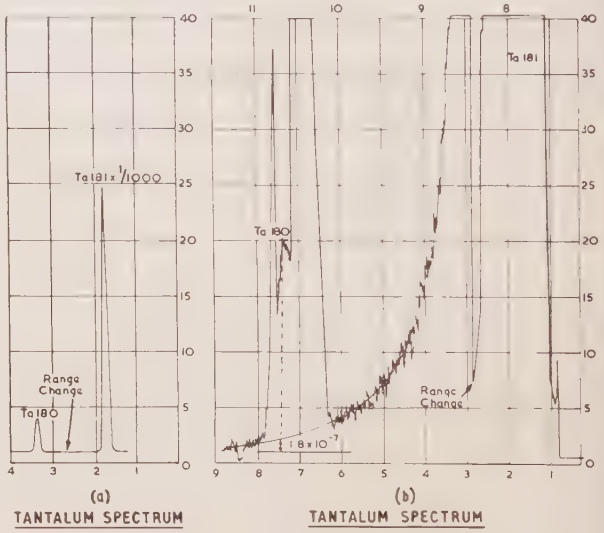

Fig. 7 (a) (b). Ta spectra. The abscissa-axis is marked in minutes

of the Ta^{181} peak at one mass removed. Fig. 7(a) shows a scan of the spectrum done in the normal way and this shows no evidence of a tail whatsoever. In a later experiment, fig. 7(b), the tantalum beam current was increased to such an extent that the mass 180 beam could no longer be recorded. A change to the most sensitive range revealed a tail and by comparison with the Ta^{181} peak height (measured on a less sensitive range) it was deduced that the contribution factor was 1.8×10^{-7}. It is not certain that even this small tail is due entirely to scattered Ta^{181} ions as there may have been a voltage remanence effect in the resistor. A time scale is indicated on the chart. It is not possible, without modification, to scan the spectrum in the opposite direction and thus pass through the small peak first.

The contribution factor has also been measured in the uranium region, using a separated U^{238} sample. In the mass 239 position the contribution arising from the tail of the 238 beam is of the order

of 3×10^{-7}. On the low mass side, however, it is of the order of 10^{-6}. The contribution factor is the limiting factor in the measurement of low abundance isotopes. As a rough rule, provided the height of the peak is of the order of, or greater than, the height of the tail, the contribution factor can be allowed for since it varies in a continuous manner with mass setting. For example, if scanning is employed, one can interpolate a base line under a peak and thus make a fairly reliable measurement. This method, however, is not so easily applied in the counting case although it is still possible to allow for the effect, if appreciable.

9.2. SENSITIVITY

A good deal of experience with the spectrometer shows that if scanning is employed, the results being recorded on a chart recorder, the sensitivity for the smallest isotope of a uranium or plutonium sample is of the order of 10^{-13} g. In fact, the spectrometer appears to be somewhat more sensitive for plutonium than for uranium. If, on the other hand, the counting method is employed and the sensitivity limit is defined as 100 counts total of the smallest isotope present, as suggested by Dietz[10]) then the sensitivity would correspond to a few times 10^{-15} g. Successful analyses have been carried out on samples whose total size was less than 10^{-10} g. Over the range of elements of which we have had experience it would appear that a sample of 1 μgm is, in general, adequate for an analysis. In the case of alkali and alkali earth metals the sensitivity is relatively very high.

The overall efficiency of a mass spectrometer is, in general, rather low. Losses occur in the source, in transmission through the spectrometer and at the detector. The most serious losses occur in the source and work is underway in this laboratory to develop more efficient sources. The detector now used has an efficiency of 100% for detection of a single ion but a further gain could be obtained if it were possible to detect all ions simultaneously. It has not hither to been possible to do this and retain 100% efficiency of ion detection. However the technique of White *et al.*[11]) shows promise in this field.

Measurements show a transmission of 50 % in the source, 17 % in the first stage and 50 % in the second. Most of the overall loss is due to spread in the vertical plane and it is planned to reduce this by z-focussing.

9.3. ABERRATIONS

From the analysis of charts such as that shown in fig. 8, an estimate can be made of the aberrations incurred in passing through the machine. In experiments using a 0.004″ source slit it was found that the width of the image at the detector was of the order of 0.008″ (this is based on a knowledge of the detector slit width). However in an S-shaped two stage machine the dispersion is double that for a single stage spectrometer. Thus the total aberrations add up to the order of 0.004 . These measurewere carried out on both tungsten and barium beams with the above result. The method of making the estimate was to measure the ratio of the width of the rising (or falling) portion of the beam to the total width. This is equal to the ratio of the image width to the sum of the image plus detector slit widths. An alternative method is to compare the rising (or falling) width with the distance between peaks. The two methods gave the same result.

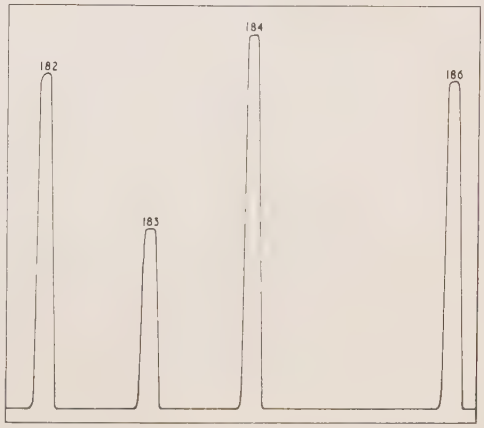

Fig. 8. Tungsten mass spectrum usnig scintillation detector.

9.4. RESOLUTION

The spectrometer is usually operated with a resolution of about 1200 which is adequate to

[10]) L. A. Dietz, Rev. Sci. Instr. **30** (1959) 235.

[11]) F. A. White, F. M. Rourke and J. C. Sheffield, A.S.T.M. Meeting on Mass Spectrometry, 1960 (not published).

resolve the K_6 peaks at masses 234 and 236 referred to earlier. Poorer resolution than this does not increase the sensitivity. In fact the resolution can be increased to ≈ 1800 without loss in sensitivity but in this case the peaks are no longer flat topped. By

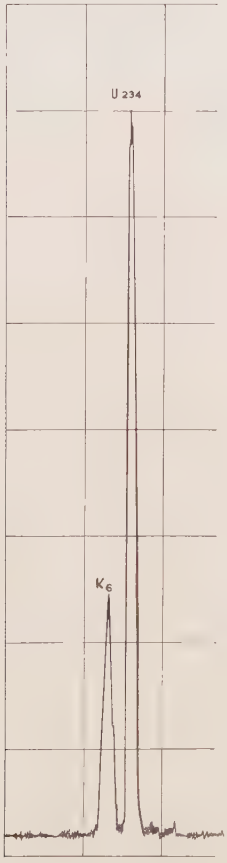

Fig. 9. Spectrum showin gresolutions of U^{234} and U^{236} from K_6 background.

closing down the detector slit to $\approx 0.001''$ the resolution increased to over 3000 but with an approximately tenfold decrease in beam height. Fig. 9 shows a spectrum taken at normal resolution. The K_6 peak is clearly resolved from the U^{234} peaks.

10. Later Improvements

When an Allen type electron multiplier is used to detect ion currents the following difficulties are always encountered. The gain of the device falls with time and can reach a level at which ion counting is very difficult. Nonlinearity arising from the curvature of the first dynode and the surface condition results in distortion of the top of a beam. Ion counting efficiency is rarely much more than 50% and falls as the multiplier ages. This can result in mass discrimination effects.

A new type of ion detector, the scintillation detector[9]), has been developed in this laboratory and one of these has been fitted to the two stage mass spectrometer.

Fig. 10 shows its construction. Ions entering the detector are accelerated to an electrode at the order of 40 kV negative potential and there they release secondary electrons which are accelerated by the same potential to a phosphor, the light signal from which being recorded by a photomultiplier tube. A Faraday bucket is also incorporated which can be used to measure large ion currents. The high voltage electrode is earthed in this case. Metal gaskets are used throughout the detector except that Araldite is used to seal the phosphor to the stainless steel plate.

A new slit system had to be developed since it was necessary to position the slit very close to the point of entrance of the ion beam into the detector. The two plates which make up the slit are mounted on the ends of two large rods. These rods operate with a scissors action to provide opening and closing of the slit. This is actuated externally by a rod mounted on a bellows. This whole system is mounted on a ball race and the angular adjustment of the slit is once again provided by a rod mounted on a bellows which rotates the ball race.

The scintillation detector was found to have the following properties:

1. High counting efficiency. This results from the fact that an ion which strikes the electrode has a high energy, 55 keV, and a low angle of incidence on the electrode, with the result that the secondary electron coefficient is high. Since the number of electrons released is statistical in nature a high coefficient results in a small probability of an ion releasing no electron and remaining undetected.

2. If the device is used to integrate the ion beam current it is found that beams with very flat tops can be obtained. This results in more precise measurement of small ion beams possessing ragged tops due to statistics.

3. Approximately 100 photoelectrons are emitted

from the photomultiplier cathode for every ion entering the detector. This coupled with the gain of 10^6 available from the photomultiplier, enables one to count ions with an amplifier of very low gain, e.g. 10.

single stage machine. These properties, especially the last, make it suitable for cross-section measurements, particularly when the isotope formed by the nuclear reaction is long lived or stable. It is being used at the present for the measurement of neutron

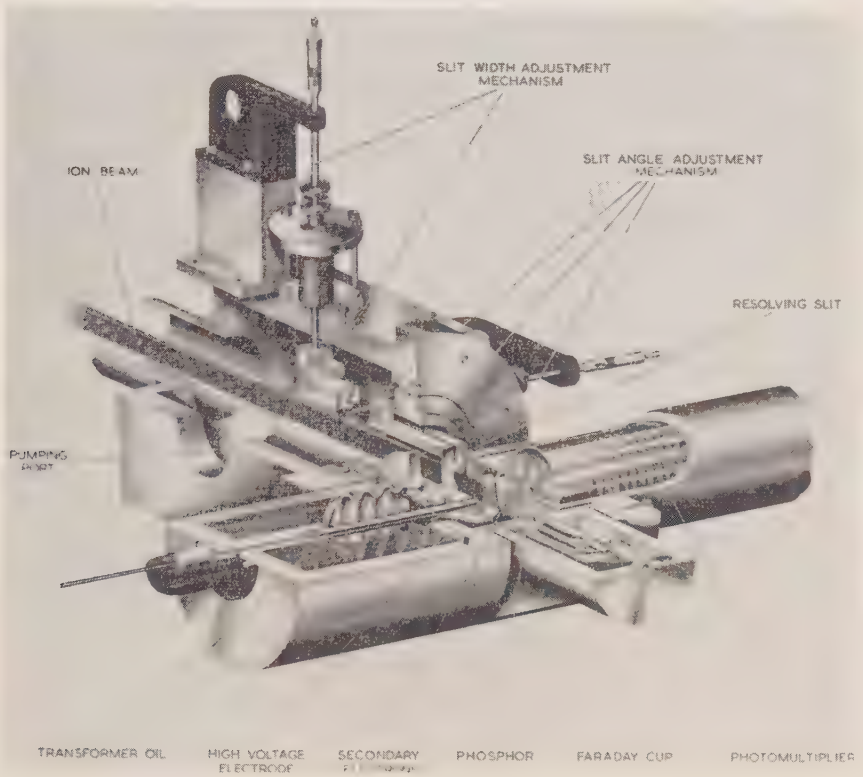

Fig. 10. Diagram of collector slit and scintillation detector assembly.

4. Noise is usually less than 10^{-19} amps.

5. Since the photomultiplier is mounted externally to the vacuum system, it can, in the event of trouble, be replaced in a few minutes.

11. Conclusion

The mass spectrometer described in this paper has been shown to have high sensitivity, low background, good resolution and, in particular, a much enhanced abundance sensitivity compared to a cross-sections of heavy and intermediate weight nuclei. The results of these investigations will be published elsewhere.

Acknowledgements

We are indebted to Dr. S. C. Curran and Dr. F. Morgan for their interest in and encouragement of this work. We also wish to thank the Director of this Establishment for permission to publish this paper.

NUCLEAR INSTRUMENTS AND METHODS 13 (1961) 282–286; NORTH-HOLLAND PUBLISHING CO.

SUR UN CIRCUIT RAPIDE DE MISE EN FORME A SEUIL REGLABLE UTILISANT DES DIODES TUNNEL

S. GORODETZKY, A. MUSER, J. ZEN et R. ARMBRUSTER

Institut de Recherches Nucléaires, Strasbourg

Reçu le 6 juin

A fast pulse shaping circuit with amplitude discriminator using tunnel diodes is described. The threshold is adjustable from 5 mA to 50 mA. The output pulse has a standard amplitude (0.3 V) and length (5 ns). The circuit is intended to be used for fast coincidence technique.

Les circuits de coïncidences à grand pouvoir de résolution en temps et très stables constituent l'élément principal des ensembles électroniques nucléaires. Ces circuits sont des éléments logiques "ET". Il est nécessaire que les impulsions attaquant le circuit "ET", aient une forme standard prédéterminée. Les impulsions d'amplitude variable provenant des détecteurs sont mises en forme à l'aide de circuits électroniques devant satisfaire à deux impératifs: rapidité et stabilité. En particulier, ils doivent être insensibles aux variations de température. Pratiquement on cherche à obtenir une impulsion standard de durée brève de quelques nanosecondes et d'amplitude constante, à partir d'une impulsion d'amplitude et de durée arbitraires dépassant un seuil règlable.

Pour réaliser un tel dispositif, nous avons utilisé un circuit à diode tunnel ou diode Esaki. La figure 1 représente la caractéristique type d'une telle diode. En polarisant celle-ci en un point R sur la partie OP, une impulsion de courant supérieure à la valeur $I_P - I_R$ permet d'obtenir une impulsion de tension d'amplitude $V_F - V_P$. Un seuil règlable peut être obtenu en déplaçant le point de repos. Il est à remarquer que I_P dépend peu de la température, l'effet tunnel étant un phénomène quantitique. La diode Esaki peut fonctionner avec des temps de commutation très rapides de l'ordre de quelques nanosecondes; elle est donc toute indiquée comme générateur d'impulsions brèves.

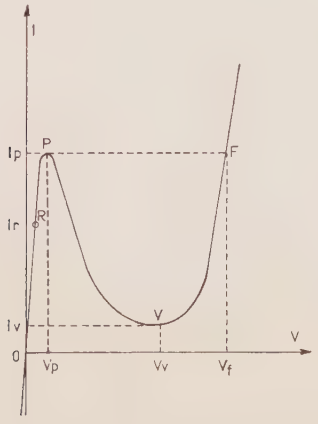

Fig. 1. Caractéristique type d'une diode tunnel.

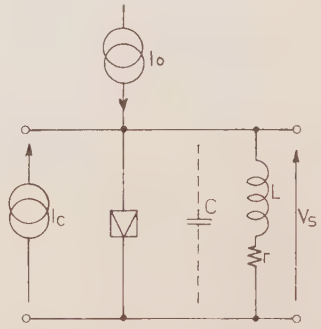

Fig. 2. Circuit multivibrateur.

La figure 2 représente le schéma du circuit multivibrateur que nous avons utilisé, comprenant une diode tunnel 1 N 2941 G.E.

Si l'on polarise la diode tunnel en R, point de repos sur la partie de la caractéristique à résistance négative, on obtient des oscillations entretenues

(fig. 3). Le courant total passant par la diode Esaki et la résistance r est noté I_0. La droite de charge représentant la résistance r passe par I_0. Pour qu'il n'y ait pas de point de fonctionnement stable, if faut que la droite de charge ne coupe la

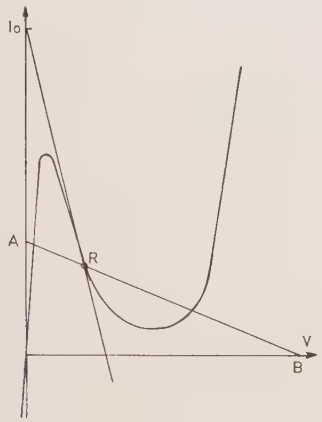

Fig. 3. Mode de fonctionnement en oscillateur.

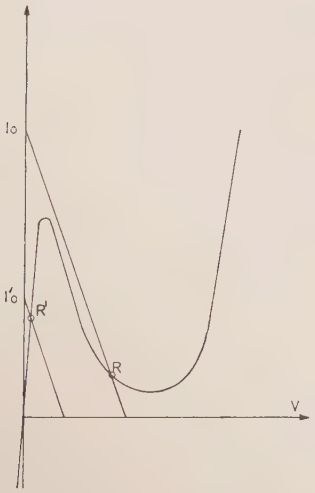

Fig. 4. Mode de fonctionnement en oscillateur déclenché.

caractéristique de la diode qu'en un seul point et ne traverse pas une partie à résistance positive comme c'est le cas pour la droite AB. Par conséquent la résistance r doit être inférieure en valeur absolue à la résistance négative présentée par la diode. Dans ce cas nous sommes en présence d'un oscillateur classique à résistance négative. Les oscillations dépendent de L, r et C, C étant la capacité totale placée en parallèle sur la diode tunnel.

Pour obtenir un régime oscillatoire déclenché, on polarise la diode en R' en diminuant I_0 jusqu'à la valeur I_0'. Le point de repos est ainsi en dessous de V_P (fig. 4). Si nous superposons à la polarisation une impulsion de commande I_c de durée D et d'amplitude $I_0 - I_0'$, nous obtenous les mêmes oscillations que précédemment pendant la durée D de l'impulsion.

Une impulsion unique est déclenchée, si l'impulsion de commande a une durée inférieure à la période de récurrence des oscillations.

La durée d'une telle impulsion peut être déterminée par un circuit de différentiation. Une impulsion unique peut également être obtenue si l'amplitude de l'impulsion de commande est comprise dans certaines limites.

Pour obtenir ces impulsions de commande, nous attaquons le multivibrateur par un trigger fournissant une impulsion de sortie d'amplitude constante.

Le schéma réalisé est constitué d'un quadripole en L comportant dans la branche série une résistance R et dans la branche parallèle la diode tunnel 1 N 2941 (fig. 5). Pour la mise au point du circuit nous avons utilisé un générateur Hewlett-Packard de résistance interne 50 Ohms fournissant des impulsions rectangulaires de 1 μsec de durée et d'amplitude variable. Le signal de sortie est observé à l'aide d'un oscilloscope cathodique Tektronix 585.

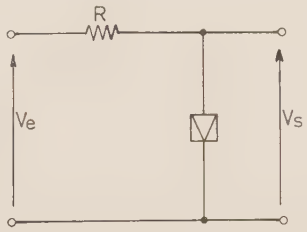

Fig. 5. Circuit du trigger.

La figure 6 indique la façon d'obtenir graphiquement la forme de l'impulsion de sortie à partir de l'impulsion d'entrée pour une résistance R donnée. Les mesures de la fonction de transfert du circuit décrit ci-dessus sont résumées par la figure 7.

On remarque que pour les faibles valeurs de R (0 à 20 Ohms), inférieures à la résistance négative de la diode, on obtient des régimes oscillatoires dépendant des paramètres passifs du circuit. Si R est compris entre 20 Ohms et quelques centaines

d'Ohms, la variation de résistance interne de la diode pertube l'impédance de transfert; une réaction de la tension de sortie sur la tension d'entrée a lieu. A partir de $R = 500$ Ohms, la variation de la résistance interne de la diode est faible par rapport à R et la réaction de la tension de sortie sur la tension d'entrée est négligeable. Pour la diode étudiée, une résistance série $R = 500$ Ohms minimum est donc à utiliser pour obtenir un fonctionnement satisfaisant.

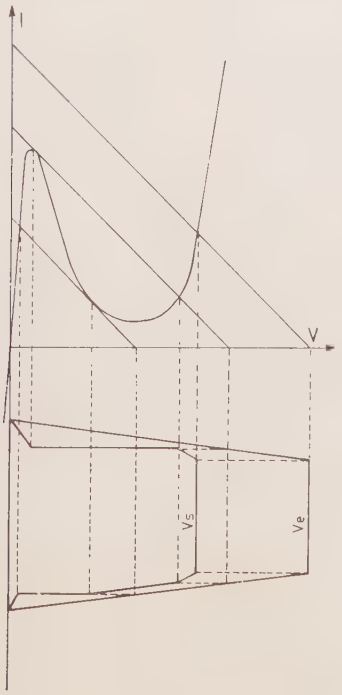

Fig. 6.
Construction graphique de l'impulsion de sortie du trigger.

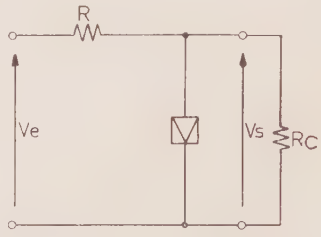

Fig. 8. Circuit du trigger avec charge.

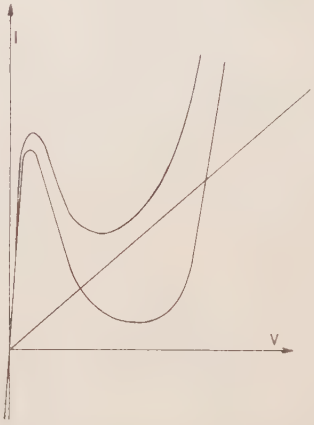

Fig. 9. Caractéristique statique de l'ensemble diode tunnel et résistance de charge.

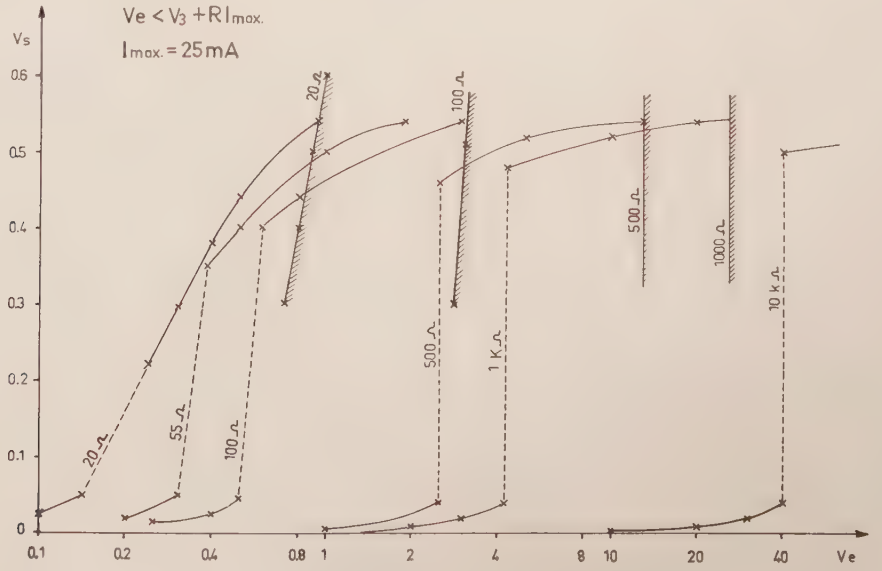

Fig. 7. Fonction de transfert du trigger.

En pratique, le circuit est utilisé avec une résistance de charge R_c localisée à la sortie du quadripole, soit par une résistance parallèle, soit par la résistance d'entrée d'un circuit complexe suivant le schéma de la figure 11. Le seuil est déterminé par la différence des courants $I_P - I_0$. Les capacités C_1 et C_2 de 0.1 μF limitent le courant continu au seul circuit de diode. La résistance de

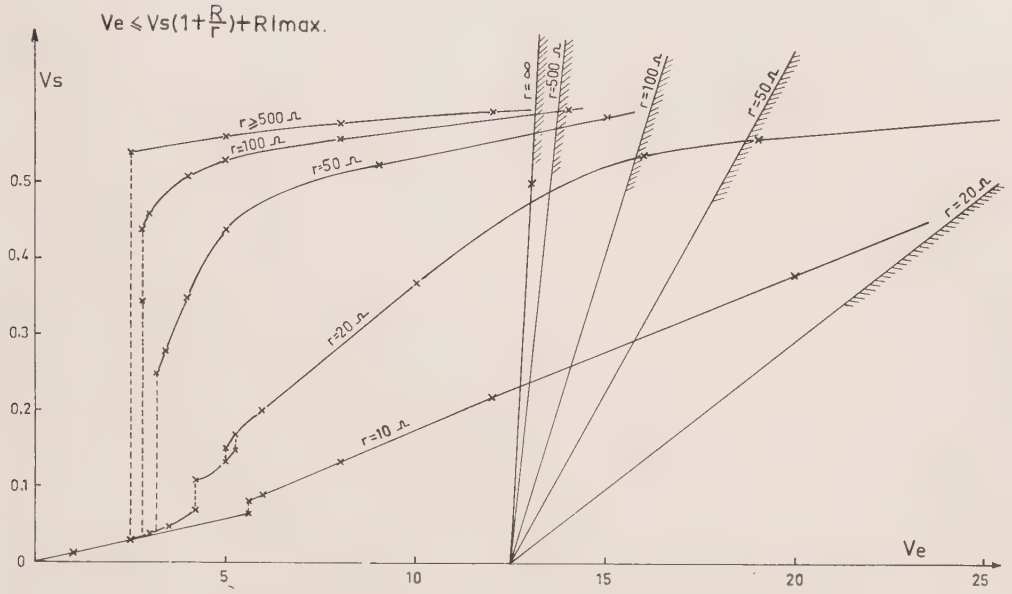

Fig. 10. Fonction de transfert du trigger pour différentes charges.

placé en aval de la diode (figure 8). La figure 9 indique comment cette charge perturbe la caractéristique volt-ampère de la diode tunnel. On remarque que la résistance R_c doit être suffisamment grande pour conserver autant que possible le rapport pic vallée nominal de la diode, La figure 10 résume l'étude de la fonction de transfert du circuit utilisé pour différentes résistances de charge. Un fonctionnement acceptable est obtenu pour une charge de 500 Ohms.

Un seuil variable de discrimination est introduit à l'aide d'une polarisation de courant I_0 de la diode

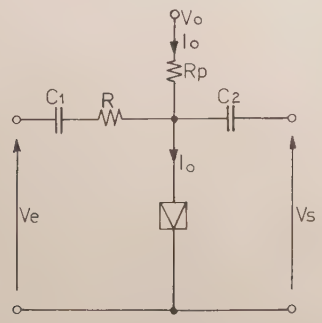

Fig. 11. Circuit du trigger avec polarisation.

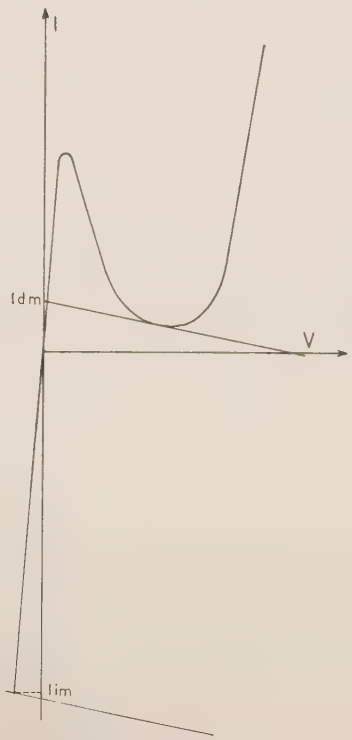

Fig. 12. Limites du courant de polarisation.

polarisation R_P doit être grande devant celle de la diode; elle a été prise égale à 500 Ohms. Le courant de polarisation I_0 est déterminé par l'intersection de la droite de charge avec la caractéristique de la diode. (fig. 12). Il est limité d'une part par le

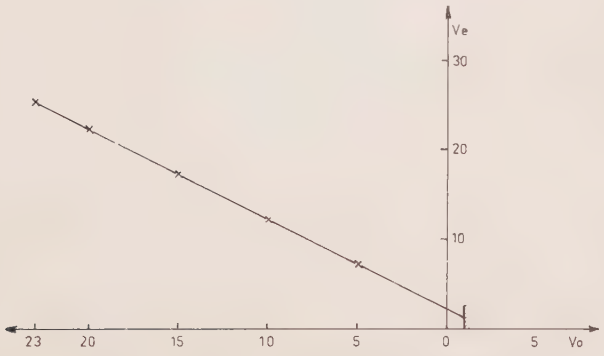

Fig. 13. Seuil de déclenchement du trigger.

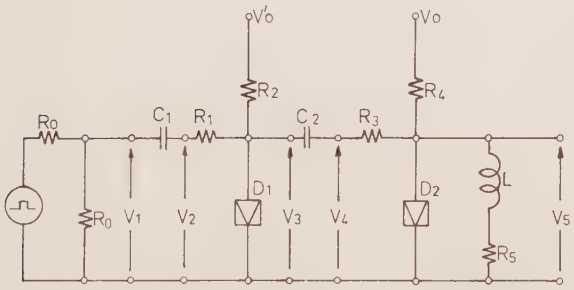

Fig. 14. Schéma d'ensemble.

courant inverse maximum I_{im} traversant la diode, qui est de l'ordre de 50 mA pour la diode 1 N 2941. Si la droite de charge coupe la caractéristique de la diode en un deuxième point stable, l'impulsion d'attaque amène le point de fonctionnement à cette intersection et il n'y a plus de basculement ultérieur possible. Ce phénomène limite d'autre part le courant direct de polarisation. Comme la polarisation en courant direct augmente à peine la plage du seuil, on utilisera donc en général une polarisation négative. La figure 13 indique la tension d'entrée V_e nécessaire au déclenchement de la diode en fonction de la tension de polarisation V_0. La variation $V_e = f(V_0)$ est très linéaire. Le rapport entre le seuil maximum et le seuil minimum est donné par la relation:

$$\frac{I_p + I_{im}}{I_p} = \frac{55}{5} = 11 .$$

La figure 14 montre le schéma d'ensemble du

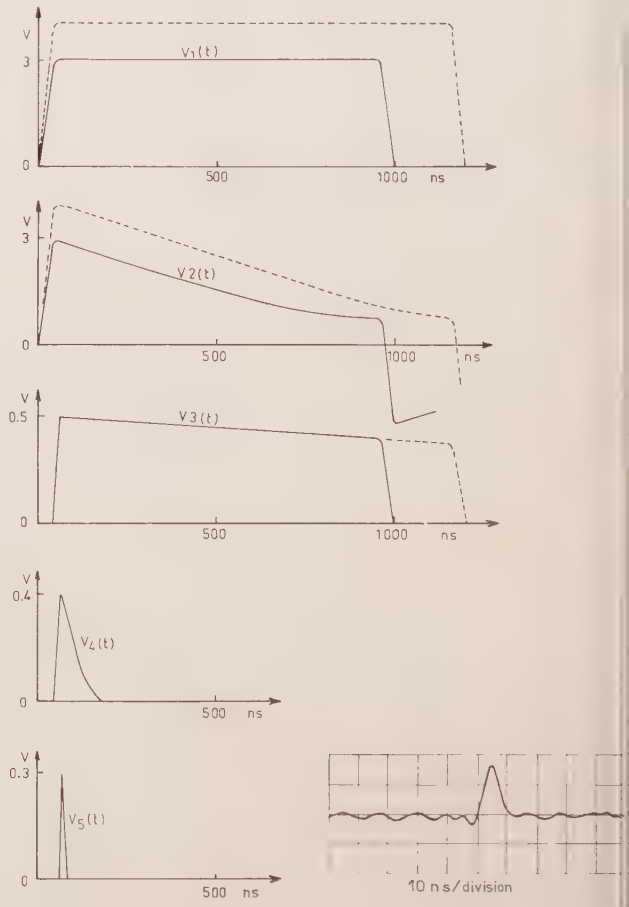

Fig. 15. Forme des signaux du circuit complet.

circuit comprenant le trigger et le multivibrateur monostable. Ce circuit permet d'obtenir une impulsion de sortie de quelques nanosecondes de durée avec une amplitude de 0.3 V, à partir d'une impulsion d'entrée arbitraire (fig. 15).

Le circuit décrit ci-dessus a été utilisé pour attaquer un circuit de coïncidences du type Bell et Petch fonctionnant avec une diode tunnel. Des résultats intéressants ont été obtenus et seront publiées ultérieurement.

Nous remercions Monsieur Lacour du C.E.N. de Grenoble qui a bien voulu mettre à notre disposition des résultats obtenus à l'aide de diodes tunnel.

NUCLEAR INSTRUMENTS AND METHODS 13 (1961) 287–296; NORTH-HOLLAND PUBLISHING CO.

THE NUCLEAR REACTOR AS A HIGH INTENSITY SOURCE FOR DISCRETE GAMMA RAYS UP TO 11 MEV†

L. JARCZYK*, H. KNOEPFEL**, J. LANG, R. MÜLLER and W. WÖLFLI

Laboratorium für Kernphysik, Eidg. Techn. Hochschule, Zürich

Received 14 July 1961

The use of a nuclear reactor as a potential high-intensity source of discrete gamma rays for energies up to 11 MeV is discussed in the light of investigations undertaken. The advantages and disadvantages inherent in such sources are compared with those associated with other gamma sources for this energy region, such as, in particular, proton capture reactions. The following features indicate interesting possibilities in employment of sources: (a) a large variety of discrete gamma rays of various energies exists (there are about 10 lines between 3 and 11 MeV); (b) background is low (for background quanta above 4 MeV, the line to background intensity ratio ranges up to about 10); (c) collimation is good (the beam can be collimated along a 4 m path) and (d) intensity is very high (about a 1000-fold that of (p, γ)-sources in practice). The absolute intensity can with ease be calibrated to within 10%. Experimental details are given, e.g. of collimation, target container and target material, and an arrangement is proposed whereby an appreciable increase of line to background intensity can be attained.

1. Introduction

As has been pointed out earlier[1,2]), a nuclear reactor may present some interesting potentialities as an intense source of discrete gamma rays up to 11 MeV. In this paper we shall summarise findings obtained with the 1 MW swimming-pool type reactor "SAPHIR"[3]) for this application and discuss advantages and disadvantages of such a gamma ray generator compared with other gamma sources in the same energy range.

These gamma rays, produced by neutron capture in different nuclei, are limited to a narrow range from 3 to 11 MeV. In this energy region, however, many physical processes have thresholds or become appreciable, indicating the experimental feasibility of utilising to advantage the high intensity coupled to a correspondingly low background, the choice of the many gamma lines with different energies and the excellent collimation. The energies are generally known with an uncertainty smaller than $\pm$ 8 keV, whereas the intensity can easily be calibrated with an absolute error of less than 10%.

As is obvious from shielding considerations, several metres seperation is required between the reactor core and the experimental assembly. The gamma-generating target can in principle be arranged anywhere in between: we confine the present discussion to the case of targets placed near the reactor core, which appears preferable to the alternative situation wherein the target is arranged in proximity to the experimental set-up[4,5]). The gamma and fast neutron background is appreciably reduced when the collimated gamma beam does not see the reactor core. Accordingly, a beam hole which goes through the reactor core or which is tangential to it is generally required when reactors are to be employed as sources of high-energy gamma rays.

† Work supported by the Schweizerischer Nationalfond zur Förderung der wissenschaftlichen Forschung, Komission für Atomwissenschaft.

* On leave from the Institute of Physics, Jagiellonic University, Krakow.

** Now at the Laboratorio Gas Ionizzati, EURATOM-CNEN, Frascati (Roma).

[1]) H. Knoepfel, P. Scherrer and P. Stoll, Z. Physik 156 (1959) 293.

[2]) L. Jarczyk, H. Knoepfel, J. Lang and W. Wölfli, Bull. Am. Phys. Soc. 4 (1959) 477.

[3]) F. Alder, A. Colomb, W. Hunzinger, T. Hürlimann and H. Winkler, Second Int. Conf. Atomic Energy (United Nations, Geneva, 1958) Vol. 10, Research Reactors, p. 192, "Some operating Experience with the Swiss Pool-Type Reactor SAPHIR.

[4]) V. O. Eriksen and C. P. Zaleski, J. phys. radium 15 (1954) 492.

[5]) R. E. Welsh and D. J. Donhaue, Phys. Rev. 121 (1961) 880.

TABLE 1

Neutron capture gamma ray sources

Element	Target compound	γ-energy (MeV)	γ-flux at 4 m (cm^{-2} sec^{-1})	Intensity Q photons/ 100 capture		$\sigma_a \cdot Q$ (barn)	$\frac{\sigma_a \cdot Q}{\sigma_{sn}}$	$\frac{\sigma_a \cdot Q}{\sigma_{s\gamma}}$	Additional lines MeV (Q)
1	2	3	4	a 5	b	6	7	8	9
Si^{28}	metal	3.54	$3.1 \cdot 10^6$	60	36	$9.6 \cdot 10^{-2}$	$2.1 \cdot 10^{-3}$	$6.9 \cdot 10^{-3}$	7.18(8); 6.40(11)
		4.93	3.9	75	37	12	2.6	8.4	5.11(8); 4.20(10)
Mg^{24}	metal	3.92	1.2	47	30	3.2	0.43	2.7	3.55(8); 3.40(5) 3.29(9)
C^{12}	graphite	4.95	0.2	70	75	0.26	0.07	0.43	
S^{32}	solid(α)	5.43	8.8	60	48	31	7.8	19	4.84(11); 4.38(7)
Y^{89}	powder Y_2O_3	6.07	6.0	45		59	7.4	15	
Ca^{40}	metal	6.42	3.6	40	22	17.5	5.3	8.0	5.89(6); 5.49(4)
Ti^{48}	metal	6.75	43	41	38	238	38	100	6.55(6); 6.41(29)
Be^{9}	metal	6.82	0.8	75	73	0.75	0.17	1.9	
Pb^{207}	metal	7.38	0.7	93	93	15.8	2.3	1.9	
Fe^{56}	metal	7.64	12	29	31	76	19	29	7.28(3)
Al^{27}	metal	7.73	1.6	20	24	4.8	1.1	3.7	
Ni^{58}	metal	9.00	19	26	28	119	15	43	8.53(11); 7.82(6) 7.53(4)
Cr^{54}	metal	9.72	2.8	5	7	15.5	4.6	6.7	8.88(14); 8.50(5)
N^{14}	melamine ($C_3N_6H_6$) powder	10.83	0.6	11	15	0.88	0.36	1.3	

Col. 1. The target nucleus is given, in which the neutron capture is followed by the emission of the gamma ray of Col. 3.
Col. 2. The target contains natural isotope mixture. All compounds are stable below 650° C, except sulphur (119°), lead (327°) and melamine (250°).
Col. 3. The energy of the main gamma line. Other lines of the spectrum are given in Col. 9.
Col. 4. Target weight 500 g. Reactor power 1 MW, corresponding to a neutron flux at the target of $\phi_{th} = 6 \times 10^{12}$ cm^{-2} sec^{-1}. No absorber in the beam path. The target weights of the yttrium and melamine compounds are respectively 630 g and 750 g.
Col. 5. Q is the number of photons per 100 neutron captures in the natural isotope mixture. 5a are the (new) Canadian values as tabulated in ref.[8]) 5b are the Russian values as tabulated in ref.[6]).
Col. 6. σ_a is the radiative absorption cross section for the natural element. For Q the Canadian values of 5a has been taken.
Col. 7. σ_{sn} is the integrated cross section value for neutron scattering in the energy range 0.1 — 1 MeV.
Col. 8. $\sigma_{s\gamma}$ is the cross section for Compton scattering of 1 MeV gamma rays.
Col. 9. The gamma lines are given, which are located around the main line in a range going from an energy 20 % less than listed in col. 3 to any higher value in the spectrum. Only the gamma rays having at least 10 % of the intensity of the main line are considered.

2. Energy and Intensity of the Gamma Rays

The neutron capture gamma rays, which are of interest for this application, are listed in table 1. The decisive factors governing their choice are: a strong gamma line at the upper energy limit of the spectra, separated by an energy interval of at least 0.5–1 MeV from any lower line and the absence of any particular requirements or restrictions upon the target material. Although obviously no strictly monoenergetic spectra can be produced, lower-energy rays if located sufficiently far from the main line may be prevented from interfering by experimental discrimination or because the threshold of the process to be studied sets in at a higher energy. The same can be said of the background, which generally starts to be of some importance

below 2.5 MeV. If the rest of the gamma spectrum and the gamma and fast neutron background does not represent a major difficulty for the experiment, then a rather large choice of different "monochromatic" gamma rays can be considered. A qualitative and schematic description of some of the experiment and gamma source represents a rather large but unavoidable intensity loss in consequence of reactor shielding. On the other hand, this can be turned to advantage in permitting a high degree of collimation of the gamma beam. The figures tabulated in column 4 of table 1 are given only as

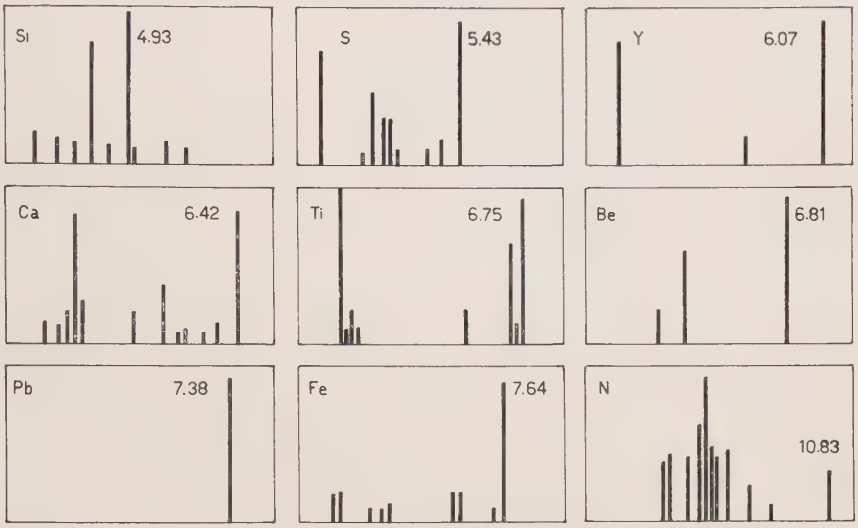

Fig. 1. Bar graphs of some typical neutron capture gamma spectra. The energy scale is linear and defined by the value in MeV attributed to the most important line. The relative intensities of the different lines are proportional to their heights (the thickness of the bars is arbitrary and has no meaning). Only the gamma rays having at least 10% of the intensity of the main line and an energy larger than 0.6 MeV are considered. For the absolute intensities and other details cf. table 1.

spectra is supplied by fig. 1. More exact information of the principal neutron capture gamma spectra is available from the literature[6,7,8]).

Also given in table 1 is the absolute flux of the corresponding gamma rays, measured in quanta per cm^2 per sec at a distance of 4 m from the target. The thermal neutron flux upon the target is 6×10^{12} $cm^{-2}\,sec^{-1}$, corresponding to a reactor power of 1 MW. The distance of several metres between representative examples. The intensity will be decreased by introducing neutron or gamma filters, or by reducing the reactor power. The intensity

Table 2

Intensity comparison between different gamma ray sources

Reaction and target	Energy (MeV)	Gamma flux ($cm^{-2}\,sec^{-1}$)
Reactor: $\phi = 6 \times 10^{12}$ $cm^{-2}\,sec^{-1}$		
500 g		4 m from target
$Tl^{48}(n,\gamma)$	6.75	4×10^7
$Pb^{207}(n,\gamma)$	7.38	7×10^5
Accelerator: 1 *mA proton current*		
thick target		0.3 m from target
$F^{19}(p,\alpha\gamma)$	6.1	1×10^5
$Li^7(p,\gamma)$	17.6	1×10^4
Betatron		
energy limit	$E = 10$	0.5 m from target
31 MeV	$\Delta E = 0.1$	1×10^6

[6]) L. V. Groshev *et al.*, *Atlas of Gamma Ray Spectra from Radioactive Capture of Thermal Neutrons* (Pergamon Press, London, 1959).

[7]) G. A. Bartholomew and L. A. Higgs, *Compilation of Thermal Neutron Capture Gamma Rays*, Atomic Energy of Canada Ltd., Rep. 669 (1958).

[8]) E. Troubetzkoy and H. Goldstein, *A compilation of Information on Gamma-Ray Spectra Resulting from Thermal-Neutron Capture*. ORNL-2904, 1961.

[9]) C. Y. Chao, A. V. Tollestrup, W. A. Fowler and C. C. Lauritsen, Phys. Rev. **79** (1950) 108.

[10]) C. P. Swann and F. R. Metzger, Phys. Rev. **108** (1957) 982.

[11]) K. Reibel and A. K. Mann, Phys. Rev. **118** (1960) 701.

TABLE 3

Proton capture gamma ray sources

Reaction	Target	Proton energy (MeV)	Gamma energy (MeV)	Rel. yield (%)	Abs. yield γ per proton	References
$F^{19}(p,\alpha\gamma)$ *	CaF_2 (thick)	0.340	6.14 6.92 + 7.12	100 4	0.17×10^{-7}	[9]
	(thick)	0.875	6.14 6.92 7.12	100 37 17	3.7×10^{-7}	[9]
	(thick)	1.38	6.14 6.92 7.12	100 9 6	8.2×10^{-7}	[9]
	(thin: 1 mg/cm²)	2.05	6.14 6.92 7.12	13 25 100	80×10^{-7}	[10], [11]
	1 mg/cm²	2.40	6.14 6.92 7.12	31 100 25	80×10^{-7}	[10], [11]
$B^{11}(p,\gamma)$	metal (thick)	1.39	12.2 16.7	100 75	0.05×10^{-7}	[9]
$Li^7(p,\gamma)$	metal (thick)	0.441	14.8 17.6	50 100	0.26×10^{-7}	[9]
$T(p,\gamma)$	deposited (thick)	0.100	20.4		2.6×10^{-10}	[9]

* The 6.92 and 7.12 MeV gamma ray are known to have a Doppler broadening of about 130 keV from the recoil imparted to the nucleus by the preceding α-emission (cf. ref. [9]) and [10]).

may also be increased, by an order of magnitude or two, if a high- flux reactor is available, but heating of the target material and other technical difficulties then have to be taken into consideration.

A comparison with other gamma sources in the same energy range is made in table 2, which reveals some interesting details. In table 3, data of the proton capture reactions, considered for the gamma source application and collected from different references, are compiled in some detail to allow better comparison. On considering the proton capture gamma ray (table 3), in particular that from the widely- used reactions $F^{19}(p,\alpha\gamma)O^{16}$ and $Li^7(p,\gamma)Be^8$, one sees that the resultant gamma fluxes are lower than those for the reactor gammas, even at a distance of 0.3 m from the source and with a proton beam current of 1 mA at 875 kV on the target. Furthermore, both the collimation and the constancy of the intensity of the gamma beam are poorer than in the reactor case. In addition, it can be seen that neither the choice of gamma lines nor the composition of the spectra are better for the proton capture gamma rays. The fluorine target, for instance, produces three gamma lines at 6.14, 6.92 and 7.12 MeV, their relative intensities depending on the proton energy.

In table 2 a comparison is also made with a betatron spectrum. For the purpose of such a comparison the mean intrinsity per 100 keV interval at 10 MeV gamma energy and at a distance of 0.5 m from the target for a betatron operated at 32 MeV is given[12]). Apart from the intensity, the difficulties of evaluating the energy dependance for

[12]) F. Tanner, ETH, Zürich, private communication.

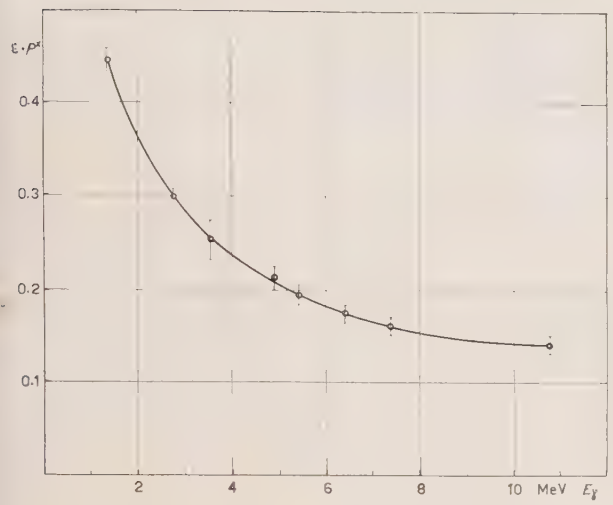

Fig. 2. The absolute photopeak efficiency for a 5″ × 4″ (diameter × height) NaI (Tl) crystal exposed axially to a narrow gamma beam, as determined experimentally (from ref.[13]). The gamma rays of the following elements have been used: Na (activity) Si, S, Ca, Pb, N.

This allows the intensity of the gamma beam to be easily determed with a NaI (Tl) scintillator to within 5 to 10% of its absolute value. In fig. 2 for instance the measured absolute photopeak efficiency of a 5″ × 4″ NaI(Tl) crystal exposed axially to a narrow gamma beam is given for energies from 1 to 11 MeV. The efficiency is given, as usual, by the ratio between the integrated counts over the photopeak—approximated by a Gaussian curve—and the actual number of photons in the same time interval).

3. The Targets

The compounds used for the targets are listed in table 1, column 2. They are of usual chemical purity, except in the case of beryllium and graphite, which are of reactor purity. If possible, substances in the solid phase are chosen (e.g. aluminium, beryllium, graphite, lead, etc.); the rod or disk is

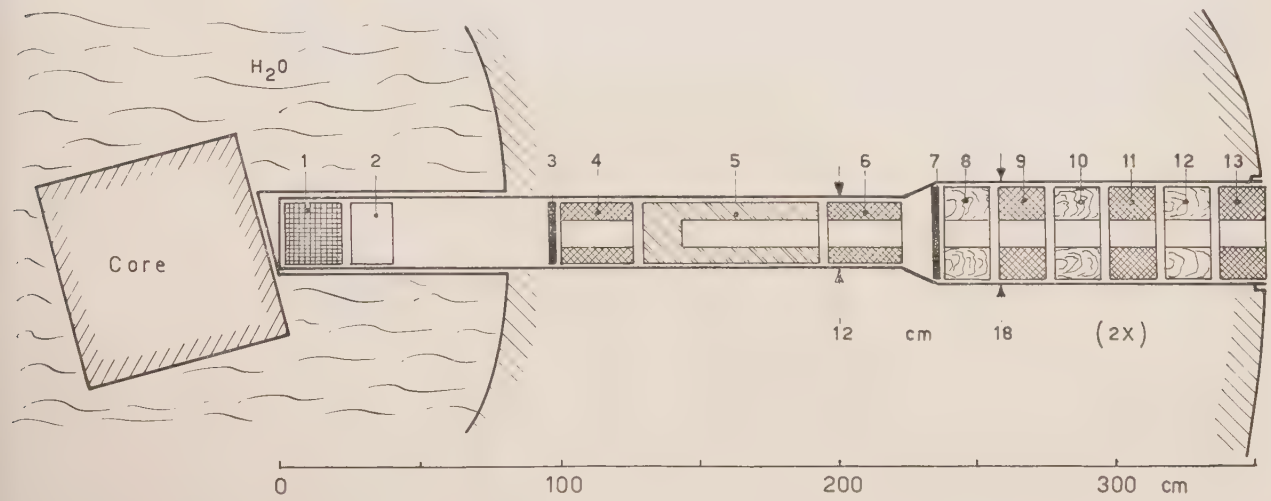

Fig. 3. A collimation assembly set in the radial beam hole. The diameters are scaled with a factor of 2 as compared to the length for better reproduction. The labels have the following meaning: (1) bismuth; (2) target; (3), (7) boron-plastic sheet; (4), (6), (9), (11), (13) lead; (5) boron loaded paraffin; (8), (10), (12) wood.

an experiment performed with a bremsstrahlung spectrum are well known and need not to be described here.

As an application of these neutron capture gamma rays, an experimental calibration of the photopeak efficiency of different scintillators has been undertaken and will be published separately[13]).

[13]) L. Jarczyk, H. Knoepfel, R. Müller and W. Wölfli (to be published).

then centered in the channel by graphite rings and in principle does not require any container.

For the construction of the target containers to be used for granular substance (e.g. silicon, titanium) various points have to be borne in mind. Generally through the collimation one sees only an axial zone of the beam hole, so that the walls (made of aluminium) are prevented from radiating into the collimated beam. If the mean free absorbtion

path of the neutrons in a target is of the order of the inner tube diameter and if high intensity is desired, then only this central zone is to be filled with material. In this case the container is also seen by which is mainly due to the absorption of the reactor gamma rays. In our case the beam hole consists of two concentric aluminium tubs separated by an air gap of 0.3 cm and, therefore, the cooling is in-

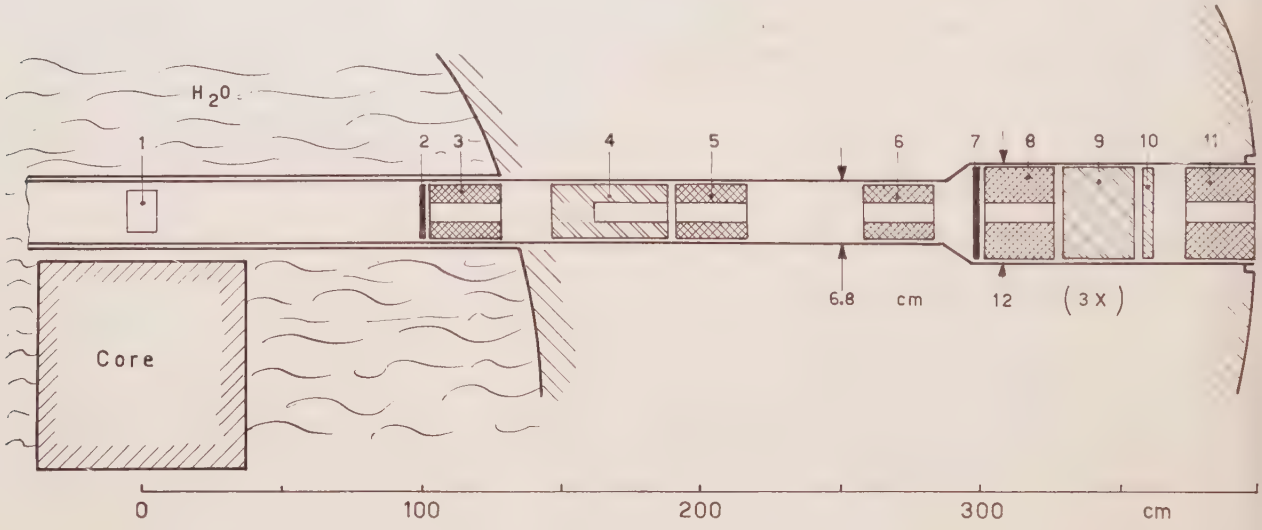

Fig. 4. A collimation assembly set in the tangential beam hole. The diameters are scaled with a factor of 3 as compared to the length for better reproduction. The labels have the following meaning: (1) target; (2), (7) boron-plastic sheet; (3) lead with inner bismuth liner; (4), (9) boron loaded paraffin; (5), (6), (8), (11) lead; (10) iron.

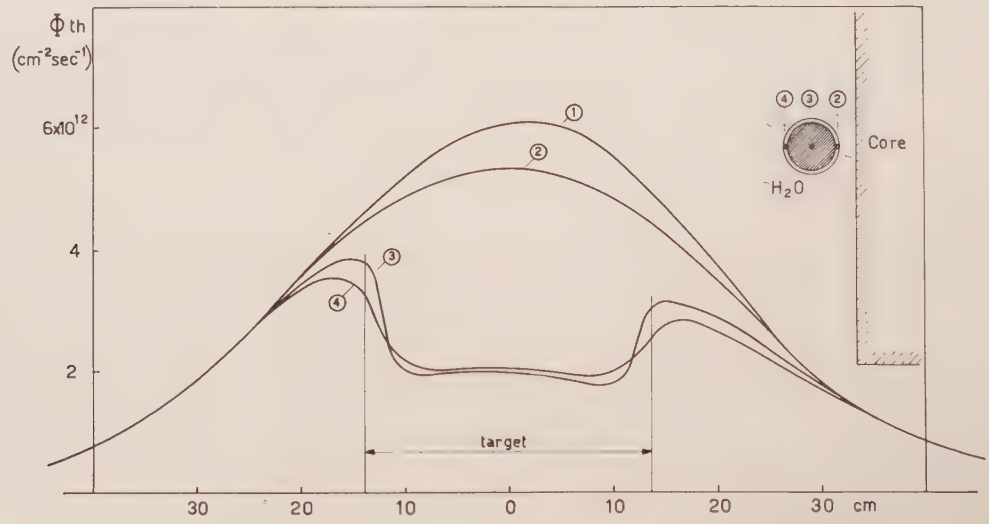

Fig. 5. Thermal neutron flux distribution in the tangential beam hole (cf. fig. 4) with and without target, measured by activation of a copper strip. Target: titanium metal, granular, 6.3 cm diameter and 27 cm length. Curve 1: without target. 2: outside the target and in front of the reactor core. 3: on the axis and inside the target. 4: outside the target and opposite to the core. The insert in the upper right corner of this figure shows the positions of the strip, in relation to the target and the reactor core. For the neutron flux distribution in the radial beam hole see ref.[14]).

the experiment and its contribution to the gamma background has to be considered. Another point to keep in mind is the heat generation in the target sufficient. For instance a lead cylinder, 50 mm diameter and 20 mm thick, placed in the beam hole near the core (*cf.* fig. 4), without any special

cooling, tends to a steady final temperature of 200°C at 1 MW reactor power.

The neutron absorption due to the target introduces a disturbance of the natural neutron flux distribution, which, in some cases, has to be considered in the prediction of the gamma output of the targets. In the case of a large neutron absorber, the flux distribution behaves as shown in fig. 5. However this represents an extreme case, since a large (6 cm diameter) titanium target has been used. The only elements in table 1 having a mean free path for neutron absorption smaller than 20 cm are: Ti (3.1 cm), Fe (4.7 cm), Ni (2.2 cm), Cr (4.2 cm) and N (19 cm). Only for these targets need the above disturbance be considered.

4. The Neutron and Gamma Background

The background problem in connection with such an application of the nuclear reactor is generally considered too pessimistically. It turns out, in fact, that with a careful design of the arrangement, the signal to background ratio is given at least as well, if not even better than with (p, γ)-reactions. (Indicative gamma spectra including background as obtained with a proton accelerator can be seen for instance in ref.[15]).)

The thermal neutrons can easily be absorbed in boron-plastic or boron-paraffin sheets. The epithermal and fast neutrons can partially be scattered out of the beam with paraffin or graphite plugs. The former material has also some advantages in filtering out the gamma background below 2 MeV. With 35 cm of paraffin and 3 cm of iron in the beam path the fast neutron flux is 600 neutrons $cm^{-2}\,sec^{-1}$, when measured with a long counter. This value has been measured at full reactor power (1 MW) in the collimated beam outside the beam hole and for a titanium target. The paraffin and iron scatterers also absorbs 83% of the 6.5 MeV gamma rays and 99.5% of the 1 MeV gamma background. The resulting ratio between the background neutrons and the 6.7 MeV quanta of titanium is 10^{-4} n/γ. This value can be roughly related to other elements, if one considers the ratio of the neutron absorption cross section (reduced to the main line) to the scattering cross section for 0.1–1 MeV neutrons as given in column 7 of table 1.

There are two main contributions to the gamma background. The first is due to the target substance itself and consists of the rest of the prompt gamma spectrum, the radioactivity of the residual nucleus and the gamma rays from other nuclei in the compound. No further improvement can be effected once the right choice of the target has been made.

The second group is due to the reactor gamma-rays scattered by the target into the collimated beam and contains two different components. One is given by the activity of the core (and, therefore, depends on the "history" of the reactor) and the other by the prompt gamma rays of fission and neutron capture in the nuclear fuel, in the supporting structure of the core, in the liner of the beam hole and in the surrounding water moderator.

It is possible to reduce the gamma background of the second group. One can, for instance, improve the neutron to gamma ratio at the target by introducing some gamma absorber between reactor core and target, as discussed further below, or effect an improvement in the intensity ratio of the high- energy gamma ray under consideration and the low-energy background by incorporating suitable absorbers in the collimation assembly. For the latter purpose, apart from the already discussed paraffin absorber, iron and possibly bismuth absorbers can be introduced into the beam, as shown in fig. 4. The arrangements are governed by the experimental requirements and the degree to which the intensity of the main line may permissibly be reduced. For instance the spectrum of fig. 6, curve 2. has been obtained in the tangential beam hole with the following absorbers in the beam (from target to scintillator); 0.5 cm boron-plastic sheet, 10 cm paraffin, 0.5 cm boron-plastic sheet, 25 cm paraffin, 0.5 cm boron-plastic sheet, 3 cm iron. The ratio between the neutron absorption cross section (reduced for the main line) to the gamma scattering cross section for 1 MeV quanta in the target compound given in column 8 of table 1 allows us to find a rough relation between the example of fig. 6 and other elements.

[14]) H. Knoepfel, Ch. Menoud and P. Stoll, Helv. Phys. Acta **31** (1958) 330.

[15]) J. Kockum and N. Starfelt, Nucl. Instr. **4** (1959) 171.

[16]) J. H. Hubbel, Rev. Sci. Instr. **29** (1958) 65.

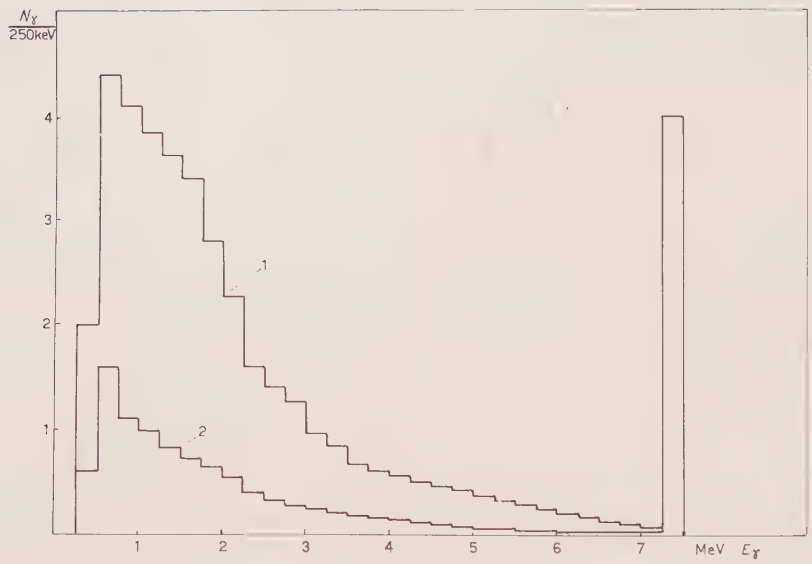

Fig. 6. The absolute spectrum of a lead target including background as determined experimentally at the radial (1) and tangential (2) beam hole (cf. figs. 3 and 4). The lead line has been normalised in both cases, but the actual intensity in the radial case for the same reactor power is 5 times less. Curve 1: 20 cm bismuth absorber before the target and 5 cm paraffin scatterer in the beam. Curve 2: 35 cm paraffin scatterer and 3 cm iron absorber in the beam. The reduction from the measured scintillation spectrum to the absolute curve shown, has been obtained by a computation method described in ref.[16])

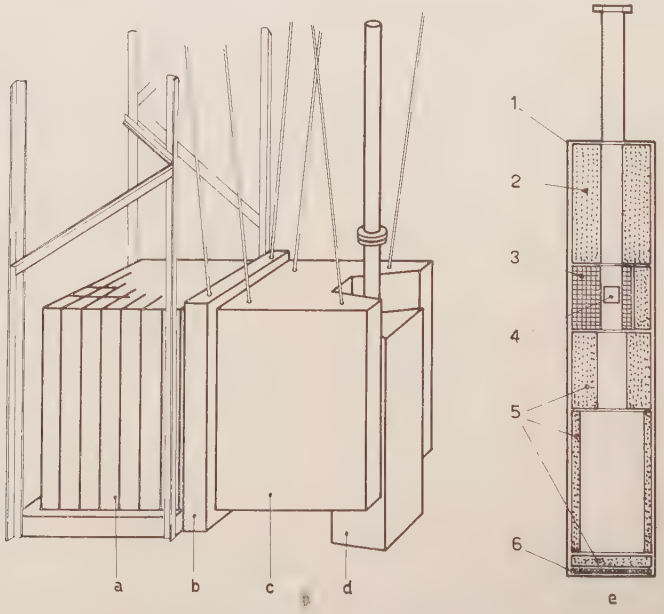

Fig. 7. General view of a special beam hole, designed to improve appreciably the gamma line to backgroung ratio. a: reactor core. b: lead absorber. c: graphite column. d: target chamber and collimation tube. e: cross-section through the target chamber with (1) aluminium casing, (2) and (5) graphite, (3) bismuth, (4) target, (6) boron-plastic sheet.

If it is possible to increase the mean angle between core target and experiment (as for instance in fig. 7) a further reduction of the background is obtained, because of an energy decrease of the Compton scattered quanta, which can then more easily be absorbed in iron or bismuth.

5. The Collimation and the General Assembly

The choice of a definite arrangement depends mainly on the reactor facilities available, on the intensity and background requirements, as also on the degree of collimation and the diameter of the gamma beam.

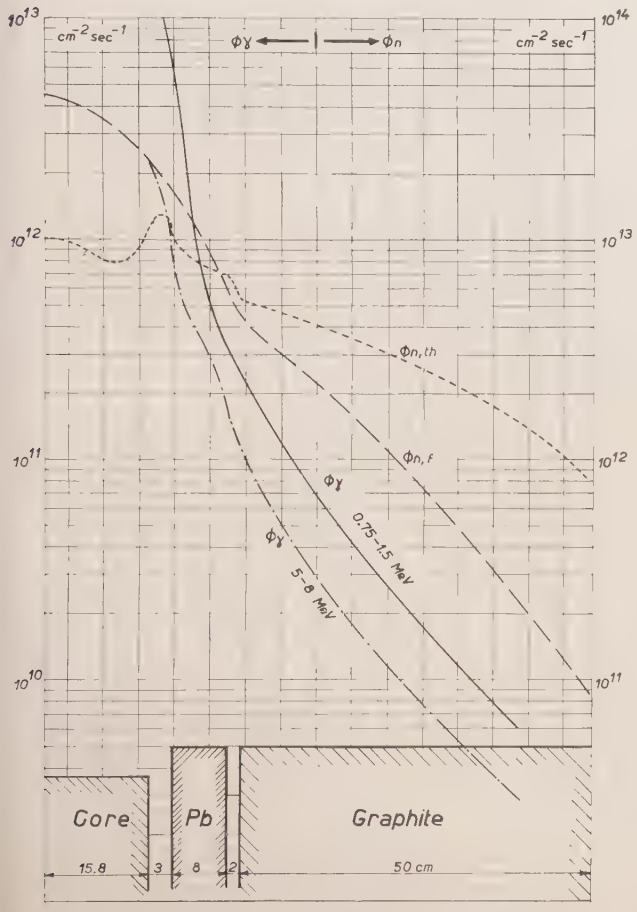

Fig. 8. Flux distribution on the axis of the column of Fig. 7 for thermal neutrons $\phi_{n,th}$, fast neutrons $\phi_{n,f}$, and gamma rays in the two energy ranges of 0.75–1.5 MeV and 5–8 MeV as calculated in ref.[17]). In computing the gamma flux, not only was the degradation of the core gammas[18]) taken into consideration, but also gamma flux ensuring from neutron capture in all elements surrounding the target (in particular, in the lead absorber).

A beam hole of a type which prevents the collimated gamma beam from seeing the reactor core is in nearly all cases a necessary facility. This can be seen from fig. 6, where a comparison is made between the measured lead spectrum in the tangential and radial beam hole of SAPHIR (*cf.* figs. 3 and 4). In the former case 1 a 20 cm thick bismuth absorber is placed between the reactor and the target to reduce the gamma background. But even with this improvement the signal to background ratio is better in the tangential beam hole by a factor of 5.

The measured neutron flux in the tangential beam hole is shown in fig. 5, curve 1. The neutron flux and hence the gamma flux are not perfectly constant in time, even if the reactor power is, and therefore a monitor (for neutrons or gamma rays) is necessary in some cases. This is due to the fact that the control rods of the reactor change in position during a reactor run to keep the power output constant and this causes a modification of the neutron flux distribution in and around the core. After a 10 hour run the neutron flux in the target may be shifted by an amount of up to 15% of its initial value.

For many applications the tangential beam hole with the target placed directly at the reactor core will be sufficient. One collimation set is given in fig. 4.

In some special cases a better line to background ratio is needed. To meet this requirement an additional (vertical) beam hole has been built to keep the reactor gamma background as low as possible. Such a device will be efficient when the inherent target background (due to the rest of the gamma spectrum and the gamma activity) is low, as for instance for beryllium, carbon and lead targets. This facility is shown in fig. 7. Part of the core gamma rays are absorbed in a lead sheet, whereas the thermal neutron flux is sustained by a graphite column. The geometry of the arrangement is such as to reduce the small angle Compton scattering, shifting the still remaining background to lower energy. The target chamber and the collimation channel can be lifted independently from the lead sheet and the graphite column, which are suspended form a bridge near the reactor.

The thermal and fast neutron flux distribution in the lead sheet and graphite column and also the gamma background have been calculated[17]) and the result plotted in fig. 8. One sees that the thermal flux is reduced at the end of the graphite column by a factor of 10, whereas the thermal to fast neutron ratio is increased from 1 to 6.5. The mean reduction of the gamma fluxes is about 10^4, nearly independent for the five different energy intervals between 0 and 8 MeV considered. If one notes the further reduction due to the bismuth absorber shown in fig. 7 and, on the other hand, also some additional gamma rays from neutron capture in the walls of the chamber and in the water, one can say that the total reduction of the gamma background is about 1000. Compared with the arrangement of fig. 4, this facility may, therefore, appreciably improve the signal to background ratio.

[17]) P. Schmid, Eidg. Institut für Reaktorforschung, Würenlingen. Internal Report ST-SR (1960) 17.

[18]) H. Goldstein, *"The Attenuation of Gamma Rays and Neutrons in Reactor Shields", Washington 1957 (US Government Printing Office).*

Acknowledgements

The authors wish to thank Prof. P. Scherrer and Prof. P. Marmier for their interest in the work, as well as to the members of the "SAPHIR" Reactor staff for their helpful cooperation, particularly to Dr. P. Schmid for the calculations plotted in fig. 8. They are also indebted to Dr. E. Sheldon for revising the English translation.

NUCLEAR INSTRUMENTS AND METHODS 13 (1961) 297–304; NORTH-HOLLAND PUBLISHING CO.

BERECHNUNG DER POLSCHUHOBERFLÄCHEN EINES MAGNETISCHEN TEILCHENSPEKTROMETERS

H. U. GERSCH

Zentralinstitut für Kernphysik, Rossendorf b. Dresden, Bereich Reaktortechnik und Neutronenphysik

Eingegangen am 10. Juni 1961

For a high resolving flat spectrometer with 190 degree focusing the surfaces of the pole pieces have been calculated using conformal mapping. The perturbation of the magnetic field near the edges has been taken into account. The influence of the exciting coil and hysteresis effects are also discussed. A general method is developed to calculate the correction to be applied to the pole pieces, if the field produced by them deviates slightly from the prescribed field.

1. Einleitung

Hochauflösende Spektrometertypen verdanken ihre Fokussierungseigenschaften inhomogenen Magnetfeldern, deren Genauigkeit über die Güte der Geräte entscheidet. Eine Erzeugung der Magnetfelder mit Luftspulen kommt dabei in den seltensten Fällen infrage. Das Magnetfeld zwischen den Polschuhen eines Eisenmagneten hängt jedoch von der Form der Polschuhflächen ab. Randeffekte, die Nähe von Erregerwicklungen und Hysteresiseigenschaften beeinflussen seinen Verlauf, so daß es in vielen Fällen nicht im ganzen Raum zwischen den Polschuhen verwertbar ist, da es höchstzulässige Abweichungen vom theoretisch geforderten Feldverlauf überschreitet†.

Oft werden aber gerade Aufwand und Größe eines Gerätes davon abhängen, inwieweit es gelingt den ungenutzten Raum zwischen den Polschuhen zu reduzieren.

Im allgemeinen wird man versuchen, die oben genannten störenden Effekte, besonders den Randabfall, durch geeignete Wahl der Polschuhoberflächen zu berücksichtigen. In anderen Fällen wird zur Vermeidung der Randeffekte die Konstruktion des Spektrometers geeignet gewählt, indem Joch und Erregerspulen außerhalb des Feldraumes angeordnet werden[1,2]).

Von Wild und Huber[3]) werden die Randeffekte mit gutem Erfolg durch Leitbleche beseitigt, die durch Zwischenspulen auf den erforderlichen magnetischen Potentialen liegen.

Bei der Entwicklung von Spektrometermagneten spielten bisher Modellversuche und auch Vorversuche im elektrolytischen Trog eine wichtige Rolle. In einigen Fällen wurden auch die Polschuhoberflächen unter Vernachlässigung aller störenden Einflüsse berechnet und nachträglich empirische Korrekturen angebracht.

Dabei wurde die Realisierung des geforderten Feldverlaufes durch sukzessive Näherungen der Polschuhform durchgeführt, die nach jedem Schritt eine Messung des Feldverlaufes und eine weitere Bearbeitung der Polschuhoberflache nach Erfahrungswerten nötig machte[4,5]).

Eine sorgfältige Berechnung müßte die Zahl der Näherungsschritte jedoch wesentlich vermindern können, wenn nicht eine Nachbearbeitung der Polschuhe vollständig überflüssig machen. Dabei wird man im allgemeinen zwei Probleme zu lössen haben, die Realisierung des geforderten magnetischen Feldverlaufes und die Korrektur der störenden Effekte.

Wichtig ist dabei die Forderung, daß die Korrekturen additiv auf die jeweils erhaltene Oberfläche aufgebracht werden können.

† Wir wollen von den Fällen absehen, in denen gerade Randeffekte zur Doppelfokussierung benutzt werden, also erwünscht sind, wie z.B. im Prismenspektrometer.

[1]) E. Arbman und N. Svartholm, Ark. Fysik **10** (1956) 1.
[2]) M. Sakai und H. Ikegami, J. Phys. Soc. Japan **13** (1958) 1076.
[3]) H. Wild und O. Huber, Helv. phys. Acta **30** (1957) 3.
[4]) A. V. Solotavin, Izv. A. N. SSSR Ser. Fis. **18** (1954) 127.
[5]) N. Svartholm und K. Siegbahn, Ark. Mat. Astr. Fys. A **33** (1946) 1.

Als Beispiel und zur Erläuterung der Methode sollen die Polschuhoberflächen eines Flächenspektrometers mit 190°-Fokussierung berechnet werden, deren Feld im ausgenutzen Bereich weniger als 0.1% vom Sollwert abweicht†. Der ausgenutzte

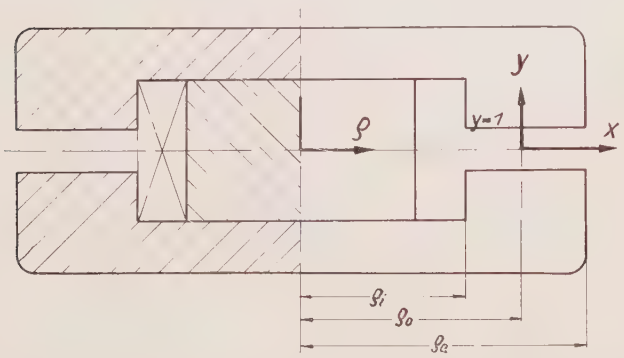

Abb. 1. Querschnitt durch den Doppelpilzmagneten mit einem Sollkreisradius von 15.5 cm. Die Koordinaten sind so normiert, daß der Polschuhabstand gleich 2 wird.
$\varrho_0 = 10 \qquad \varrho_i = 7.4 \qquad \varrho_a = 12.9$

Bereich soll dabei fast den gesamten Raum zwischen den Polschuhen des in Abb. 1 gezeigten Doppelpilzmagneten einnehmen.††

Im allgemeinen wird das für die Fokussierung hoher Ordnung geforderte Magnetfeld in der Mittelebene zwischen den Polschuhen rotationssymmetrisch vorgegeben. Im Prinzip gibt es für die Wahl der Feldverteilung noch andere Möglichkeiten, z.B. für eine exakte 180°-Fokussierung einen einseitig abfallenden Feldverlauf[7,8]). Ein rotationssymmetrisches Feld hat jedoch neben den Vorteilen für die Berechnung der Bahngleichungen und Abbildungseigenschaften im Spektrometer konstruktive Vorteile, die in der Verwendung eines Zentraljoches und der einfachen Bearbeitung auf einer Drehbank liegen.

Da das Feld zwischen den Polschuhen wirbelfrei ist, existiert ein skalares Potential. Will man das Problem der Polschuhform rechnerisch lösen, muß man die Polschuhoberflächen als Äquipotentialflächen des Magnetfeldes betrachten. Dies ist unter der Voraussetzung der Verwendung von ideal weichem Eisen zulässig†††.

Stoker *et al.*[10]) geben für einen Spezialfall Lösungen der Laplaceschen Differentialgleichung in Form einer Reihenentwicklung nach dem Abstand von der Rotationsachse an. Diese Methode setzt jedoch voraus, daß der Feldverlauf in der Rotationsachse keine Singularitäten aufweist. In unserem Problem würde sie nur auf eine Näherung führen, die umso besser ist, je größer das Verhältnis des Achsenabstandes zum Polschuhabstand ist.

Bei großen Werten dieses Verhältnisses ist jedoch eine Lösung der Laplaceschen Differentialgleichung in der Ebene ebenso zulässig. Den Lösungsweg liefert dann die Funktionentheorie. Das hat neben einem vereinfachten Rechnungsgang den Vorteil, daß sich Korrekturen für den Feldabfall in der Nähe der Polschuhränder angeben lassen. Die Einflüsse durch die so vernachlässigte Rundung der Polschuhe in der 3. Dimension lassen sich zusätzlich durch eine Störungsrechnung berücksichtigen.

Lee-Whiting[6]) verwendet als felderzeugende Quellen einen Satz Dipole auf der Rotationsachse, der natürlich außerhalb der gesuchten Äquipotentialflächen liegen muß und der so eingerichtet ist, daß in der Mittelebene das gewünschte Feld

† Ein ähnlicher Magnet wird von Lee-Whiting[6]) für ein hochauflösendes Comptonspektrometer zur Untersuchung der Neutroneneinfangstrahlung vorgeschlagen. Unabhängig davon begannen wir 1957 mit dem Bau eines Magneten mit obigen Anforderungen für denselben Zweck. Obgleich damals die Theorie der Polschuhoberflächenberechnung noch unvollständig war, erreichten wir mit der ersten Bearbeitung eine sehr gute Näherung mit maximalen Abweichungen bis 0.5%. Das Compton spektrometer arbeitet zur Zeit mit einer Gesamtauflösung von 1% (Auflösungsvermögen als β-Spektrometer 0.5%). [6a]).

†† Der Doppelpilzmagnet (Yo-Yo-Typ) hat den Vorteil einer guten Zugänglichkeit für das Experiment, man muss jedoch mit einem relativ grossen Streufeld rechnen. Die Forderung nach einer Näherung bis auf 0.1% gilft für Spektrometer mit einem Auflösungsvermögen von etwa 0.1%.

††† Die von Bjorken und Bitter[9]) benutzte Annahme, dass die Polschuhoberflächen gleichmässig mit magnetischen Dipolen belegt sind, kann man unter Umständen fü einen Permanentmagneten treffen. Die Autoren berechneten hiermit Shims für ein möglichst homogenes Magnetfeld eines Permanentmagneten. In unserem Falle läßt sich diese Methode jedoch nicht verwenden.

[6]) G. E. Lee-Whiting, Can. J. Phys. **38** (1960) 720.
[6a]) H. U. Gersch und R. Breitenfeld, Zentralinstitut für Kernphysik, Institutsbericht ZfK-RN 11 (1961).
[7]) B. S. Dželepov und A. A. Bašilov, Izv. A. N. SSSR Ser. Fis. **14** (1950) 263.
[8]) M. P. Glazunov und V. Spicyn, Izv. A. N. SSSR Ser. Fis. **20** (1956) 1423.
[9]) J. D. Bjorken und F. Bitter, Rev. Sci. Inst. **27** (1956) 1005.
[10]) P. H. Stoker, Ong Ping Hok, E. F. de Haan und G. J. Sizoo, Physica **20** (1954) 337.

entsteht. Für eine Berücksichtigung des Randfeldabfalles besteht hier keine Möglichkeit.

Die Oberflächen der Polschuhe erhält man auf Grund der Rechnungen geschwungen und ohne Stufen. Obwohl sich, wie eigene Erfahrungen zeigen, keine Schwierigkeiten für die maschinelle Herstellung ergeben, wird oft der einfachere Weg der Herstellung von stückweise konischen Oberflächen beschritten[11,12]). Nach unserer Meinung dürften keine erheblichen Fehler im Feldverlauf entstehen, falls der theoretisch erhaltene glatte Oberflächenverlauf durch einen geeignet gewählten stückweise konischen Verlauf ersetzt wird.

Unsere Methode gestattet die Berücksichtigung aller Effekte, die durch analytische Funktionen beschrieben werden können. Deshalb sind folgende Voraussetzungen nötig:

1.) Die Funktionentheorie ist zweidimensional. Wir können lediglich flächenhafte Probleme lösen und müssen deshalb voraussetzen, daß die Polschuhe in der 3. Dimension genügend schwach gekrümmt sind.

2.) Die Polschuhoberflächen müssen Äquipotentialflächen sein. Das verwendete Eisen wird daher als ideal weich vorausgesetzt.

3.) Die Behandlung mit Hilfe eines skalaren Potentials setzt Wirbelfreiheit des Magnetfeldes voraus, was physikalisch bedeutet, daß sich die Erregerwicklung hinreichend weit entfernt befindet.

2. Realisierung des Fokussierungsfeldes

Das in unserem Beispiel der 190°-Fokussierung geforderte rotationssymmetrische Feld ist in der Mittelebene zwischen den Polschuhen nach Lehr[13]) durch eine Potenzreihe darstellbar

$$h(x,y=0) = a_0 + a_1 \frac{x}{\rho_0} + a_2 \left(\frac{x}{\rho_0}\right)^2 + a_3 \left(\frac{x}{\rho_0}\right)^3 + a_4 \left(\frac{x}{\rho_0}\right)^4, \tag{1}$$

die unserer Genauigkeitsforderung entsprechend abgebrochen wurde (Abb. 2). Die Koordinaten sind hierbei bereits dem funktionentheoretischen Problem angepaßt, für das auf der Polschuhoberfläche $y = \pm 1$ gewählt wurde. Das Magnetfeld ist auf dem Sollkreis auf 1 normiert, für dessen Radius $\rho_0 = 10$ gilt. Die Koeffizienten sind

$$\begin{aligned} a_0 &= 1 \\ a_1 &= -0.097 \\ a_2 &= -0.579 \\ a_3 &= 0.736 \\ a_4 &= -0.530. \end{aligned}$$

Das Problem der Polschuhberechnung beschränkt sich zunächst darauf, für den geforderten Feldverlauf die Potentialflächen zu finden und aus deren Schar eine geeignete auszuwählen.

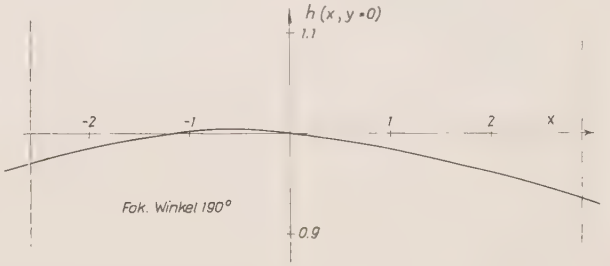

Abb. 2. Gefordertes Magnetfeld für 190°-Fokussierung höherer Ordnung.

Das skalare Potential des Magnetfeldes genügt wie vorausgesetzt der Laplaceschen Differentialgleichung

$$\Delta V = 0\,. \tag{2}$$

Diese Gleichung erfüllt sowohl der Realteil als auch der Imaginärteil jeder analytischen Funktion

$$W(z) = U(x, y) + \mathrm{i}V(x, y)\,. \tag{3}$$

Betrachtet man $V(x, y) = \text{const.}$ als Potentialflächen (-linien) und $U(x, y) = \text{const.}$ als magnetische Feldlinien, so gilt unter Benutzung der Cauchy-Riemannschen Gleichungen für die y-Komponente der magnetischen Feldstärke†

$$h_y(x, y) = \frac{\partial V}{\partial y} = \frac{\partial U}{\partial x}\,. \tag{4}$$

Damit das Magnetfeld $h_y(x, y = 0)$ auf der x-Achse der Forderung (4) genügt, muß gelten

$$U = \int h_y(x, y = 0)\,\mathrm{d}x + C\,. \tag{5}$$

[11]) S. A. Baranov, A. F. Malov und K. N. Šljagin, Prib. techn. eksp. **1** (1956) 3.

[12]) J. A. Biuner und F. R. Scott, Rev. Sci. Inst. **21** (1950) 545.

[13]) G. Lehr, Marburger Sitzungsberichte **79** (1956) 3.

† Zur Vereinfachung verlassen wir hier die übliche Vorzeichenkonvention für die Feldstärke.

Mit (1) lautet die entsprechende analytische Fortsetzung in die z-Ebene

$$W = a_0 z + a_1 \frac{z^2}{2\rho_0} + a_2 \frac{z^3}{3\rho_0^2} + a_3 \frac{z^4}{4\rho_0^3} + a_4 \frac{z^5}{5\rho_0^4}, \quad (6)$$

wobei aus Symmetriegründen die Integrationskonstante $C = 0$ gesetzt wurde.

Der Imaginärteil dieser analytischen Funktion stellt die Äquipotentialflächen dar

$$V = h(x, y = 0)\, y - \left(\frac{a_2}{3\rho_0^2} + \frac{a_3}{\rho_0^3} x\right) y^3 + \cdots . \quad (7)$$

Hier wurden nur die Terme berücksichtigt, die über der Fehlergrenze von 0.1% liegen.

Geben wir für die Polschuhoberflächen die Äquipotentialflächen $V = \pm 1$ vor, erhalten wir aus (7) Bedingungen für deren Verlauf. Sie müssen symmetrisch zueinander liegen, was auch das Auftreten von nur ungeraden Potenzen in y erklärt. Abb. 6 zeigt den Verlauf einer Polschuhoberfläche (gestrichelte Kurve). Sie stellt nur einen Teil der auftretenden Äquipotentialflächen $V = \pm 1$ dar. Das ist in einem größeren Maßstab ersichtlich, bei dem zur Vereinfachung nur die Potenzen von $h(x, y = 0)$ bis zur 2. Ordnung berücksichtigt wurden (Abb. 3).

Allgemein gilt, daß bei einem Feldverlauf, der durch eine Potenzreihe bis zur n-ten Ordnung beschrieben ist, $2(n + 1)$ Potentialflächen erscheinen,

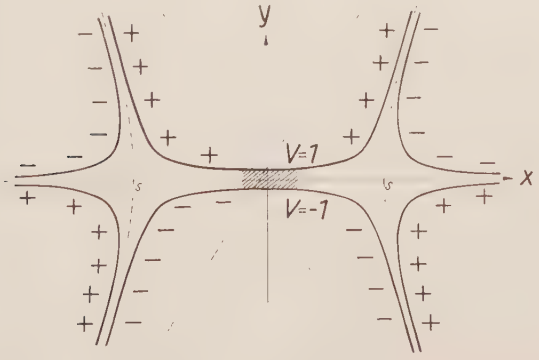

Abb. 3. Kompletter Verlauf der Polschuhoberflächen für ein Magnetfeld, das durch eine Potenzreihe 2. Ordnung dargestellt ist. In den Sattelpunkten S, die in der W-Ebene die Rolle von Verzweigungspunkten spielen, wird die Feldstärke null.

die sich im Potential abwechseln. Zur exakten Realisierung des geforderten Feldverlaufes müßten sie all durch Polschuhoberflächen ersetzt werden. Aus der Abbildung ist jedoch ersichtlich, daß das Magnetfeld, das uns etwa im schraffierten Bereich interessiert, nur durch die zentralen Potentialflächen erzeugt wird.

3. Randfeldkorrektur

Mit Hilfe der konformen Abbildung ist es möglich, eine Polschuhoberfläche anzugeben, die für ein annähernd homogenes Feld zwischen den

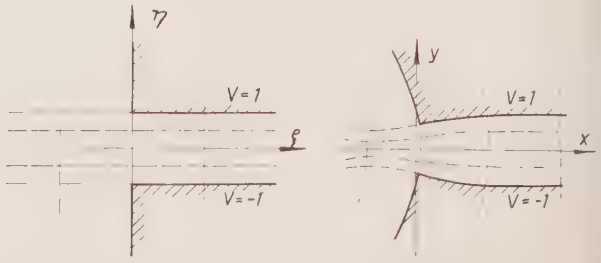

Abb. 4. Konforme Abbildung der ebenen Polschuhkanten auf eine Oberflächenform, die ein möglichst homogenes Feld erzeugen soll.

Polschuhen bis zum Rand sorgt. Eine exakte Lösung dieser Aufgabe verbietet der Eindeutigkeitssatz der Funktionentheorie. Ihm zufolge existiert nur eine einzige Potentialverteilung, falls auch nur in einem kleinen Gebiet die Feldstärke vorgeschrieben ist. Für einen homogenen Feldverlauf ist uns jedoch schon die triviale Lösung der parallelen, ebenen Polschuhoberflächen bekannt. Eine Randkorrektur wird also immer nur eine Näherung bleiben können. Es muß der Diskussion überlassen bleiben, eine geeignete Korrektur auf Grund zusätzlicher Bedingungen und Forderungen auszuwählen.

Das Feld in der Mittelebene zwischen den Kanten zweier ebener Polschuhe läßt sich mittels der der Schwarz-Christoffel-Transformation bestimmen (siehe z.B.[14])).

Legt man die Polschuhkanten – wie auf der linken Seite der Abb. 4 – auf die η-Achse einer ζ-Ebene und gibt den Polschuhoberflächen die Potentiale $V = \pm 1$, so erhält man für das Feld $h_\eta(\xi)$ bzw. die Differenz zum Feld weit zwischen den Polschuhen $\varepsilon(\xi) = 1 - h_\eta(\xi)$

$$\xi = \frac{1}{\pi}\left(\ln \frac{1 + h_\eta}{1 - h_\eta} - \frac{2}{h_\eta}\right) = \frac{1}{\pi}\left(\ln \frac{2 - \varepsilon}{\varepsilon} - \frac{2}{1 - \varepsilon}\right). \quad (8)$$

[14]) M. Morse und H. Feshbach, Methods of Theoretical Physics, Vol. I (New York, Toronto, London 1953) p. 445.

Das Feld läßt sich nicht explizit darstellen. Abb. 5 zeigt den Verlauf in der Nähe der Polschuhränder.

3.1. FORDERUNG NACH EINEM HOMOGENEN FELD BIS ZUM RAND

Fordert man statt des berechneten abfallenden Feldes zwischen den Polschuhen ein homogenes

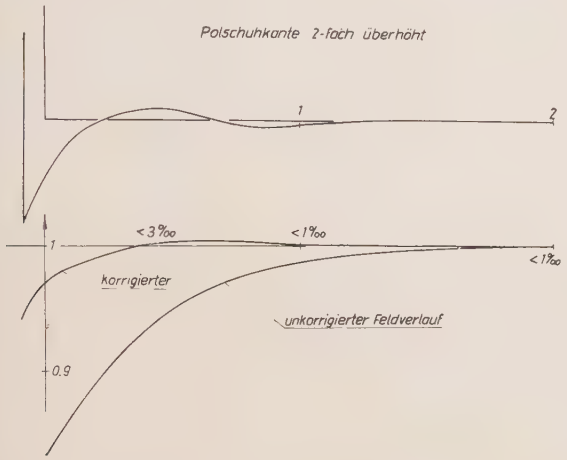

Abb. 5. Unkorrigierter und für die Forderung nach einem homogenen Feld korrigierter Polschuhverlauf in der Nähe der Kante. Der Verlauf an den Aussenseiten ist unwesentlich und wurde deshalb eben gewählt.

Feld, wird dies anschaulich nur möglich sein, wenn sich die Polschuhe nach den Kanten zu gegenseitig nähern.

Wir können uns vorstellen, daß die so geforderten Äquipotentialflächen in Abb. 4 (rechte Skizze) aus den ebenen Polschuhflächen (linke Skizze) durch eine konforme Abbildung hervorgegangen sind.

In der z-Ebene soll das Feld zwischen den Polschuhen homogen sein

$$h_y(x, y = 0) = \frac{\partial U(x, y = 0)}{\partial x} = 1 \,. \tag{9}$$

Diese konforme Abbildung

$$\zeta(z) = \xi(x, y) + \mathrm{i}\eta\,(x, y) \tag{10}$$

läßt sich mit Hilfe der obigen Forderung

$$\frac{\partial U}{\partial x} = \frac{\partial U}{\partial \xi}\frac{\partial \xi}{\partial x} + \frac{\partial U}{\partial \eta}\frac{\partial \eta}{\partial x} = 1 \tag{11}$$

und der Symmetrieeigenschaft

$$\frac{\partial U}{\partial \eta} = 0 \qquad \text{für} \qquad y = 0 \tag{12}$$

berechnen. Da $\partial U/\partial \xi = h_\eta(\xi, \eta = 0)$ das in Gleichung (8) für den ebenen Fall berechnete Randfeld darstellt, lautet die Bestimmungsgleichung für die gesuchte konforme Abbildung

$$x = \int h_\eta\,(\xi, \eta = 0)\,\mathrm{d}\xi + C = \xi + \int_\xi^\infty \varepsilon(\xi)\,\mathrm{d}\xi \,. \tag{13}$$

Die Wahl der Integrationsgrenzen folgt aus der Forderung, daß sich die Abbildung für große ξ der trivialen Abbildung nähert. Gelingt es, diese Funktion $x(\xi)$ in die z-Ebene analytisch fortzusetzen – $z(\zeta)$ –, so erhält man aus der Schar der Flächen mit konstanten η die gesuchten Polschuhoberflächen.

Diese Fortsetzung ist wegen des oben erwähnten Eindeutigkeitsprinzips nicht möglich. Es soll deshalb versucht werden, für $x(\xi)$ eine Funktion zu finden, die im Gebiet zwischen den Polschuhen eine möglichst gute Annäherung an das homogene Feld liefert und analytisch in die z-Ebene fortsetzbar ist. Nennen wir die Näherungsfunktion für das Integral in (13) $J\,(\xi)$, so erhalten wir ein Magnetfeld mit den aus dieser analytischen Fortsetzung berechneten Polschuhen:

$$h_y(x, y = 0) = h_\eta(\xi, \eta = 0)\,\frac{\partial \xi}{\partial x} = \frac{1 - \varepsilon(\xi)}{1 + \dfrac{\mathrm{d}J(\xi)}{\mathrm{d}\xi}} \,. \tag{14}$$

Deshalb werden wir für die Funktion $J(\xi)$ eine möglichst gute Näherung ihrer Ableitung $-\,\mathrm{d}J/\mathrm{d}\xi$ an die Randfeldfunktion $\varepsilon(\xi)$ verlangen. Wir wählen für $J(\xi)$ eine Gaußfunktion

$$J(\xi) = b\,\mathrm{e}^{-a(\xi+c)^2} \,, \tag{15}$$

deren 3 freie Parameter noch besonderen Gesichtspunkten gehorchen müssen.

Während zwischen den Polschuhen eine möglichst gute Annäherung angestrebt werden muß†, ist außerhalb der Polschuhe darauf zu achten, daß die Näherungsfunktion schnell abnimmt und gegen null geht. Dann nimmt auch das Feld schnell genug ab, ohne daß große Streuverluste eintreten.

Die Verwendung von nur 3 Parametern läßt noch keine befriedigende Näherung zu. Deshalb wählten wir eine weitere Korrekturfunktion derselben Form und bestimmten die jetzt vorhandenen Parameter unter Berücksichtigung der beschriebenen Forderungen.

† Eine Übereinstimmung der Asymptoten beider Funktionen ist wegen der Genauigkeitsforderung nicht nötig.

Die so erhaltene Näherungsfunktion

$$-\frac{\mathrm{d}J}{\mathrm{d}\xi} = \frac{\xi + 0.7}{4}\,\mathrm{e}^{-(\xi+0.7)^2} - \frac{\xi}{15}\,\mathrm{e}^{-2\xi^2}, \qquad (16)$$

bei der also die Parameter

$a_1 = 1 \quad b_1 = 0.125 \quad c_1 = 0.7$
$a_2 = 2 \quad b_2 = -0.0167 \quad c_2 = 0$

verwendet wurden, stimmt mit $\varepsilon(\xi)$ gut überein.

Der Fehler

$$1 - h_y(x, y = 0) \approx \varepsilon(\xi) + \frac{\mathrm{d}J(\xi)}{\mathrm{d}\xi} \qquad (17)$$

ist nach (14) gleichzeitig die Abweichung vom homogenen Feld. Abb. 5 zeigt den Feldabfall an den unkorrigierten und korrigierten Polschuhrändern.

Zur Realisierung dieses korrigierten Feldverlaufes muß die Bestimmungsgleichung für die konforme Abbildung

$$x = \xi + J(\xi) = \xi + 0.125\,\mathrm{e}^{-(\xi+0.7)^2} - 0.0167\,\mathrm{e}^{-2\xi^2} \qquad (18)$$

in die z-Ebene fortgesetzt werden

$$z = \zeta + J(\zeta)\,. \qquad (19)$$

In Real- und Imaginärteil separiert, folgen daraus die Transformationsgleichungen der konformen Abbildung

$$\begin{aligned} x &= \xi + \sum_{1,2} b_i\,\mathrm{e}^{-a_i(\xi+c_i)^2}\,\mathrm{e}^{a_i\eta^2}\cos 2a_i(\xi + c_i)\eta \\ y &= \eta - \sum_{1,2} b_i\,\mathrm{e}^{-a_i(\xi+c_i)^2}\,\mathrm{e}^{a_i\eta^2}\sin 2a_i(\xi + c_i)\eta\,. \end{aligned} \qquad (20)$$

Die damit erhaltenen Potentialflächen für $\eta = 1$ stellen die verlangten Polschuhoberflächenformen in der Nähe der Ecken dar und haben den in Abb. 5 gezeigten Verlauf†.

Die zugehörigen Koordinaten des Potentialverlaufes für $\eta = 1$ liefert Tabelle 1.

Wegen des Auftretens von Singularitäten zwischen den Polschuhen ist eine unbegrenzte Näherung an das geforderte homogene Feld nicht möglich. Durch geschickte Wahl der Parameter kann jedoch weitgehend die Forderung nach guter Ausnutzung des Raumes zwischen den Polschuhen befriedigt werden.

Tabelle 1

x	$1 - y$
— 0.087	0.205
— 0.015	0.121
0.088	0.045
0.211	0.003
0.343	— 0.018
0.472	— 0.022
0.590	— 0.012
0.698	+ 0.001
0.799	0.011
0.993	0.008
1.191	0.003
1.396	— 0.002
1.599	— 0.001
2	0

3.2. Additive Behandlung der Korrekturen

Im 2. Abschnitt erhielten wir eine Oberflächenfunktion, die das von uns geforderte Sollfeld liefert. Die wirklichen Polschuhe sind jedoch begrenzt. Trotzdem soll ihr Feld bis zu den Rändern dem Sollfeld entsprechen. Wir werden deshalb den Randeffekten Rechnung tragen müssen.

Die Bedingung für die konforme Abbildung aus der ζ- in die z-Ebene lautet jetzt

$$\frac{\mathrm{d}x}{\mathrm{d}\xi} = \frac{1 - \varepsilon(\xi)}{h_y(x)}\,, \qquad (21)$$

wobei $h_y(x)$ nicht homogen ist, sondern den in Gleichung (1) vorgeschriebenen Verlauf hat. Außerhalb des Randfeldeinflusses entspricht das der Forderung (5)††.

Diese Gleichung gestattet, die für unser Problem geforderte konforme Abbildung in 2 Schritten – etwa über eine Z-Ebene – vorzunehmen, für die die Gleichungen auf der x- bzw. X-Achse lauten

$$[1 - \varepsilon(\xi)]\,\mathrm{d}\xi = \mathrm{d}X$$

$$\mathrm{d}X = h_y(x)\,\mathrm{d}x\,. \qquad (22)$$

Die Weiterführung der Betrachtung zeigt, daß eine additive Überlagerung der Randfeldkorrektur

† Eine Berechnung von Shims mit der Funktionentheorie, wie sie Rose[15]) durchgeführt hat, führt auch zu einer relativ guten Näherung bei der Korrektur der Randeffekte. Diese Methode verfügt jedoch über weniger Parameter als unsere Methode.

†† In unserem speziellen Problem greifen die Randeffekte nicht aufeinander über, da sie bereits in einer Entfernung, die dem Polschuhabstand entspricht, unter $1\,{}^0/_{00}$ abgefallen sind.

[15]) M. E. Rose, Phys. Rev. 53 (1938) 715.

(Abbildung von der ζ – in die Z-Ebene) auf die im zweiten Abschnitt berechnete Oberflächenform für die Realisierung des geforderten Fokussierungsfeldes (Abbildung von der Z- in die z-Ebene) möglich ist. Es entsteht lediglich eine zusätzliche Korrektur zweiter Ordnung, die aus dem Produkt der Randfeldkorrektur mit der Abweichung des geforderten Magnetfeldes vom homogenen Feld $1\text{-}h_y(x)$ besteht. Diese Störungskorrektur überschreitet in unserem Falle selbst an den Polschuhkanten nicht 1% und verschwindet in dem uns interessierenden Gebiet.

Betrachten wir die Differenz zwischen den beiden Potentialen als Störung $V = V_0 + V_1$, so erhalten wir

$$\left(\frac{\partial^2}{\partial\rho^2} + \frac{\partial^2}{\partial y^2} + \frac{\partial}{\rho\partial\rho}\right) V_1 = -\frac{\partial}{\rho\partial\rho} V_0 \,, \qquad (25)$$

wobei unter Umständen das 3. Glied als Term zweiter Ordnung vernachlässigt werden kann.

Aus dieser Differentialgleichung läßt sich prinzipiell das Zusatzpotential V_1 bestimmen, das in der Mittelebene zusammen mit seinen ersten und zweiten Ableitungen null ist.

Das so entstehende exakte Potential V für das

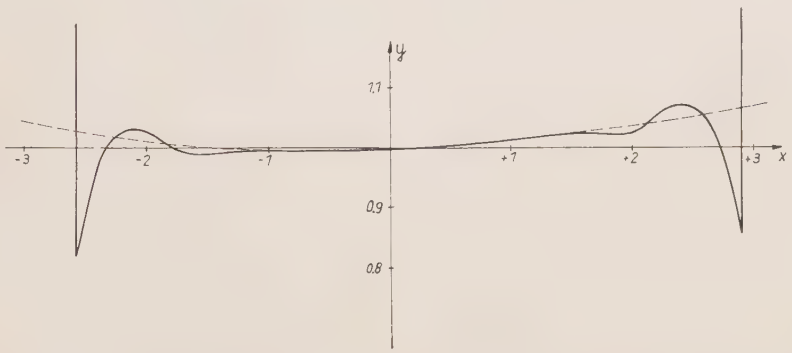

Abb. 6. Polschuhoberflächenform des Doppelpilzmagneten zur Erzeugung des für die Fokussierung nötigen Magnetfeldes mit und ohne Randfeldkorrekturen (5 – fach überhöht).

Kombinieren wir in unserem Beispiel den im 2. Abschnitt berechneten Oberflächenverlauf und die Randkorrektur, erhalten wir den in Abb. 6 dargestellten Verlauf in den eingeführten normierten Koordinaten.

4. Die Rundung der Polschuhe

Inwieweit eine funktionentheoretische Behandlung der gestellten Aufgabe genügt, hängt vom Verhältnis des Polschuhabstandes zum Krümmungsradius ab, welches zunächst als sehr klein angenommen wurde.

Im wirbel- und quellenfreien Raum gilt

$$\Delta V = \left(\frac{\partial^2}{\partial\rho^2} + \frac{\partial^2}{\partial y^2} + \frac{\partial}{\rho\partial\rho}\right) V = 0 \,, \qquad (23)$$

wobei die Bezeichnungen der Abb. 1 verwendet werden. Gelöst wurde bisher das funktionentheoretische Problem

$$\Delta V_0 = \left(\frac{\partial^2}{\partial\rho^2} + \frac{\partial^2}{\partial y^2}\right) V_0 = 0 \,. \qquad (24)$$

räumliche Problem wird dann an einer anderen Stelle gleich 1, und zwar für kleinere Ordinatenwerte, wenn V_1 positiv ist und umgekehrt. Wir wollen uns mit einer Abschätzung begnügen, die man in der Nähe des homogenen Feldes zwischen den Polschuhen durchführen kann. Dort ist auch das erste Glied in (25) zu vernachlässigen, und man erhält, wenn man $\partial V_0/\partial\rho$ aus der analytischen Fortsetzung des Potentials (7) entnimmt

$$\frac{\partial V_0}{\partial x} = \frac{\partial h_y(x, y=0)}{\partial x} y - \left(\left(\frac{a_3}{\rho_0{}^3} y^3\right)\right) , \qquad (26)$$

aus (25)

$$V_1 = -\frac{1}{\rho}\int\int_0^{y_0} \frac{\partial V_0}{\partial x}\,\mathrm{d}y\,\mathrm{d}y \approx -\frac{1}{\rho}\frac{\partial h_y(x, y=0)}{\partial x}\frac{y_0{}^3}{6} \,, \qquad (27)$$

wobei die obere Grenze y_0 die Ordinate ist, bei der $V_0 = 1$ war.

Für die Kanten $\rho_i = 7.4$ und $\rho_a = 12.9$ erhalten wir $V_1 = -0.0007$ bzw. $+0.00035$. Demnach müßten die inneren Kanten um 0.7 ‰ weiter

auseinander, die äußeren Kanten um 0.35‰ weiter zusammengelegt werden.

Diese Ergebnisse sind in guter Übereinstimmung mit den durch Vergleich mit der Theorie von Stoker[10]) erhaltenen Abweichungen. Wegen ihrer Geringfügigkeit brauchen sie nicht berücksichtigt zu werden. Sie zeigen jedoch, daß schon bei unserer Aufgabe einer Berechnung in der Ebene nichts im Wege steht.

5. Die Nähe der Erregerspulse

Die Erregerspule erhöht in ihrer Nähe das Magnetfeld. Diesen Einfluß machen sich z.B. Stoker *et al.*[10]) zunutze, indem sie ein äußeres Rückschlußjoch verwenden. Die so erzielte Feldbeeinflussung macht eine Korrektur des Randfeldes jedoch nicht in allen Fällen überflüssig.

Der Einfluß der Erregerspule ist schwer zu erfassen. Man kann davon ausgehen, daß in dem Falle, in dem der gesamte Erregerstrom durch ein Band direkt an den Kanten der Polschuhe fließt, keine Randeffekte auftreten können. Um wenigstens zu einer Abschätzung zu kommen, haben wir den Einfluß des Bandes als Differenz der Felder mit und ohne Berücksichtigung der Erregung angenommen. Dieses Differenzfeld ist das uns bekannte $\varepsilon(x)$. Für den Realfall verteilen wir diesen Einfluß auf die ganze Spule. Nimmt man außerdem zu dieser Abschätzung nur den Teil der Spule, der zwischen den Polschuhen liegt, so ergibt sich in unserem Falle eine Verminderung der inneren Randeffekte um 10%. Man wird also hier von vornherein nur 90% der berechneten Randfeldkorrektur benutzen.

Diese halbempirische Methode kann zu Feldabweichungen an den Kanten führen, die jedoch nach der im 3. Abschnitt beschriebenen allgemeinen Methode korrigiert werden können.

6. Einflüsse der Hysteresis des Eisens

Die Betrachtung der Polschuhoberflächen als Äquipotentialflächen ist nur unter der Bedingung eines ideal weichen Eisens zulässig. In der Praxis wird das Eisen einen nicht zu vernachlässigenden magnetischen Widerstand haben, der, solange er für jede Feldlinie im Polschuh gleich ist, nicht stört. Verschieden lange Wege der Feldlinien und die Hysteresiseigenschaften sorgen jedoch für Abweichungen. Dadurch wird der Feldverlauf zwischen den Polschuhen im geringen Maße von der Feldstärke und der Vorgeschichte abhängen.

Allgemein ist daher bei der Konstruktion eines Magneten zu berücksichtigen, daß der magnetische Widerstand des Eisens nur einige Promille von dem des Luftspalts beträgt und daß wegen der geringen Anfangspermeabilität bei nicht zu kleinen Feldstärken gearbeitet wird.

Für große Induktionen im Eisen treten allerdings Sättigungserscheinungen auf. Wichtigste Maßnahme neben der Wahl einer guten Weicheisensorte ist die entsprechend große Dimensionierung aller Querschnitte.

Der wesentlichste Sättigungseffekt wird sich an scharfen Kanten bemerkbar machen. Die Äquipotentialflächen werden hier in das Eisen hineingezogen. Dieser Effekt hat eine feldstärkeabhängige Vergrößerung des Randabfalles zur Folge.

Langer und Cook[16]) verwenden auch auf den Innenflächen der Polschuhe stufenförmige Absätze. Da hier an den jeweils 8 Kanten starke Sättigungserscheinungen eintreten müssen, ist auch mit einer entsprechenden Abhängigkeit des Feldverlaufes von der Feldstärke zu rechnen. Aus diesem Grunde sind glatte oder stückweise konische Polschuhoberflächen vorzuziehen.

Eine rechnerische Korrektur der Hysteresiseinflüsse ist wenig sinnvoll, da sie feldabhängig durchgeführt werden müßte. Es gibt verschiedene Kunstgriffe, diese Einflüsse klein zu halten oder zu kompensieren.

Ich danke Herrn Prof. Dr. K. F. Alexander für anregende Diskussionen und Hinweise.

[16]) L. M. Langer und C. S. Cook, Rev. Sci. Inst. **19** (1948) 257.

NUCLEAR INSTRUMENTS AND METHODS 13 (1961) 305–308; NORTH-HOLLAND PUBLISHING CO.

SOLID-STATE DETECTOR FOR MONITORING 14-MeV NEUTRON PRODUCTION†

R. CEDARLUND, A. HORN and M. SCOLNICK

Lawrence Radiation Laboratory, University of California Livermore, California

Received 4 April 1961

This paper describes the use of a silicon p-n junction as an alpha monitor for the $H^2(H^3, n^1)He^4$ reaction on the Cockcroft-Walton accelerator. The use of the p-n junction to monitor the proton contribution from the the D-D reaction is also mentioned. Various graphs illustrate alpha and proton pulseheight distributions, their dependence on bias voltage, and the ratio $\frac{\text{proton pulse height}}{\text{alpha pulse height}}$ vs bias voltage. Conclusions are also reported.

1. Introduction

In monitoring the production of 14-MeV neutrons from the D-T reaction it is customary to use an alpha-particle detector. Some of the more desirable characteristics of such a counter are:

1. Small size and mass—this insures that few neutrons will be scattered back into the experimental setup.

2. Fast response—to minimize dead-time correction under high count-rate conditions; possible application in time-of-flight work.

3. Stability—response independent of time and not subject to variations in behavior due to details of construction.

4. Resistance to radiation damage.

5. Low maintenance—long useful life and easily replaceable without cumbersome precautions.

6. Energy-dependent response—to insure that the desired signal is distinguishable from other signals and from noise. In the course of producing 14-MeV neutrons from a tritium target the deuteron beam loads the target with deuterium and hence produces low-energy ($\approx$ 3 MeV) neutrons through the D-D reaction. For some experiments these low-energy neutrons may contribute troublesome backgrounds whose level changes with time. Since the D-D reaction produces a 3-MeV proton a significant fraction of the time, the presence of low-energy neutrons due to deuterium build-up may be monitored by a charged particle detector which can distinguish between 3-MeV protons and 3-MeV alpha particles. This can be done with a detector whose thickness is small compared with the range of a 3-MeV proton.

Proportional gas counters used as alpha detectors have several disadvantages:

1. They are not as small and as low in mass as desired.

2. Very painstaking maintenance is required—component parts must be washed in solvent and thereafter baked out while being evacuated. The thin Mylar window is delicate and requires careful handling.

3. When evacuating the beam-pipe target assembly to which this unit is attached, a cautious pumpdown is required so as not to rupture the window.

4. A clean vacuum-counter filling system is necessary on standby at all times.

5. A high voltage is required for operation—although hig-voltage supplies are a commonplace item, a certain hazard exists when one considers the frequency with which these must be connected and disconnected in remote accelerator bombardment pits.

Silicon p-n junctions, on the other hand, surmount most of these difficulties. In order to be useful for our purpose, however, they must have a very thin depletion layer. Most of our solid-state detectors to date have had too thick a depletion layer. Recently, however, we have received a unit from R.C.A. of Canada which appeared to be appropriate

† This work was performed under the auspices of the U.S. Atomic Energy Commission.

for our application. It was a type D silicon junction having a surface detecting area of 20 mm².

2. Experimental Setup

The silicon p–n junction was adapted to the 135° arm of the 90°–135° alpha-monitor target assembly, which is shown in fig. 1. A conventional gas-filled proportional counter was mounted on the 90° arm.

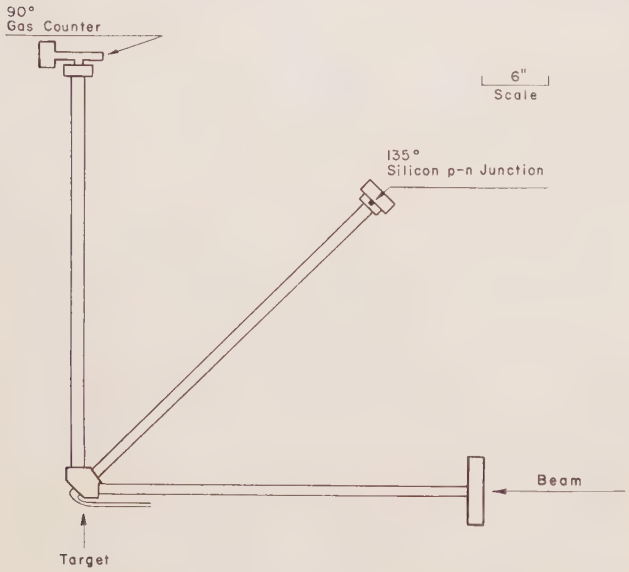

Fig. 1. Diagram of alpha-monitor target assembly.

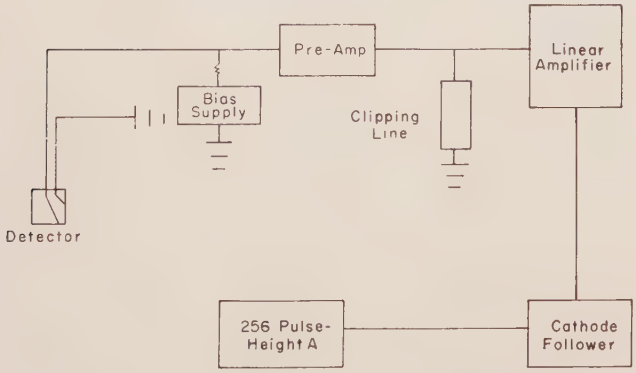

Fig. 2. Block diagram of the detector electronics.

A normal tritium target was used. In addition to tritium this target had acquired a deuterium loading from previous deuteron bombardment. This factor made it possible to view simultaneously the pulse-height spectra of alphas from the D-T reaction, as well as any contribution due to protons from the D-D reaction. Figure 2 shows a block diagram of the detector electronics.

In order to stop the 350-keV elastically scattered deuterons, a 1-mg/cm² Mylar foil was placed in front of the detector. This was subsequently found to be unnecessary and so was removed since the detector apparently had a sufficiently thick surface layer.

3. Observations

p–n junction alpha spectra were observed on the 256 pulse-height analyzer for bias voltages of 2, 4, 6, 8, 10, 12, 14, 16, 20,, 30, 40, and 50 volts. Figure 3 shows a sample pulse-height distribution of protons and alpha particles. This spectrum compares favorably with that observed[1]) in a gas proportional counter. For all detector bias voltages observed between 2 and 30 volts inclusive, we obtained very good resolution of the alpha spectrum. Good resolution of the proton spectrum was obtained with detector bias voltages of 4 through 20 volts. At 40 volts bias and above, the depletion-layer thickness became commensurate with the proton range and the proton spectrum merged with the alpha spectrum. Figure 4, which shows the pulse-height peaks vs detector bias voltage, illustrates how the pulse-height peaks begin to approach each other rapidly above a detector bias voltage of 40 volts. Note that this graph does not show the energy spread of each spectrum, merely the peaks.

In many instances the response of a detector to more than one particle is undesirable, but in this case it provides a definite advantage. The accompanying graphs show that not only is the detector well suited to monitor the alpha particles from the D-T reaction, but also provides a means of distinguishing that portion of the neutrons which is produced by the D-D reaction. Use of dual-channel differential discrimination enables one to count both products separately and simultaneously. Figure 5 shows a plot of the ratio

$$\frac{\text{pulse height of proton spectrum}}{\text{pulse height of alpha spectrum}}$$

detector bias voltage. This graph emphasizes the fact that in order to monitor protons as well as alpha particles from the previously mentioned reactions,

[1]) Benveniste, Mitchell, Schrader and Zenger, University of California Radiation Laboratory Report UCRL 5619 (1959).

one would best do so by using a low detector bias voltage.

Throughout the run, the average neutron yield at the target, as measured by the 90° gas alpha counter, was about 1.5×10^{10} n/sec. This is about 1×10^5 n/cm^2/sec at the position of the detector. We continued to observe and check the spectra periodically for approximately eleven hours total run on two consecutive days. The total neutron radiation flux to which the detector was exposed was approximately 4×10^9 n/cm^2. A constant detector bias of 14 volts was used for this check. The pulse height of the alpha and proton spectra varied only a few channels throughout. The detector did not show any noticeable signs of deterioration during the observed run, either from radiation damage or voltage breakdown. The peak of the pulse height of the noise spectrum remained fairly constant over the range of 2 to 50 volts bias.

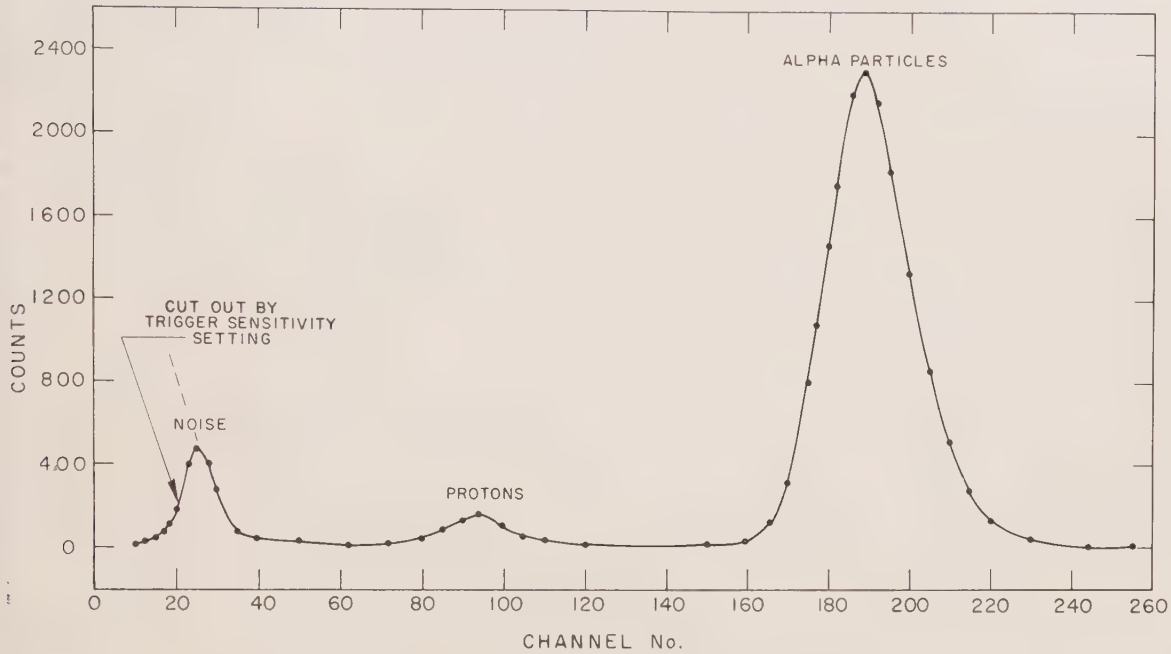

Fig. 3. Pulse-height distribution of protons and alpha particles.

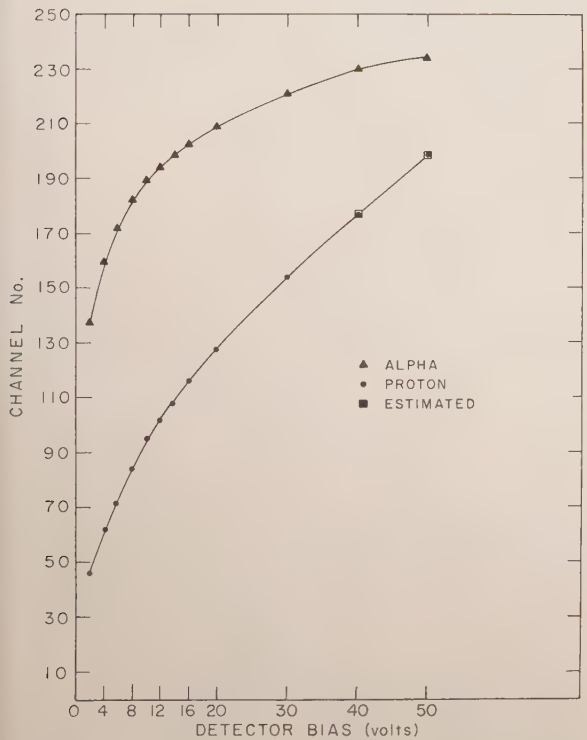

Fig. 4. Pulse-height peaks versus detector bias voltage.

4. Conclusions

In our opinion silicon p–n junctions are admirably suited to the task of monitoring the D-T reaction and/or the D-D reaction for the following reasons:

1. Small size.
2. Easily maintained.
3. Low operating voltage.
4. Ability to monitor alpha particles and protons of 3 MeV.

5. Ability to distinguish between protons and alpha particles of 3 MeV.

6. No change in detection characteristics due to irradiation.

Acknowledgements

The authors wish to express their gratitude to Dr. Jack Benveniste for his generous help and advice both during the experiment and in the writing of this report.

We also wish to thank Arthur Mitchell and Rex Booth for their help and for the latter's loan of a low noise pre-amp. Finally, we thanks Dr. Richard Hill and Mr. Murrey Goldberg for giving us the silicon p–n junction.

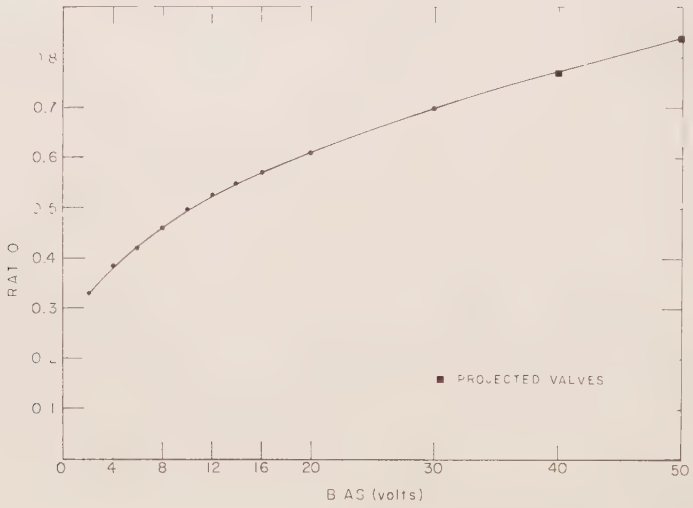

Fig. 5. Pulse-height peak ratio (p/α) versus detector bias voltage.

NUCLEAR INSTRUMENTS AND METHODS 13 (1961) 309–312; NORTH-HOLLAND PUBLISHING CO.

OPTIMUM LOCATION OF BF_3 COUNTERS IN A NEUTRON MODERATOR

C. W. PETERS and A. L. SNYDER

U.S. Naval Research Laboratory, Washington 25, D.C.

Received 31 July 1961

A method has been developed for determining the optimum location of several BF_3 counters in a moderating medium, such as water. This method, which gives a maximum sensitivity to a neutron flux with a given energy spectrum, requires the use of data on (a) the interaction characteristics for sets of two and three counters and (b) the relative count rate profiles along the axis of symmetry of the moderator and along a line perpendicular to the axis of symmetry. In addition to a description of the method, experimental verification is presented for the case of three BF_3 counters in a rectangular water moderator.

1. Introduction

A sensitive neutron detector may consist of one or more proportional counters filled with boron trifluoride (BF_3) gas operated in a neutron moderating medium such as water or paraffin[1]).

A method will be described for determining the optimum location of the counters, in a detector geometry such as that shown in fig. 1 so as to achieve a maximum neutron sensitivity to a neutron flux with a given energy spectrum. This method is expected to hold for other neutron detectors, such as fission counters or boron lined counters, and for moderator geometries other than the rectangular parallelepiped indicated in fig. 1.

2. BF_3 Counters and Electronics

The proportional counters[2]) employed in developing this method had a 0.032 in. thick, 1 in o.d. aluminum cathode and a 0.002 in. o.d. tungsten anode; the active anode length was 12 in. which was defined by a guard ring at one end and a glass bead at the other end. They were filled with BF_3, which was 96% enriched with B^{10}, to a nominal pressure of 60 cm of Hg.

The counters were selected such that their spectra matched at an operating voltage of 2700 V. Counters with matched spectra are now available from the manufacturer.

[1]) B. B. Rossi and H. H. Staub, *Ionization Chambers and Counters*, (McGraw-Hill, New York, 1949).

[2]) Manufactured by Radiation Counter Laboratories, Skokie, Illinois.

When two or more counters are operated in parallel, the input capacity relative to one counter increases, thus resulting in a loss of gain. By connecting a variable capacitor in parallel with the cathode follower input and adjusting it such that the input capacity remains constant, the count rate of two or more counters can be compared with the count rate from one counter without changing the amplifier gain, discriminator setting, or the input capacity.

3. Moderator and Source Geometry

A Po-Be source, mounted in one face of a paraffin block, was located at one end of a "cave" consisting of water-filled cans on the top and sides, a concrete floor, and a large rectangular water tank as shown in fig. 1. A smaller tank (15.5 × 41 × 42 cm) was filled with water to a depth of 41 cm and placed at the other end of the cave for use as the moderating medium. A sheet of cadium, placed across the open end of the cave about 3 cm from the moderator tank was used in order to reduce the flux of thermal neutrons.

The BF_3 counters were placed inside of water tight, 0.032 in. thick, brass walled tubes. The counters were put into the moderator tank as shown in fig. 2 such that the active length was below the surface of the water and their axes were parallel.

4. Observed BF_3 Counter Response

Curve A of fig. 3 shows the response from one counter as a function of the centerline to centerline

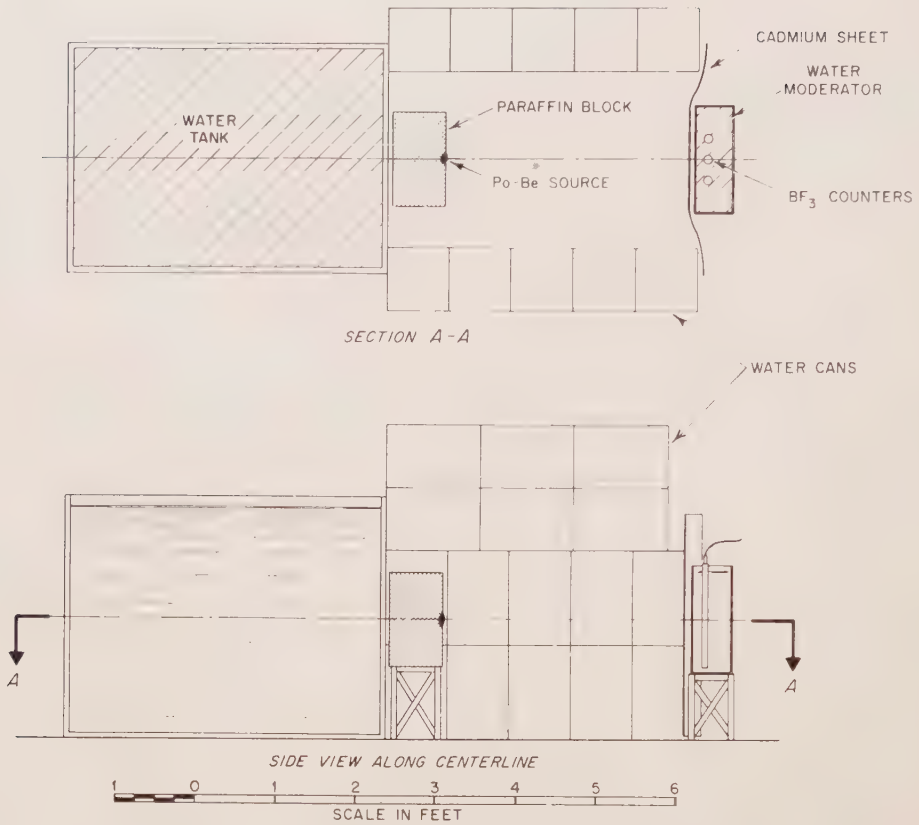

Fig. 1. Side and top views of partially moderated Po-Be neutron source, shielding, and detector arrangement.

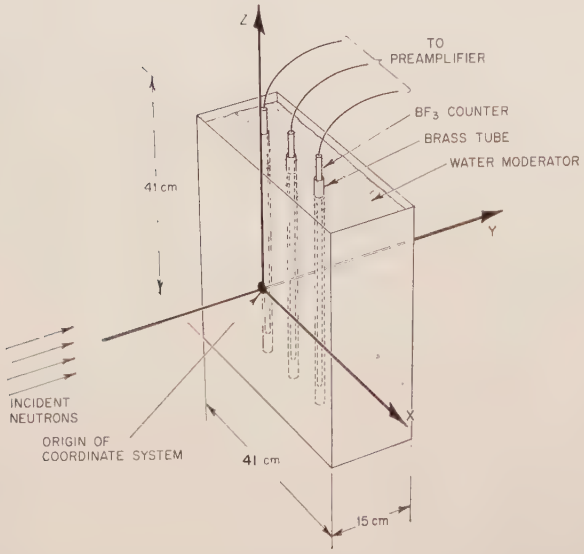

Fig. 2. Small rectangular moderator tank with three BF_3 counters. A cartesian coordinate system is indicated for reference.

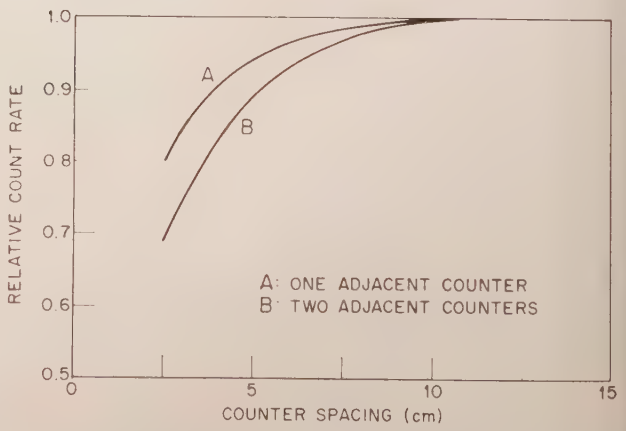

Fig. 3. Relative count rate versus centerline to centerline counter spacing for, A—one adjacent counter and B—two adjacent counters.

distance between it and a neighboring counter. The latter is moved along an isodose line common to both counters. Curve B of fig. 3 illustrates the variation of the response from one counter as a function of the distance, along an isodose line, between it and two counters which are equally spaced on either side of the counter being monitored. These data were taken in the large tank where the isodose lines are nearly straight lines at a distance of 10 cm. or more from the face of the tank, with a counter arrangement similar to that shown in fig. 2.

A cartesian coordinate system with the origin located in the center of the neutron incident face of the detector moderator is indicated in fig. 2. The relative count rate from one BF_3 counter as a function of Y for X equal to zero and $\pm$ 10 cm is shown in fig. 4. The peak count rate occurs at Y equal to 3.5 cm.

The count rate profile as a function of Y for X equal to zero for a bare Po-Be source was found to be similar to the profile shown in fig. 4 but with the peak at 4 cm. Omohundro[3]) observed a profile with an unmoderated fission neutron source similar to that shown in fig. 4 with the peak at 3.5 cm.

The relative count rate from one BF_3 counter as a function of X for Y equal to 3.5 cm is shown in fig. 5. The count rate was extrapolated to zero at the extrapolated boundary of the moderator.

5. Calculating the Response from Several BF_3 Counters

The count rate for one BF_3 counter relative to the peak count rate at (X, Y) equal to (0, 3.5 cm) can be calculated for any (X, Y) from the data in figs. 4 and 5. Furthermore, by combining the appropriate two or three counter interaction data shown in fig. 3 with the count rate profiles shown in figs. 4 and 5, the count rate from two or more counters can be calculated relative to the peak count rate from one counter at (X, Y) equal to (0, 3.5 cm).

For example, consider the case of five counters, with their axes aligned such that they are equally spaced and parallel in the plane, Y equal to 3.5 cm.

Let:

X_i = location of ith counter along the line Y = 3.5 cm.

X_0 = distance between axes of adjacent counters

$f_2(X_0)$ = two counter interaction shown in fig. 3, Curve A

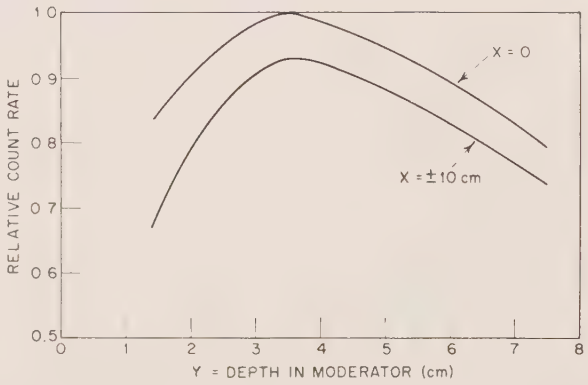

Fig. 4. Relative count rate versus the distance of the centerline of the counter from the front face of the moderator along the lines X = 0 and X = $\pm$ 10 cm.

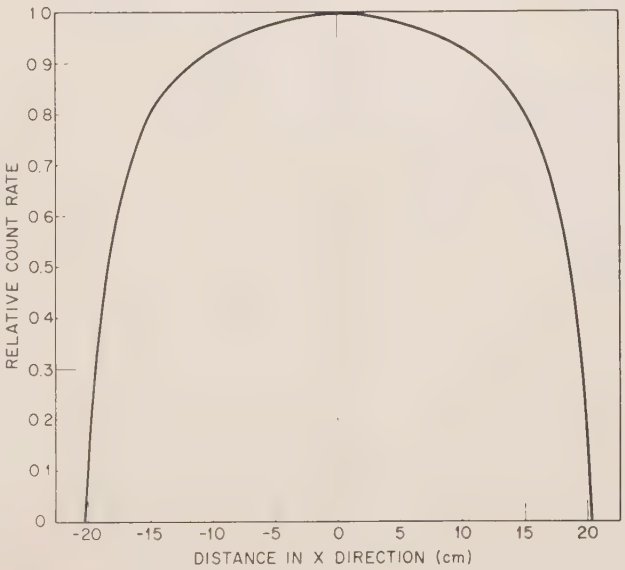

Fig. 5. Relative count rate versus X for Y = 3.5 cm.

$f_3(X_0)$ = three counter interaction shown in fig. 3, Curve B

$\phi(X_i)$ = relative count rate shown in fig. 5

C_5 = count rate of five counters relative to one counter at (X, Y) equal to (0, 3.5 cm).

[3]) R. J. Omohundro, U. S. Naval Research Laboratory, Washington 25, D.C., Personal Communication.

Then: $C_5(X_0) = \phi(X_1)f_2(X_0) + \phi(X_2)f_3(X_0) + + \phi(X_3)f_3(X_0) + \phi(X_4)f_3(X_0) + \phi(X_5)f_2(X_0)$ where the counters are numbered consecutively beginning at one end of the row. Since $\phi(X_i)$ (fig. 5) is symmetrical about $X = 0$, the middle counter of an odd array should be placed at $X = 0$.

So: $X_1 = -X_5$
$X_2 = -X_4$
$X_3 = 0$
$X_0 = X_2 - X_4$
$2X_0 = X_1 - X_5.$

And: $\phi(0) = 1$
$\phi(X_1) = \phi(-X_1) = \phi(X_5)$

leaving:

$$C_5(X_0) = 2\phi(X_1)f_2(X_0) + 2\phi(X_2)f_3(X_0) + + 1\,f_3(X_0) = = 2\phi(2X_0)f_2(X_0) + [2\phi(X_0) + 1]\,f_3(X_0).$$

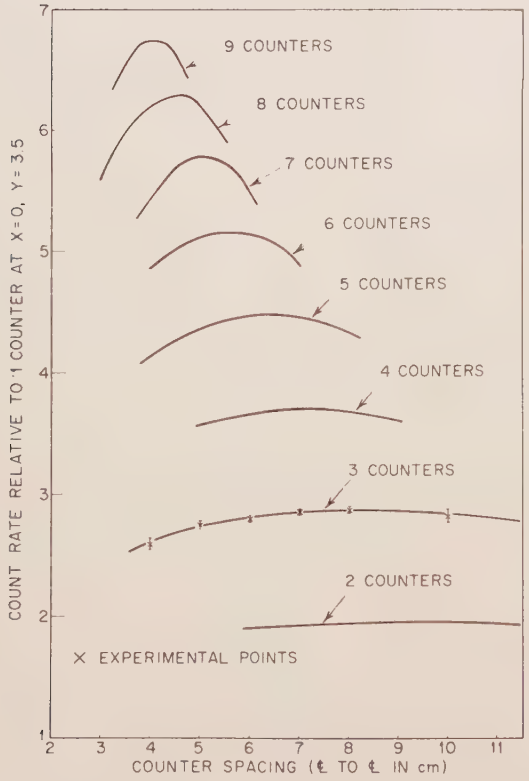

Fig. 6. Calculated relative count rate versus centerline to centerline counter spacing (X_0) for two to nine counters. Experimental points for the three counter case are shown.

The calculated relative counts rate as a function of X_0 for assemblies of two through nine counters along the line Y equal to 3.5 cm is shown in fig. 6. Where significant, interactions between each counter and nonadjacent counters were used in these calculations; curves of fig. 3 were assumed to be accurate enough for this purpose. A few calculations for the case of unequal spacings between counters were attempted, but resulted in little change in the sensitivity for this choice of BF_3 counter and moderator dimensions.

The experimental variation in relative count rate of a three counter array is also indicated in fig. 6. The experimental data agree statistically within $\pm$ 1 % of the corresponding points on the calculated curve.

Several arrangements, other than putting all of the counters along the 3.5 cm line, have been tried and found to be less efficient for this choice of BF_3 counter and moderator dimensions.

6. Discussion

The method described for determining the optimum location of BF_3 counters is also applicable to cases where the distance between source and detector is greater than the detector length and width, such that the incident neutron flux is uniform over the detector face. The experimental data required are the interaction between counters (fig. 3) and the relative count rate profiles (figs. 4 and 5) along the axis of symmetry of the moderator and along a line perpendicular to it. Furthermore, maximum relative count rates can be calculated for different numbers of counters.

Detectors which have been optimized for the partially moderated Po-Be spectrum show a high sensitivity to thermal neutrons.

Acknowledgements

The authors are grateful to Dr. C. V. Strain and Mr. D. C. Cook for their encouragement and guidance during the course of this work.

NUCLEAR INSTRUMENTS AND METHODS 13 (1961) 313–316; NORTH-HOLLAND PUBLISHING CO.

AN IMPROVED Li^6-LOADED GLASS SCINTILLATOR FOR NEUTRON DETECTION

F. W. K. FIRK† and G. G. SLAUGHTER

Oak Ridge National Laboratory, Oak Ridge, Tennessee

and

R. J. GINTHER

Naval Research Laboratory, Washington, D.C.

Received 30 July 1961

A cerium activated, Li^6-loaded, glass scintillator of improved scintillation efficiency and Li^6 content has been developed and used for detecting neutrons with energies from thermal to 80 keV by time-of-flight techniques. The following properties of a glass scintillator ($\approx 1.5''$ thick) with 0.045×10^{24} Li^6 atoms/cm^2 were determined:

(i) an efficiency of 20% for detecting neutrons of 1 keV energy

(ii) a negligible background due to γ-rays of energy < 1.3 MeV

(iii) a resolution of 25% for the $Li^6(n, \alpha)T$ peak

(iv) a pulse with rise time ≈ 4 nanosec and a decay ≈ 100 nanosec into an impedance of 100 ohms.

(v) a time resolution < 2 nanosec when using a "fast-slow" coincidence system and annihilation quanta from Na^{22}.

These properties have been exploited in measuring the neutron energy spectrum from the reaction $Li^7(p, n)Be^7$ using the ORNL pulsed Van de Graaff and the associated nanosec time-of-flight spectrometer. For a proton energy 15 keV above the reaction threshold the neutron energy spectrum extended from 5 keV to 80 keV. Neutron transmission measurements up to several keV also demonstrate the use of the scintillator with a fast chopper neutron spectrometer. Lithium and boron loaded glass scintillators have been compared and it is concluded that lithium glass is, in general, the more suitable for neutron detection.

1. Introduction

The most successful neutron detectors currently available for time-of-flight measurements in the energy range 1 eV to 100 keV are the NaI-B^{10} scintillation detector of Rae and Bowey[1]), and the boron loaded liquid scintillator of Muehlhause and Thomas[2]). The LiI(Eu) neutron detector developed by Schenck[3]) has not found application in the detection of resonance energy neutrons because the competing capture in the iodine introduces detailed structure in the energy response. From considerations of the light output and decay time of LiI(Eu) it is inferred that the timing resolution should be about the same as that of the NaI-B^{10} system. The boron loaded liquid of Muehlhause and Thomas has a time resolution ≈ 0.5 μsec due to the thermalization time of neutrons in the liquid and is not suitable, therefore, for use with the short bursts of neutrons now produced by pulsed cyclotrons, pulsed linear accelerators and, in particular, pulsed Van de Graaff machines. The NaI-B^{10} detector has been developed by Good and Neiler[4]) for use with the Oak Ridge 3 MeV pulsed Van de Graaff and a time resolution of 5–6 nanosec. (1 nanosec $= 10^{-9}$ sec), using a "fast-slow" coincidence system, has been achieved. Considerable effort has been made to improve the above resolution but it appears that the intrinsic timing resolution of the detector has been reached. The need for a neutron detector of high efficiency combined with a time resolution < 5 nsec is therefore obvious.

Recently, several papers have described scintillating glasses suitable for use as both γ-ray and neutron detectors[5,6]). The work of Voitovetskii, Tolmacheva and Arsaev[7]) and of Bollinger, Thomas

† Visiting ORNL from AERE, Harwell, England.

[1]) E. R. Rae and E. M. Bowey, Proc. Soc. A **66** (1953) 1073.

[2]) C. O. Muehlhause and G. E. Thomas, Nucleonics **11**, No. 1 (1953) 44.

[3]) James Schenck, Nature **171** (1953) 518.

[4]) Good, Neiler and Gibbons, Phys. Rev. **109** (1958) 926.

[5]) R. J. Ginther and J. H. Schulman, I.R.E. Trans. NS-5, No. 3 (1958) 92.

[6]) R. J. Ginther, I.R.E. Trans. NS-7, No. 2–3 (1960) 28.

[7]) Voitovetskii, Tolmacheva and Arsaev, Atomnaya En. **6** (1959) 321; also (1959) 472.

and Ginther[8]) showed that cerium activated glasses loaded with either lithium or boron were suitable for detecting neutrons. However, the relatively low pulse height of the glass of Voitovetskii *et al.*[7]) and the use of natural boron in the glass of Bollinger *et al.*[8]) limited the general use of these glass scintillators for neutron detection. This paper reports measurements of neutron energies up to ~ 100 keV (by time-of-flight techniques) using a Li^6-loaded glass scintillator. The scintillation efficiency of the present glass (12% of NaI(Tl) for 1 MeV γ-rays) has been increased by a factor of 4 over that reported by Voitovetskii *et al.*[7]).

2. Composition and Manufacture of a Li^6-loaded Glass Scintillator

The glass scintillator used had the following composition:

	$Li^6O_{\frac{1}{2}}$	$AlO_{\frac{3}{2}}$	$CeO_{\frac{3}{2}}$	SiO_2
Molar ratio	0.355	0.075	0.02	0.55
% by weight	11.03	8.48	7.28	73.12

This has the optical properties of glass No. 6 given by Ginther in ref.[6]). For the present purpose, Li_2CO_3 prepared at ORNL containing ≅95% of its Li content as Li^6 was used as a raw material. Eight small batches each consisting of about 14.5 g of glass were first melted in a reducing atmosphere in 50 ml platinum crucibles at 1500°C using the crucible arrangement described in ref.[5]). These small samples were allowed to cool in their crucibles, then removed and remelted together in a $1\frac{3}{4}''$ diameter $\times$ $2\frac{1}{2}''$ tall platinum cylinder made from 0.002″ foil. The platinum cylinder was supported by a cylindrical alumina crucible of about the same size resting on a bed of powdered graphite inside a larger alumina cylinder about $3\frac{1}{4}''$ OD and $6\frac{1}{4}''$ high. This latter crucible was capped with platinum foil. The crucible arrangement is simply a larger version of the one used for melting the eight individual pieces.

While the pulse height with gamma ray excitation of the small pieces was 12% of that of a NaI(Tl) crystal, it was found that in the large sample this pulse was reduced to 10%, presumably due to self absorption of the emitted light.

3. Neutron Detection Properties of the Scintillator

3.1. Pulse Height Spectrum from the Reaction $Li^6(n, \alpha)T + 4.8$ MeV

The pulse height spectrum when irradiated with resonance energy neutrons from the Oak Ridge 30 MW reactor and associated fast chopper neutron spectrometer[9]) is shown in fig. 1. The well defined peak with full width at half maximum of 25% is clearly above the noise level of the electronic system and is readily selected using a single channel pulse height analyzer. For smaller pieces of glass, 1″ diameter $\times$ $\frac{1}{4}''$ thick, a resolution of 18% was obtained.

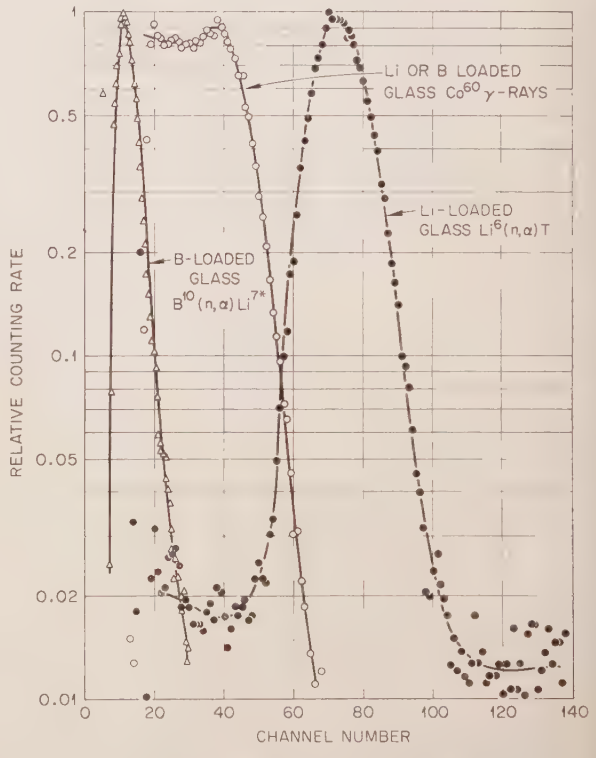

Fig. 1. Typical pulse height spectra for lithium-loaded and boron-loaded glass scintillators. The mass absorption coefficient of the lithium loaded glass for Co^{60} gamma rays, as measured by total integrated counts, agreed qualitatively with an approximate calculated value of 0.055 cm^2/g.

The equivalent electron energy of the (n, α) peak shown in fig. 1 is approximately 1.6 MeV. This was

[8]) Bollinger, Thomas and Ginther, Rev. Sci. Inst. **30** (1959)L 1135.

[9]) Block, Slaughter and Harvey, Nucl. Sci. and Eng., **8** (1960) 112.

determined from the maximum Compton electron energies obtained using Co^{60} and ThC″ γ-ray sources.

3.2. γ-RAY SENSITIVITY

Ginther and Schulman[5]) have shown that cerium activated glasses of the type described here are useful detectors of γ-rays. This is a disadvantage when used for neutron detection. However, the γ-ray sensitivity of the present glass is such that γ-rays of energy < 1.3 MeV contribute negligibly to the (n, α) peak. This is demonstrated in the curve in fig. 1 where the pulse height spectrum from Co^{60} γ-rays (1.17 and 1.33 MeV) is compared with the neutron induced spectrum.

3.3. TIME CHARACTERISTICS OF THE SCINTILLATION PULSE

An important feature of a scintillator used with time-of-flight spectrometers is the decay time of the light pulse. This has been measured using a Tektronix oscilloscope Type 585 which has a rise time of ≈ 3 nsec. The observed voltage pulse obtained from the anode of a Philips 56 AVP phototube with a load resistor of 100 Ω had a rise time (10–90%) of ≈ 5 nsec and decay time (100–50%) of 100 nsec. The decay time is approximately 40% of the corresponding quantity for a NaI(Tl) crystal.

3.4. NEUTRON DETECTION EFFICIENCY

The large neutron cross section of Li^6 at thermal energies (≈ 900 b) ensures that the Li^6 glass will have a high neutron efficiency at low energies. However, for neutron energies greater than 1 keV it has been possible to load the glass with sufficient Li^6 nuclei to obtain an efficiency of 20% at 1 keV using a 1.5″ thick piece of glass. The efficiency of the glass has a $1/v$ dependence for energies up to ~ 30 keV. The cerium content introduces no resonance structure in the neutron response.

4. Applications to Neutron Time-of-Flight Experiments

4.1. NANOSECOND TIME-OF-FLIGHT MEASUREMENTS IN THE NEUTRON ENERGY RANGE 5 TO 80 keV

The ORNL 3 MeV pulsed Van de Graaff has been used to produce proton bursts of ≈ 10 nsec duration at a repetition rate of 500 kc/s. The energies of neutrons from the reaction Li^7(p, n)Be^7 for incident protons 15 keV above threshold were detected using nanosecond time-of-flight techniques[4]). Using a flight path of 1.7 m and 1023 timing channels, each of 2.6 nsec duration, a resolution of ≈ 7 nsec per metre was obtained. The contribution to the time resolution from the glass scintillator was < 4 nsec. This figure was obtained in a separate experiment by observing 1.5 to 2 MeV γ-rays from the target of the Van de Graaff machine when using a beam pulsing system which provided a burst duration of < 2 nsec[10]) and timing channels of 0.6 nsec. A reproducible time resolution of < 4 nsec was determined.

The measured neutron energy spectrum from the

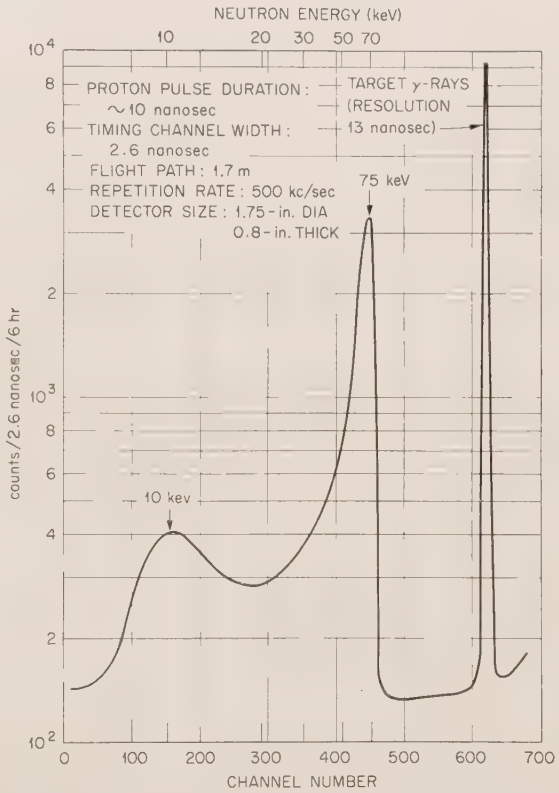

Fig. 2. The observed neutron energy spectrum of Li^7(p, n)Be^7 measured with a Li^6-loaded glass scintillator.

Li^7(p, n)Be^7 reaction is shown in fig. 2. The full width at half maximum of the peak obtained from the target γ-rays shows that the total resolution is

[10]) W. M. Good and R. F. King (to be published).

$\sim$ 13 nsec. The detection efficiency at 20 keV (of a glass with 0.01×10^{24} Li^6 atoms/cm^2 is approximately the same as that of a B^{10}-NaI(Tl) detector using a densely packed slab of $B^{10}{}_4C$ of 1 cm thickness viewed by a 4″ diameter by 2″ long NaI crystal with a 30% solid angle.

4.2. NEUTRON TRANSMISSION MEASUREMENTS USING A FAST-CHOPPER

The ORNL fast chopper and associated time-of-flight spectrometer[9]) has been used with a Li^6 glass neutron detector (1.75″ diam. $\times$ 0.8″ thick) to measure total neutron cross sections up to an energy of 5 keV. The time resolution of the detector was negligible compared with the duration of the narrowest burst obtainable from the chopper ($\approx$ 0.8 μsec). Due to the use of the MkI rotor[9]) which has 15 slits each 0.030″ wide and provides 8 bursts per revolution, a continuous γ-ray background accompanied the neutrons, thereby representing a severe test of the neutron: γ-ray sensitivity of the detector. Flight paths of 12, 45 and 180 m length were used for these measurements. A typical neutron transmission curve for tungsten (0.1″ thick) obtained at the 45 m detector station is shown in fig. 3. The signal: background ratio was approximately 10:1 for 1 keV neutrons. The efficiency per unit area of the Li^6 glass detector for 1 keV neutrons is $\approx$ 10 times that of the $B^{10}F_3$ counters currently in use at the 180 m detector station. The use of a large area Li^6 glass scintillator would therefore appear to be very promising in this case.

5. Conclusions

These measurements show that Li^6-loaded glass scintillators are comparable in efficiency for detecting neutrons in the energy range 1 eV to 100 keV with any fast detector now in use. The Li^6 glass offers the following advantages:

(i) excellent time resolution
(ii) good neutron: γ-ray sensitivity
(iii) ease of manufacture
(iv) simple associated electronics.

Apart from a factor of $4\frac{1}{2}$ in favor of the $B^{10}(n, \alpha)$ cross section compared with the $Li^6(n, \alpha)$ cross section, boron loaded glasses[8]) are not so well suited for time-of-flight neutron detection, particularly where nanosecond time resolution is required. This is due to the poorer pulse height and resolution (50%) obtainable for a boron loaded glass[8]). From a linear extrapolation of measurements using a

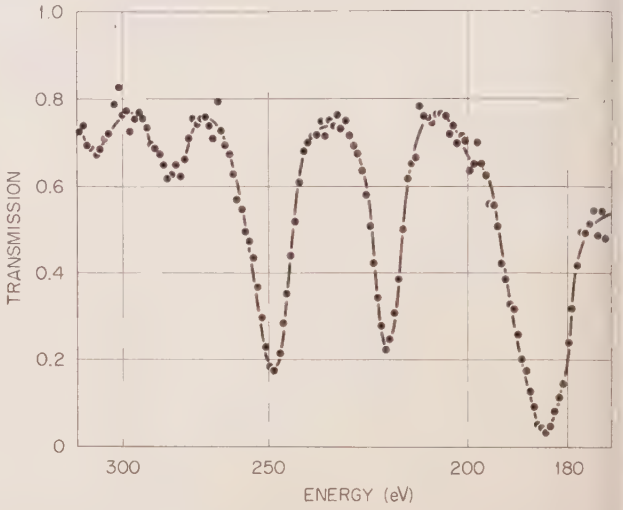

Fig. 3. The observed neutron transmission of tungsten from 180 to 320 eV.

5.1 MeV Pu^{239} α source it is inferred that the 2.1 MeV α from the $Li^6(n, \alpha)T$ reaction contributes an equivalent electron energy of 400 keV in the lithium glass. The remaining 1.2 MeV equivalent electron energy of the reaction can be attributed to the 2.7 MeV triton. Although this large difference in response to α particles and tritons is atypical of crystalline inorganic scintillators, the glass does not have their regular structure and long range order. It is not so surprising, therefore, that the particles in the $B^{10}(n, \alpha)Li^{7*} + 2.3$ MeV reaction, with their high specific ionization, contribute a total equivalent electron energy in the boron glass of only 250 keV. The relatively small pulse height from the $B^{10}(n, \alpha)$ peak means that the boron loaded glasses are sensitive to low energy (< 0.5 MeV) γ-rays, which is an undesirable feature in almost all experiments involving neutron detection

Acknowledgements

One of us (F.W.K.F.) is indebted to Drs. W. M. Good and J. A. Harvey for the excellent facilities made available at ORNL for this work. It is a pleasure to acknowledge the able assistance of Mr. Richard P. Cumby.

NUCLEAR INSTRUMENTS AND METHODS 13 (1961) 317–320; NORTH-HOLLAND PUBLISHING CO.

THE ACHIEVEMENT OF VERY HIGH PUMPING SPEEDS IN THE ULTRA-HIGH VACUUM REGION

D. R. SWEETMAN

A.W.R.E., Aldermaston, Berks.

Received 24 July 1961

The gettering action for hydrogen of a freshly evaporated film of titanium has been investigated at surface temperatures between 25°C and — 196°C. At 25°C sticking probabilities of 13 per cent are observed. At — 196°C the sticking probability is greatly increased and is estimated to be greater than 50%. It remains high until a mono layer has formed on the surface.

1. Introduction

Research on controlled thermonuclear reactions has stimulated interest in the maintenance of an ultra high vacuum in the presence of large leaks of hydrogen and other gases. The high pumping speeds necessary require the use of either diffusion pumps, which become prohibitatively large and expensive for speeds above 20000 l/sec or the use of gettering. In many applications the high pumping speeds are required for only a few minutes or even seconds. In these cases a gettering technique has advantages.

The capture probability of a gas molecule incident on a surface is dependent on the detailed structure of the surface and the time of contact. The surface structure is known to depend on the temperature of the surface during evaporation, and the time of contact should depend on the surface temperature during the absorption. Most of the experiments with getter surfaces have been carried out at room temperature and above where the sticking probability is found to decrease monotonically with temperature[1,2]).

We report here the results of some measurements in which we have observed very high sticking probabilities for hydrogen with a large titanium getter surface cooled to liquid nitrogen temperature.

2. Apparatus

Fig. 1 shows the apparatus used for this work. The apparatus was designed for use in a thermonuclear experiment involving the injection of neutral particles into an ultra-high vacuum and so was not ideal for the measurement of sticking probabilities.

Titanium was evaporated from high purity wire

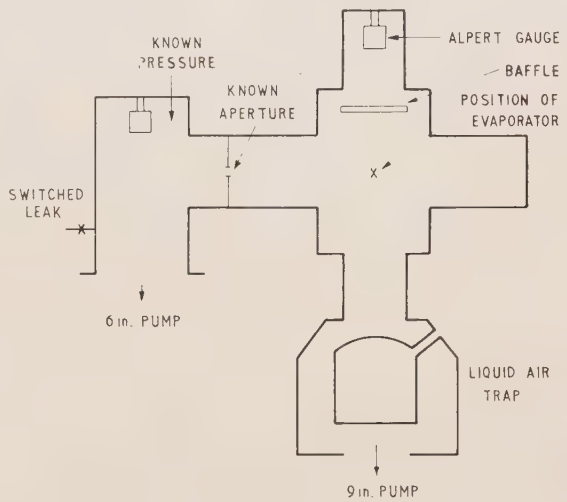

Fig. 1. Diagram of the apparatus.

wrapped around a tungsten filament mounted centrally in the stainless steel vessel of 10^4 cm^3 volume and 5000 cm^2 surface area which was continously pumped by a 9″ diffusion pump through a liquid nitrogen trap. Hydrogen could be let into the vessel at a known rate by raising the pressure in a neighbouring vessel by a known amount, the two vessels being connected by a circular aperture of calculable conductance. If so desired, the hydrogen

[1]) G. Ehrlich, J. Phys. Chem. **60** (1956) 1388.
[2]) S. Wexler, Rev. Mod. Phys. **30** (1958) 402.

flow could be switched on for only a few seconds, sufficient to observe the pressure rise. The pressure in the main vessel was measured with an Alpert ultra-high vacuum gauge mounted in a side limb shielded from the titanium source by a baffle.

The main vacuum vessel could be allowed to remain at room temperature or, alternatively, titanium was outgassed by dissipating about 150 W in the tungsten filament for about 30 sec. After the pressure had fallen to its previous value the titanium was evaporated at about 300 W for several seconds. The filament supply was then switched off and the pressure allowed to settle down to its equilibrium value, which was about 10^{-9} Torr. The

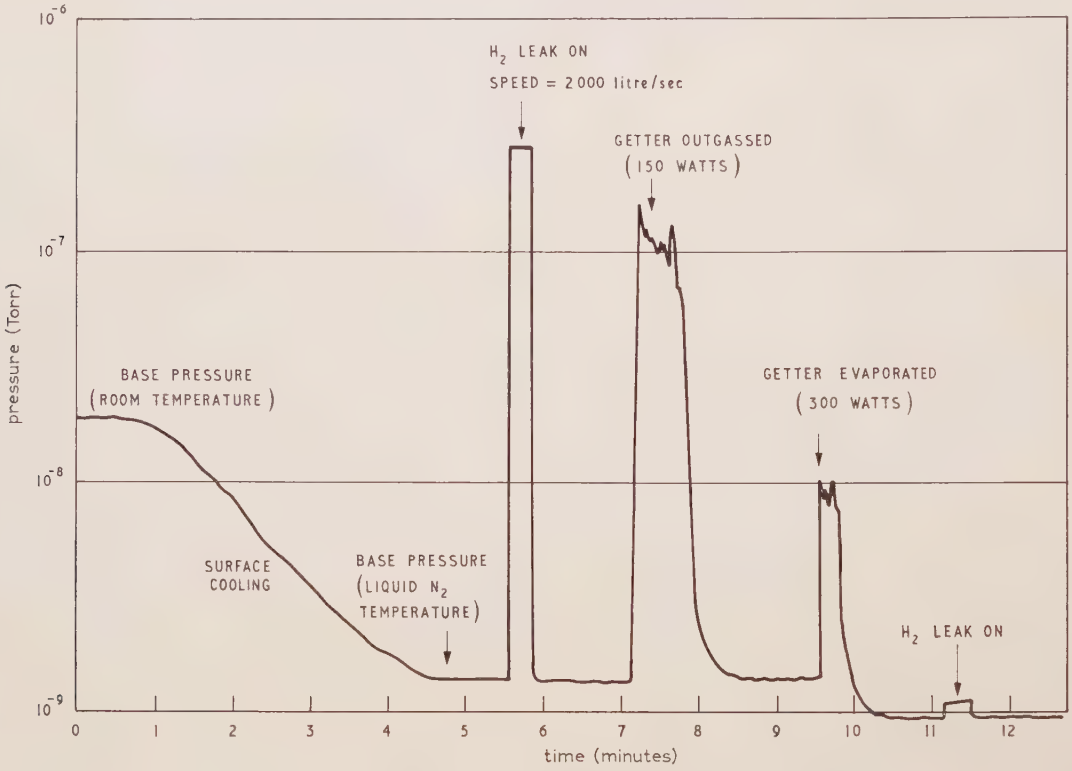

Fig. 2. Pressure variation with time for typical run.

liquid nitrogen could be passed through the cooling jacket. The temperature of the wall surface was measured with a copper-constantan thermocouple.

3. Experimental Results and Discussion

The base pressure in the apparatus at room temperature was about 2×10^{-8} Torr. Reduction of the wall temperature to $-196°$ reduced the pressure to about 2×10^{-9} Torr. In a typical experiment the pumping speed of the diffusion pump was first measured by letting in hydrogen at about 1 litre micron/second. The pressure rose to about 5×10^{-7} Torr indicating a pumping speed of 2000 l/sec, in agreement with the manufacturer's quoted value. After switching off the hydrogen leak the pumping speed was then measured by noting the pressure rise when the hydrogen leak was switched on. This sequence of events is best illustrated by the resulting plot of pressure against time, as indicated on a pen recorder, shown in fig. 2.

When the titanium was evaporated at room temperature the pumping speed was increased from the 2000 l/sec of the diffusion pump to about 30000 l/sec. The approximate area over which the titanium was evaporated was 5000 cm^2. The specific pumping speed was therefore 6 l/sec cm^2 compared with 44 l/sec cm^2 for a completely absorbing surface: a sticking probability of 13%.

Reduction of the wall temperature to $-196°$C and subsequent evaporation of the getter resulted

in a marked increase in the pumping speed over the room temperature values. Apparent speeds of several million l/sec were obtained. In a typical experiment when a 1 litre micron/sec leak was switched on the pressure rose from 1.0 to 1.2 $\times$ 10^{-9} Torr.

Under these conditions, however, the usual method of calculating pumping speed becomes meaningless; with such high sticking probabilities it is necessary to take into account the number of wall reflections that a particle makes in travelling from the input aperture to the ion gauge limb. Although the geometry of the apparatus is far from ideal for such calculations, it is estimated that sticking probabilities in excess of 50% are required to explain the observed results.

In an attempt to discover the mechanism for the dramatic change of sticking probability with temperature, experiments were performed in which the getter was evaporated at room temperature and the apparatus subsequently cooled, the pumping speed being determined with the pulsed hydrogen source at intervals during the cooling cycle. Experiments were also performed in which the getter was evaporated with the walls at liquid nitrogen temperature and the wall temperature subsequently raised. The results of two such runs are shown in fig. 3. There is shown the "apparent speed": that obtained directly from dividing the leak rate by the pressure rise. Such "speeds" have no absolute meaning except for the geometry in question but serve to illustrate both the profound change with temperature and also that the temperature of evaporation is important. Experiments in which the temperature was held constant over a period of 30 min or more, much greater than that required for the previous runs, showed no change of speed from beginning to end.

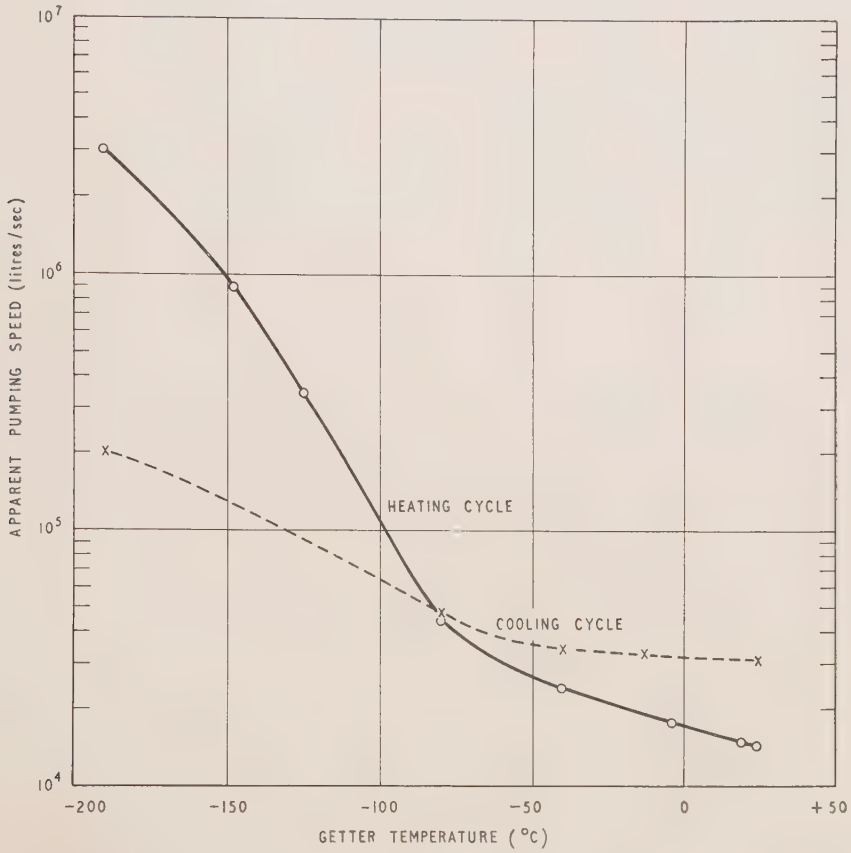

Fig. 3. Leak rate divided by pressure change as a function of temperature. Note that differential pumping effects are not taken into account in this plot.

Poisoning of the getter surface is therefore not considered to be important during these experiments.

The change in sticking probabilities with temperature may be due to a) a change of form of the titanium layer with the temperature of deposition and subsequent processing, or b) a change of the inherent sticking probability with temperature. The results would indicate that both of these processes contribute.

It is perhaps significant that during all the heating and cooling runs, an emission of gas occurred at temperatures between -120 and -150°C. A crystaline transition in this temperature region could account in part for the change of speed.

In experiments in which the hydrogen leak was left on for long periods, the sticking probability decayed rapidly with time at liquid nitrogen temperature, the time constant being approximately that for a mono layer of hydrogen atoms to be deposited on the surface. After switching off the hydrogen leak, the surface recovered its high pumping speed over a period of some five minutes. It is not known whether this recovery is due to slow diffusion of titanium into the substrate or due to release of hydrogen which was pumped away by the diffusion pump. Very clean conditions are required to observe this recovery. In experiments where the surface outgassing rate was known to be high, a slow poisoning of the gettering surface was observed. At room temperature the time constant for decay of the pumping speed corresponded to the formation of a hydrogen layer approximately 50 Å thick. It would appear that at this temperature, the diffusion rate into the titanium substrate is comparable with the deposition rate.

Acknowledgements

The author is indebted to Mr. R. E. Bradford and Mr. J. R. Coupland for their help with the experimental runs and Mr. J. R. Bailey for valuable discussions on vacuum technique.

NUCLEAR INSTRUMENTS AND METHODS 13 (1961) 321–329; NORTH-HOLLAND PUBLISHING CO.

A NEW DESIGN OF A MULTIPLE-WIRE SPARK COUNTER AND SOME STUDIES WITH THE SINGLE WIRE-PLATE SPARK COUNTER

GURBAX SINGH and N. K. SAHA

Department of Physics, University of Delhi-6, India

Received 12 July 1961

A new design of multiple-wire spark counter is described which eliminates almost completely the mutual interaction between the individual counter wires. The counter shows a long plateau (3.3 kV–6 kV) for alpha particle detection with practically no slope. The new design results in a considerable improvement in the neutron counting efficiency over the earlier records.

The alpha counting efficiency of a single wire-plate spark counter is studied at various partial pressures of water, methyl alcohol and ethyl alcohol. A marked effect is observed which shows a close relationship with the diffusivity of these vapours in air. The effect of irradiation by strong beta, gamma and ultraviolet rays on the alpha counting behaviour of the counter shows some interesting results.

1. Introduction

Several attractive features possessed by the Rosenblum type of spark counter[1,2]) have made it a very useful instrument for the detection of α-particles. Chief among these are its simplicity of construction and operation, complete absence of background counting for weakly ionising radiation and generation of very large amplitude ($\approx$ 100 V) pulses of short duration[3]) ($\approx 10^{-8}$ sec or less) following the spark breakdowns. Extensive works have been done by various authors[1–12]) on the spark counter. Some of these works aim at elucidating the difficult problems of distribution of potential and electric field and the sparking mechanism in the counter[4]), but others, more numerous, are devoted to the study of the various practical aspects of its counting properties, e.g. its counting rate versus voltage characteristics[5,6,7]), angular dependence of the counting rate[4,7]), counting behaviour of the different wires of a multiple-wire spark counter[8]), effect of the presence of water vapour in the counting space[4,7,8]), practical feasibility of neutron detection by the multiple-wire form of the spark counter[5,8,9]), etc. Some apparent anomalies which existed in the results of the earlier workers have been largely removed by the later works. There is, however, room for further studies, particularly, of the multiple-wire form of the counter, an improvement in the construction and working of which is called for in order to achieve a reasonable efficiency of neutron detection with this simple device.

The construction of a well operated multiple-wire spark counter presented many difficulties to the earlier workers[2,5,8,10]). Use of an array of equidistant parallel wires as an anode in front of a plane cathode produces considerable mutual interaction between the wires, making it difficult to operate all the wires simultaneously. This interaction also reduces the counting efficiency and results in a non-uniform counting response of the different wires of the counter. The interaction was minimised in two

[1]) W. Y. Chang and S. Rosenblum; Phys. Rev. **67** (1945) 222.
[2]) M. P. Savel; Comptes Rend. **234** (1952) 2596.
[3]) S. L. Gupta and N. K. Saha, Nucl. Instr. and Meth. **13** (1961) 258.
[4]) L. Daddi and L. de Franceschi, Rev. Sci. Instr. **30** (1959) 419.
[5]) N. K. Saha and Narendra Nath, Nucleonics **15**, No. 6 (1957) 94.
[6]) R. D. Connor, Proc. Phys. Soc., London B **64** (1951) 30.
[7]) E. Andreschev and B. M. Isaev, Sov. Phys. JETP. **1** (1955) 212.
[8]) S. Kawata, J. Phys. Soc. (Japan) **16** No. 1, (1961) 1.
[9]) M. Nachman, L. Schächter and H. Totia, Proceedings of the Second International Conference on the Peaceful Uses of Atomic Energy **14** (1958) 335.
[10]) R. D. Connor, J. Sci. Instr. **29** (1952) 12.
[11]) G. G. Eichholz, Nucleonics **10**, No. 10 (1952) 46.
[12]) T. Nakaya and K. Imamura, (Private Communication).

different ways. The first method consisted in the adjustment of the relative distances of the wires from the plane cathode[10]). In the second method the wires were stretched in front of a system of parallel rods which constituted the cathode[11]), the wires running close and parallel to the rods and thus making the electric field between the wires and the rods highly localised and consequently reducing the mutual interaction. Both these modifications do not, however, improve the efficiency much. In the former case, wires slightly farther from the cathode have lower efficiency for detection than those nearer to the cathode. This also results in frequent local discharges between the cathode and the nearer wires. In the latter case, the strong localisation of the electric field makes each wire-rod system strongly directional in α-counting and results in a smaller sensitive volume, as shown by Daddi and Franceschi[4]). This is a very great practical limitation when the counter is used for neutron detection or monitoring.

The present work mainly concerns with a new design of the multiple-wire Rosenblum counter in which the above mentioned defects are sought to be completely eliminated. In this design the counter essentially consists of a number of identical, parallel and semi-cylindrical cavities scooped on the cathode surface. The wires which form the anode are stretched along the axes of the cavities which shield the wires from each other (as described in detail later). Each wire-cavity system is found to be less directional in its counting property than the wire-plate or the wire-rod system. Consequently, it is more efficient and presents a greater sensitive volume for alpha detection.

Operating characteristics of a single wire-cavity system and the dependence of its efficiency on the direction of the incident alphas have been studied. Characteristics of a multiple wire-cavity system have also been investigated. The results show that there is practically no loss of counting efficiency of the individual wires when they are all operated together. This indicates the absence of any observable interaction between the wires.

The slow neutron detection has been studied with the newly designed counter. Considerably higher efficiency of detection is believed to have been achieved than it was possible in the earlier works[5,8]).

In addition to the above studies on the multiple-wire counter, the effect of water, methyl and ethyl alcohol vapours on the counting characteristics of the single wire-plate spark counter has been investigated. Some interesting results are obtained which can be interpreted in terms of the diffusivity of these vapours in air.

Effect of weak ionising radiations like beta, gamma and ultraviolet rays on the behaviour of the counter has also been studied and the preliminary findings are presented.

2. General Description

Fig. 1 shows a front view of the newly designed multiple-wire spark counter. It consists of ten smooth semi-cylindrical cavities of 3 mm diameter

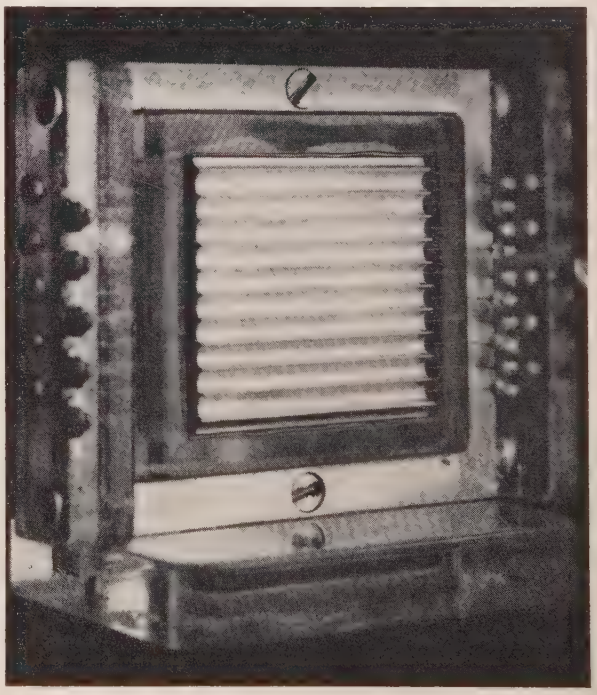

Fig. 1. Photograph (front view) of the newly designed "Multiple Wire-Cavity" spark counter.

each with a 0.1 mm diameter tungsten wire running along the axis of the cavity. The cavities are milled on the surface of a flat brass plate 4 cm $\times$ 4 cm $\times$ 6 mm thickness. The axes of the consecutive cavities are separated by a distance of 3.5 mm and

lie in a plane at a depth of 0.5 mm below the cathode surface. In this way the wires are shielded from each other by the inter-cavity ridges 0.5 mm high

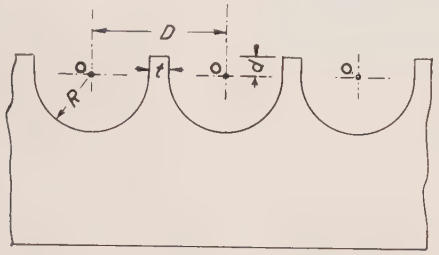

Fig. 2. Illustration of the shielding of the wires from each other by inter-cavity ridges (O is the trace of the wire running along the axis of the semi-cylindrical cavity, R = radius of the cavity, d = depth of the wire-axis below the plate surface, D = separation between the two consecutive wires and t = thickness of the intercavity ridge).

and 0.5 mm wide (fig. 2). The cavity diameter and the ridge width can be reduced further to increase the effective sensitive volume of the counter. Positive voltage up to 6 kV could be applied to the wires individually or collectively. The cathode was grounded through a usual R-C quenching circuit and the pulses were fed to a scaler (fig. 3). For

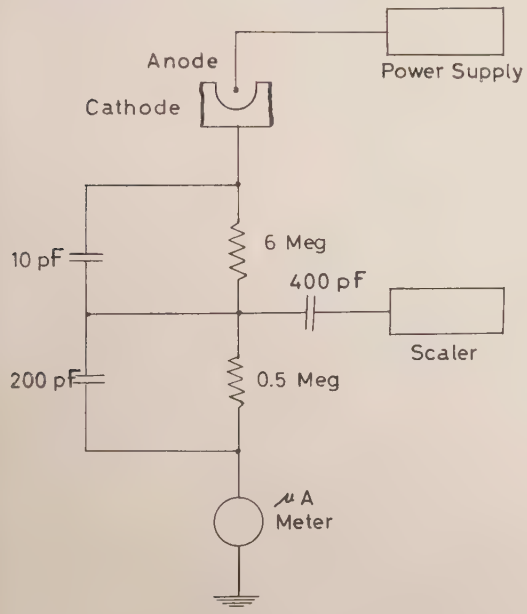

Fig. 3. Operating circuit of the spark counter.

measuring the dependence of counting efficiency on the angle of incidence of the impinging alpha particles, the alpha source was fixed in a holder which was capable of rotating about an axis coinciding with one of the anode wires of the counter. This gives a variation of the angle θ that the direction of the incident α-particles makes with the normal to the cathode plane (see insert of fig. 5). A thin Th-B + C deposit on a platinum foil 1 cm in diameter served as an alpha source. Uncollimated alpha source was used throughout except where stated otherwise.

3. Operating Characteristics

The source was placed facing one of the middle wires of the cavity counter at a distance of 8 cm from it and the counting rate versus voltage characteristics of this particular wire-cavity system were observed. Figs. 4a and 4b show the counting characteristics and the observed variation in the quiescent corona current. The variation in the counting efficiency with the angle of incidence θ (fig. 5) was studied with the wire maintained at an applied voltage of 3.5 kV and by using a collimated beam of alpha particles. For comparison, the angular efficiency was investigated also for a wire-plate counter having the electrodes separated by a distance of 1.5 mm. Figs. 5a and 5b show the relative counting rates for the two cases. In the case of wire-plate system the counting rate falls rapidly after $\theta = 30°$, whereas for the wire-cavity system, it remains practically constant up to $\theta = 60°$ as also observed by Andreschev and Isaev[7]). This proves the superiority of the wire-cavity system as regards its angular efficiency over the wire-plate. The effect is due to the somewhat more symmetrical geometry resulting in a correspondingly more symmetrical sensitive volume of the wire-cavity system than that of the first which has an extended sensitive volume in the direction of the cathode.

Similar investigations for each of the cavities were made and they were found to behave identically within the limits of the experimental accuracy. Next the voltage was applied to the whole array of wires. Figs. 6a and 6b show the counting characteristics and the quiescent corona current variation with applied voltage resulting from this arrangement. A very long plateau (> 2.5 kV) with practically zero slope seems to be an interesting feature. Moreover, as is evident from the figs. 6 and 4, the

number of counts obtained with the multiple wire-cavity counter (having 10 cavities) is very nearly ten times that obtained with a single wire-cavity system. This proves qualitatively independent functioning of each wire as regards its counting behaviour. As expected, the corona current at a observed indicates again the absence of any observable interaction between the wires.

4. Neutron Detection

The wider plateau and the higher alpha counting efficiency of the multiple wire-cavity counter than

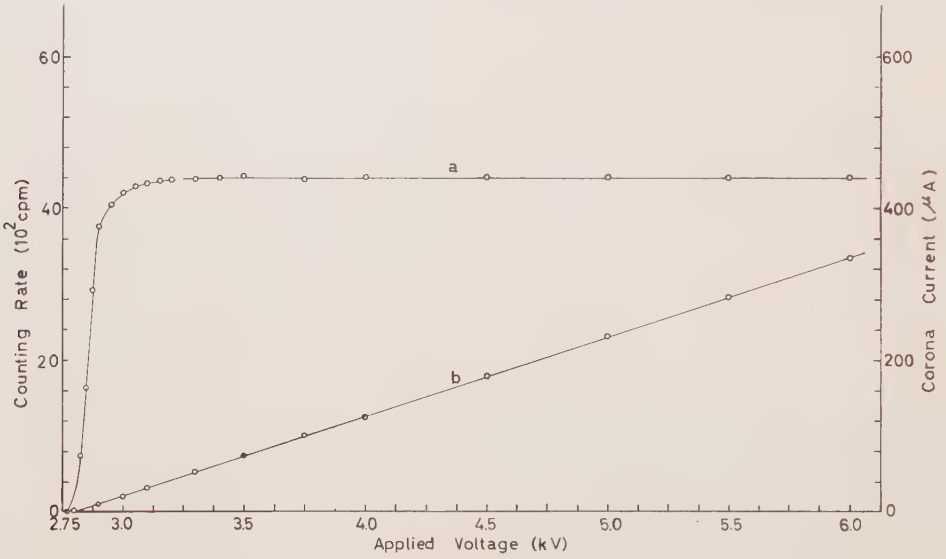

Fig. 4. (a) Counting characteristics and (b) Corona current characteristics of a single wire-cavity spark counter.

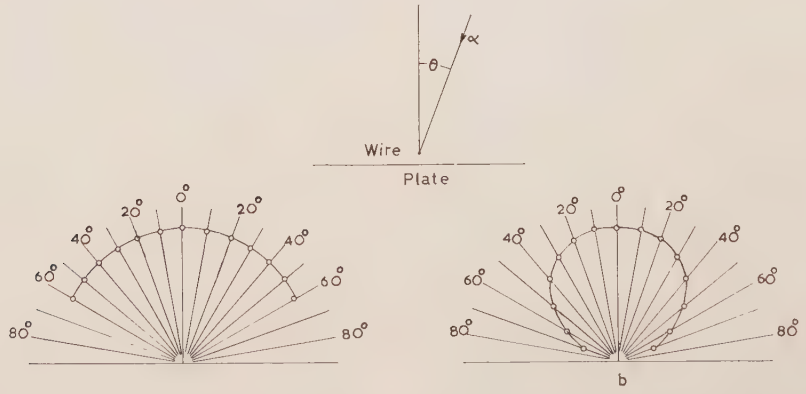

Fig. 5. Counting efficiency vs. angle of incidence (θ) (efficiency at $\theta = 0°$ being taken as unity) (a) for a wire-cavity system, (b) for a wire-plate system. The insert defines the angle θ.

given applied voltage is considerably greater than that for a single wire-cavity system. To test further the uniformity of counting of the wires, when all operating together, the source was collimated by a 4.5 mm diameter and 2.5 cm long hole and displaced perpendicularly across the wires at a constant distance of 4.5 cm from them. Fig. 7 gives a count-displacement curve. The uniform response

those of the conventional multiple-wire systems are very promising features for the detection of fast and slow neutrons. We have tried the new design for the slow neutron detection by making use of the usual $B^{10}(n, \alpha)Li^7$ reaction.

The cathode surface was uniformly coated with natural boron powder mixed with a very little amount of aquadag which served as a sticking and

conducting material. The counter and a 100 mg. Ra-α-Be neutron source, separated by a distance of 6 cm, were placed inside a cubic paraffin box of 11 cm inner side and 10 cm wall thickness all round. The neutron counting rate versus applied voltage was studied and is illustrated in fig. 8a. It gives a distance of 2 mm in front of the wires. A shift of about 100 V was observed in the threshold voltage and is probably due to the proximity of the plate resulting in the distortion of the electric field. Curves 8a′, 8b′ and 8c′ give the corresponding corona currents. Next the aluminium and the glass

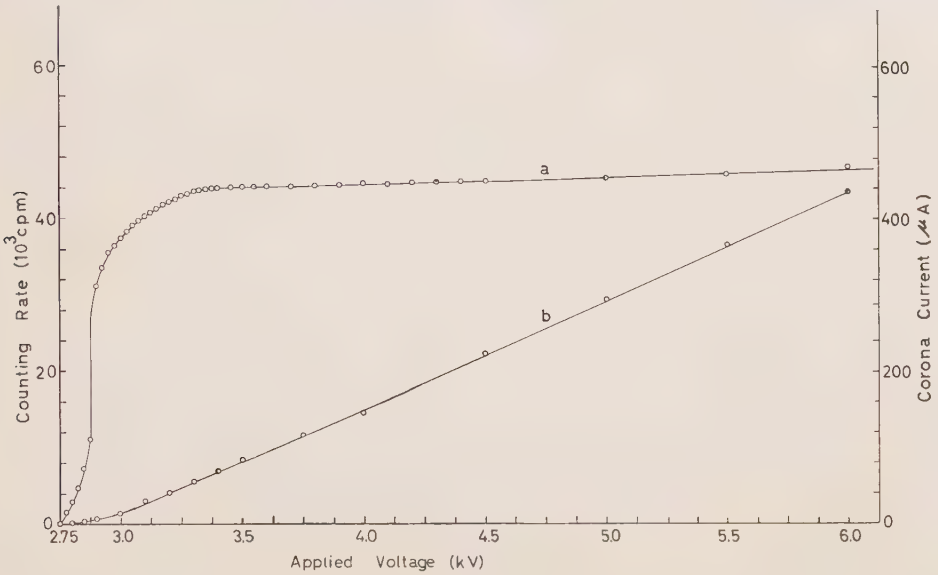

Fig. 6. (a) Counting characteristics and (b) Corona current characteristics for the multiple wire-cavity spark counter.

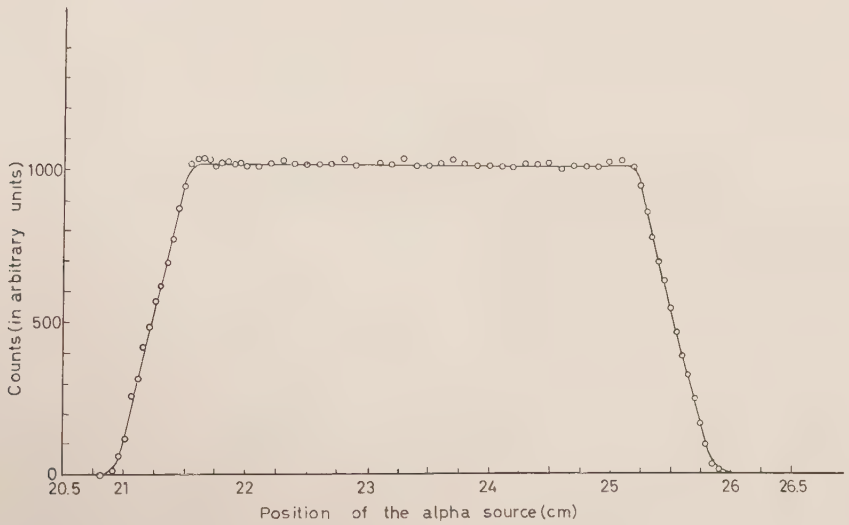

Fig. 7. Counting rate vs position of the α-source when the source is moved parallel to itself and perpendicular to the wire length.

very good plateau with an average counting rate of 310 cpm. Curves 8b and 8c (which coincide with 8a at higher voltages) are the neutron counting characteristics obtained when a thin bare glass plate and an aluminium plate, respectively, were placed at a plates were coated with boron and placed back in position. Figs. 8d (glass) and 8e (aluminium) show the new counting characteristics obtained. The observed rise of about 70 counts/min in the counting rate in the plateau region is due to the

contribution of alphas coming from the coating on the plate. Curves 9a, 9b and 9c show further the neutron counting characteristics observed when the boron coated aluminium plate was placed at three different distances from the wires, namely 1.5 mm, 2 mm and 3 mm respectively. While the neutron counting rate in the plateau region was about 380 cpm as compared to 7 cpm reported in our earlier work (Saha and Nath[5])) under the same geometrical arrangements. Kawata[8]) observed 70 counts by covering a conventional multiple-wire spark counter, having a boron coated plate in front

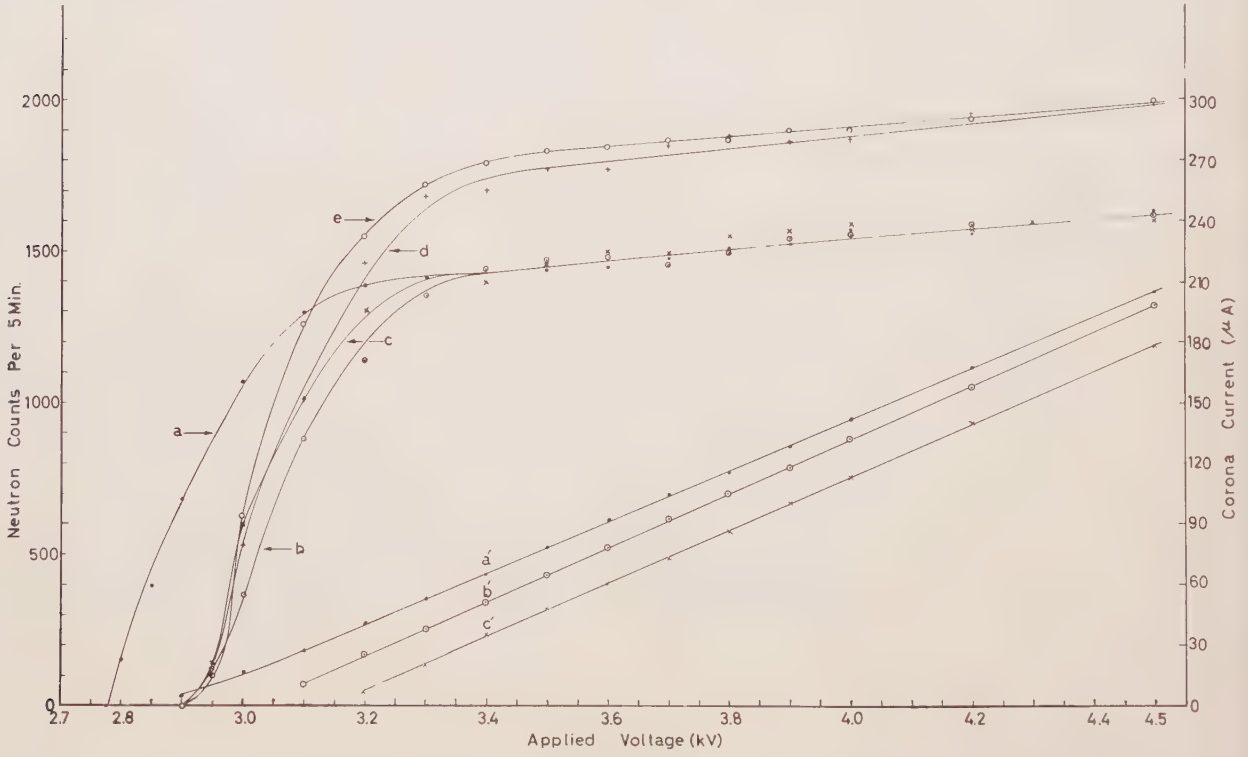

Fig. 8. Neutron counting rate vs applied voltage: (a) with the multiple wire-cavity counter having boron coated cathode, (b) with bare glass plate, (c) with bare aluminium plate in front of the counter, (d) with boron coated glass plate and (e) with boron coated aluminium plate in front of the counter. a′, b′ and′ c give the corona current characteristics corresponding to a, b, and c respectively.

first two curves are practically identical, the third shows a substantially lower counting rate. This is probably due to the low energy of the alpha particles and their straggling in the coating layers on the plate. This results in the reduction of alphas reaching the sensitive region. Much shorter distances gave the trouble of spontaneous discharges. Optimum distance for the maximum available counting rate seems to lie between 1.5 mm and 2 mm. Practically no background counts were observed in the presence or absence of a strong gamma ray source when the neutron source had been removed.

Under the optimum conditions the average of it at 1.5 mm, with paraffin 4 cm thick and placing a 50 mc Ra-α-Be neutron source on the upper side of the paraffin. Our arrangement seems to be somewhat more effective in neutron detection than that used by Kawata. It is hoped that the neutron counting efficiency can be further improved by using enriched boron-10 coating instead of natural boron. Operating the counter in an atmosphere of BF_3 enriched in B-10 is also likely to improve the efficiency.

5. Effect of Vapours

Some of the earlier workers have reported a very small effect of temperature on the counting efficien-

cy of the spark counter (Saha and Nath[5]), Kawata[8])). A marked dependence of the counting efficiency on the water vapour content in air has been observed by Andreschev and Isaev[7]), Kawata[8]) and Daddi and Franceschi[4]). The first two authors[7,8]) have shown an almost linear increase of temperature, 24°C). The total air pressure in the chamber was always maintained constant at 74.3 cm Hg. Variation in the quiescent corona current and the counting rate was observed at various partial pressures of water, methyl alcohol and ethyl alcohol vapours, in turn. Observations were carried

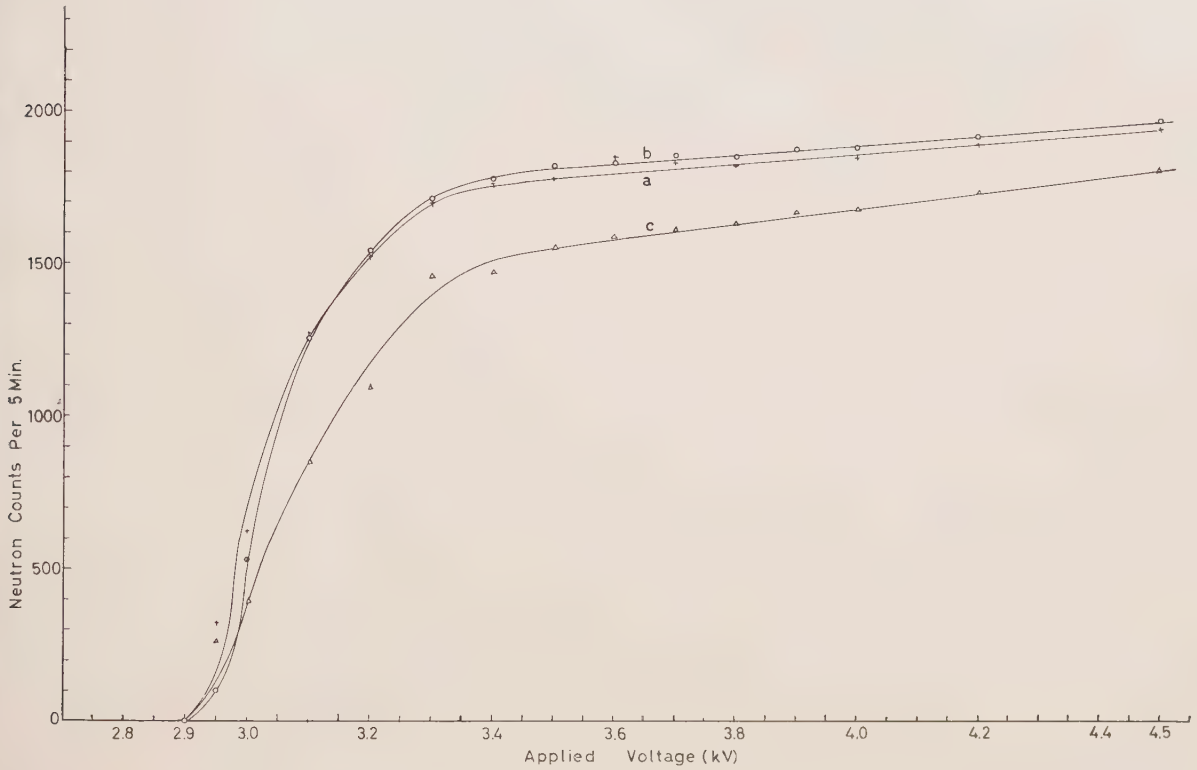

Fig. 9. Neutron counting rate vs applied voltage when the boron coated aluminium plate is placed at (a) 1.5 mm, (b) 2.0 mm and (c) 3.0 mm from the counter wires.

the plateau counting rate with the partial vapour pressure of water. With a view to understand the role of vapour, in general, in influencing the spark breakdown process, we have tried similar investigations with water vapour, as well as with methyl and ethyl alcohol vapours. A highly polished flat stainless steel plate served as the cathode and a single 0.1 mm diameter tungsten wire as the anode, the separation between the two being maintained at 1.3 mm. The alpha source was kept in the end-on position at a fixed distance of 7.5 cm from the counter wire and the two were kept inside a sealed chamber. Provision was made for electrical connections and for introducing any of the vapours into the chamber at a desired pressure (below its saturation vapour pressure at the room out at the room temperature and the minute effect that might be caused by its fluctuations during the period of observation was neglected.

These studies made it clear that at any given applied voltage no appreciable change in the corona current occured within the range of the above variations in the atmospheric condition. But the plateau slope of the counting rate versus applied voltage characteristics showed a striking improvement with the addition of the water vapour. This result is in agreement with the observation of Andreschev and Isaev[7]). No such improvement was, however, observed in the other two cases of alcohol vapours. But the sensitivity of the counter was found to be strongly dependent on the amount of the vapour present in all the three cases. Figs. 10a,

10b and 10c show the observed variation of the plateau counting rate (at 3.5 kV) as a function of the partial vapour pressure of water, methyl alcohol and ethyl alcohol, respectively. It is seen that the plateau counting rate increases linearly with the partial vapour pressure in each of the three cases. given vapour enhances the probability of heavier negative ion formation. The heavier ions are expected to diffuse less and thus remain localised. The localisation may greatly help the spark breakdown and consequently improve the counting efficiency (Andreschev and Isaev[7]). The inverse

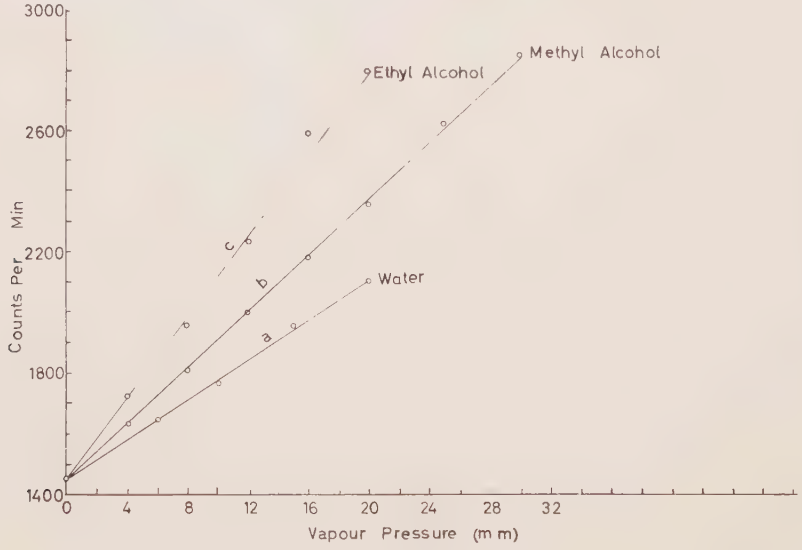

Fig. 10. Plateau counting rate vs partial vapour pressure of (a) Water, (b) Methyl alcohol and (c) Ethyl alcohol.

The slope of the lines increases, in order, from water vapour to methyl to ethyl alcohol vapour. Since the three vapours are in increasing order of molecular weights, it is suspected that the slopes of the lines may be closely related to the diffusivity of these vapours in air. Actually the slopes for the three curves are found to be inversely proportional to the respective diffusion coefficients of the vapours in air as shown in the table below.

The effect seems to depend on the formation of heavy negative ions of vapour molecules in the ionisation space. Increasing the number of vapour molecules by increasing the partial pressure of a relationship of the slopes with the diffusion coefficients of the vapours concerned is therefore qualitatively understood.

Table

	Water	Methyl alcohol	Ethyl alcohol
Ratio of the slopes	1	1.4	2
Diffusion coefficients at 24°C ($cm^2\ sec^{-1}$)	0.240	0.156	0.121
Ratio of the inverse of the diffusion coefficients	1	1.5	2

6. Effect of Radiation

No effect on the α-counting rate was observed when the spark counter was irradiated with beta rays from 1 mc Cs-137 and gamma rays from 50 mc Co-60 or from 100 mg Ra-α-Be neutron source. Exposure to a 1000 watt ultraviolet lamp also left the counting rate unchanged. Contrary to our observation, Nakaya and Imamura[12]) have reported strong suppression of the alpha counting rate under similar radiation exposures. Further we observed on the oscilloscope screen that the corona burst pulses, which appear near the threshold of the corona current, disappeared under the effect of all the above mentioned radiations. This is in close agreement with the observation of Nakaya and Imamura. The significance of the above radiation effects is not yet clearly understood and the effects are worthwhile pursuing further.

7. Conclusion

The idea of the multiple wire-cavity design of the spark counter may perhaps be exploited usefully for the construction of large neutron counters. Such counters may be employed for the study of scattering of neutrons at different target materials. The main advantage of such an arrangement will be that one can directly photograph the sparks caused by neutrons scattered at various angles. Another possible application of the spark counter as such is for monitoring alpha activity in exhaust gases or other contaminations.

Further studies on the spark counter operation in atmospheres containing vapours of different kinds may help in the construction of more efficient counters and may also throw light on the sparking mechanism in the counter.

Acknowledgements

We are thankful to Prof. D. S. Kothari and Prof. R. C. Majumdar for providing facilities and encouragement, to Mr. Narendra Nath for valuable discussions and to Mr. Tirath Ram for technical help.

NUCLEAR INSTRUMENTS AND METHODS 13 (1961) 330–334; NORTH-HOLLAND PUBLISHING CO.

AN AUTOMATIC SAMPLE CHANGER

G. J. SPROKEL

IBM, General Products Division, Development Laboratory, Endicott, N.Y.

Received 24 July 1961

The instrument described permits automatic assay of any number up to 40 radioactive samples. It may be programmed to record the number of the sample being assayed, the accumulated radiation count, and the elapsed time. Complete design data and circuit diagrams are included.

1. Introduction

Most automatic counters which are commercially available are designed and built as complete units, and are not easily interchangeable with equipment from other manufacturers: Our sample changer can, in principle, be used with any gamma spectrometer which has a print-out device. At present, the changer is operated with RIDL† count and time scalers. A CMC†† printer is used to provide a printed record.

2. Operation of the Sample Changer

The changer mechanism consists of an "elevator" and a "turntable". The elevator raises a sample-holding tube out of the detector well. The turntable then rotates, brings the next sample tube over the detector well, and the elevator lowers this sample

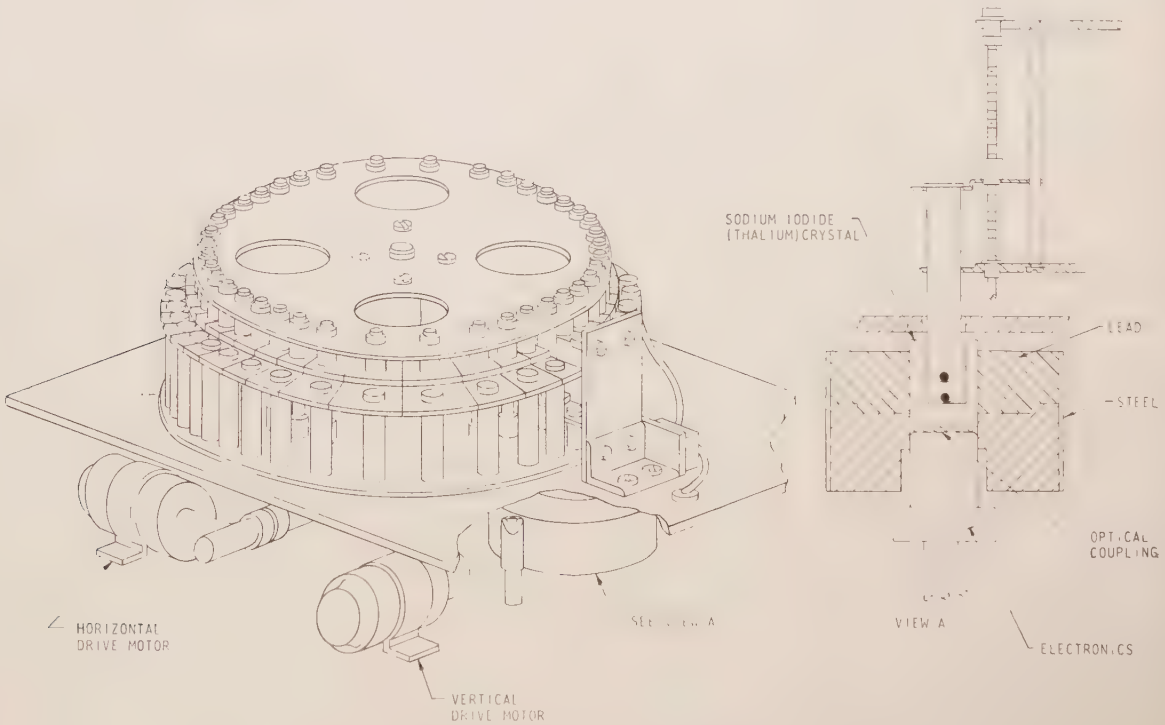

Fig. 1. Sample changer turntable.

† Radiation Instrument Development Laboratory, Chicago, Ill.

†† Computer Measurement Corporation, North Hollywood, Cal.

into the well. During the cycle the counting equipment is kept biased off until the new sample reaches its correct position in the well.

The mechanical layout is apparent from fig. 1. Tubes containing radioactive samples are placed in the tube holders, starting at position 1. A maximum of 40 tubes can be accommodated. The elevator motor (labeled Vertical Driver Motor) drives the elevator screws through idler gears. A reversible motor is used, to both lower and raise the samples. The idler gears are swung out of the way whenever the turntable moves. The turntable motor (labeled Horizontal Drive Motor) drives the table through a 40:1 reduction worm and gear mechanism. Thus, one revolution of the reduction gear shaft brings a new sample over the detector. The upper and lower positions of the elevator are determined by the positions of microswitches 1 and 2 (fig. 2). Microswitch 4, operated from a detent on the turntable motor shaft, determines the position of the sample in relation to the detector. Microswitch 3 is part of the sample identification system (see Section 3).

The switching techniques used are shown in fig. 2. This diagram shows that all motor relays are driven from small relays in the anode circuits of NPNP-controlled switches. The use of these thyratron-like devices has the advantage that a small, short pulse can turn the relay on. The relay will stay on until it is turned off by interrupting the anode circuit.

The changing cycle is initiated by a pulse from the RIDL count scaler. A positive pulse of about 0.6 V at the gate of CS 1 turns on relay 1, when the "repeat-advance" switch is closed. The anode supply is through contact 4 of relay 2 and MS 1, which at this time is closed. Contacts 1 and 2 of relay 1 close elevator motor relay 1 and the elevator moves up. As the elevator starts up, microswitch Ms 2 is released. The normally closed contact of MS 2A connects the + 30 volt anode supply to contact 4 of relay 1, in preparation for the return of the elevator. The normally open contact of MS 2B disconnects the count bus from ground. (This bus is part of the bias circuit of the time and count scalers. These scalers will operate only if the count bus is grounded. Thus, MS 2B prevents the scalers from operating until the switch is tripped by the new sample.)

Continuing now, as the elevator goes up, microswitch MS 1 (located at the top) is tripped. The two sections of this microswitch are adjusted such that MS 1A switches just prior to MS 1B. MS 1A connects the anodes of CS 3 and CS 4 to the + 30 V supply, but this does not turn the devices on. MS 1B disconnects the supply line from relay 1. At the same time CS 3 is turned on. Thus as MS 1B is tripped, the elevator motor stops and the turntable motor starts.

It was necessary to use a dual microswitch to assure that the plate supply of CS 3 (and CS 4) is turned on before the signal arrives at the gate of CS 3.

It was mentioned that there is a detent on the turntable motor shaft. As the detent trips microswitch 4, a pulse at the gate of CS 4 turns this NPNP transistor on. While CS 4 was off, the coupling capacitor between the anodes of CS 4 and CS 5 charged to + 30 V. As CS 4 is turned on, the charge on this capacitor decreases the anode voltage of CS 3 momentarily to about − 23 V. This turns CS 3 off; relay 3 falls out, and the turntable stops.

The detent microswitch also turns on CS 2; thus, as relay 3 switches the AC line back from the turntable motor relay to the elevator motor relays, the elevator will move down. Notice that this is the only possible direction, since contacts 4 of relay 2 interrupt the anode circuit of CS 1. As the elevator lowers the new sample into the detector, microswitch MS 2 is tripped. This interrupts the anode circuit of CS 2; relay 2 drops out; and the elevator stops. At the same time the count bus is grounded again and the counting cycle starts. At the end of the counting cycle CS 1 is turned on by the counting equipment, which starts the changing cycle again.

This process will be repeated until the preselected number of samples is reached. (The sample identification and selection system are discussed in Section 3.) As the preselected number is reached, a pulse appears at the gate of CS 5. Contact 4 of relay 4 now interrupts the detent circuit, the turntable will continue to rotate until the turntable trips microswitch MS 3. MS 3A interrupts the anode circuit of CS 5 and relay 4 falls out. The next time the detent microswitch is tripped, relay 3 will turn off and the normal cycle will be resumed. Microswitch 3B resets the sample identification system.

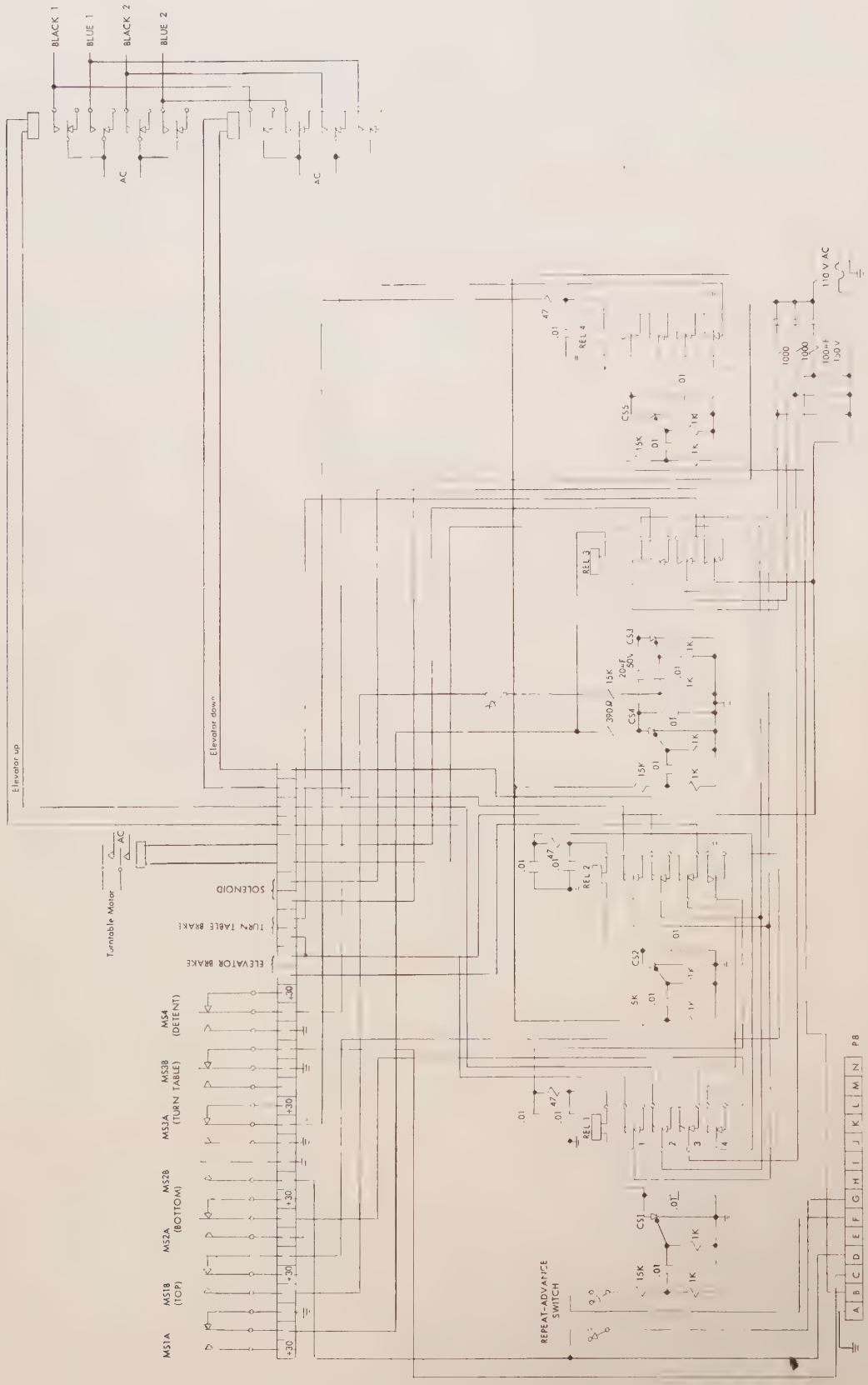

Fig. 2. Sample changer circuitry.

Thus, as the next sample is lowered into the detector, it will register as sample number 1.

To prevent coasting, it was necessary to use brakes on the turntable and elevator motors. The brakes are operated from simple half-wave rectifiers. The turntable motor brake is "on" whenever relay 3 is off. The elevator motor brake is "on" if both relay 1 and relay 2 are off. To prevent overheating the electromechanical brakes, 1000 Ω series resistors are used; however, as the brakes pull in, the capacitors are charged to the full supply voltage (about 150 V). Thus, rapid braking is obtained without overloading the coils.

Controlled switches are very sensitive devices. They may turn on (by internal feed-through) if the anode circuit is suddenly turned on. To prevent this, all CSs are bypassed with 0.01 μf capacitors; CS 1 and CS 2 are further protected by the filter network in series with the relays. Because of the interwiring of CS 1 (through contacts 4 of relay 2) and CS 2 (through contacts 4 of relay 1) it is not possible to turn both relay 1 and relay 2 on at the same time. This would short the AC line through the elevator motor. Notice that the AC line to the motor relays is wired such that only the elevator motor or the turntable motor can be energized, but not both at the same time.

The system CS 3, CS 4, coupling capacitor, and anode load impedances may be regarded as a bistable multivibrator. It is possible to replace CS 4 and the coupling capacitor with a relay.

A detent system was considered for the elevator mechanism without using the limit switches. However, if ever the "turn-off" controlled switch (the equivalent of CS 4) should fail, the elevator would not stop. To avoid this, limiting microswitches could be used, but then these switches might as well be used at all times, which leads to the circuit as described.

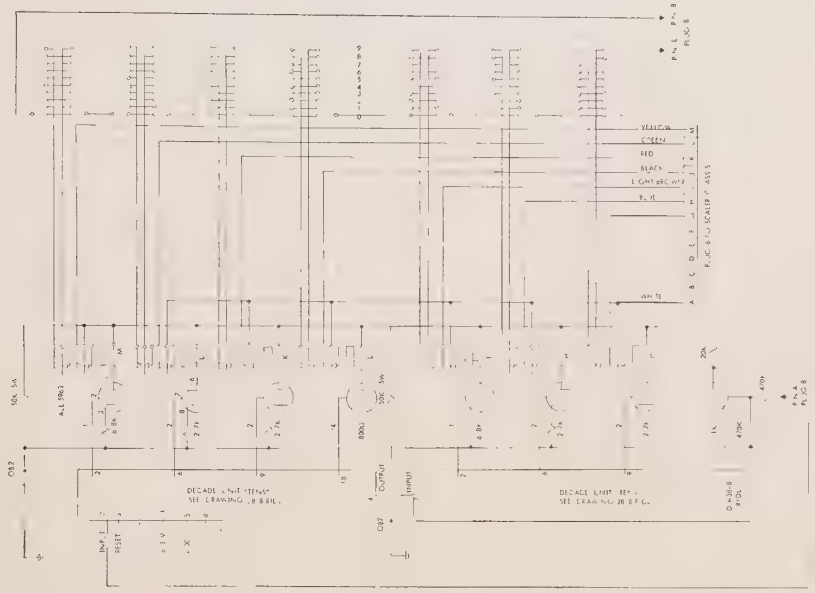

Fig. 3. Sample number identification circuitry.

3. Sample Identification and Selection System

Sample identification on the printed record is is necessary. The CMC printer used with the RIDL time and count scalers accepts a 122′ 4 modified binary code. Positions are available in the printer for an identification system. Thus, the simplest solution is to register the sample numbers in decade units compatible with the printer. These decade units are commercially available.

Fig. 3 shows the identification and selection system. Two decade units are used to register units and tens. The output of the decade units is stored in a buffer stage consisting of two double triodes with a plate relay in each anode circuit.

The positive starting pulse (at the normally closed contact of MS 2B) is inverted in a triode and used to advance the "units" decade by one count. The connection to the pulse inverter is made through the "repeat-advance" switch. If this switch is in the repeat position, the sample number is *not* advanced as a new counting cycle is started.

The triodes in the buffer stage as shown in fig. 3 are normally biased off. They are turned on by the decade units in such manner that the 1, 2, 2′, 4 modified binary code is preserved. Thus the off-on pattern of the relays represents the sample number in a code acceptable to the printer.

The sample number selecting switches are assembled from commercially available parts. The eight decks are wired in the 1, 2, 2′, 4 code; the unused contacts are cross-connected. As an example, suppose the "unit" switch is in position 5 and the "tens" in position 0. As a count of 5 is registered in the buffer stage, relays M, L, and K will close. Then a pulse at the gate of CS 5 (via pin B, plug 8) opens the detent circuit. As explained before, this causes the turntable to rotate until microswitch MS 3 is tripped. The next sample will be lowered in the detector. Since MS 3 also resets the sample decades, this sample will be registered as "1".

NUCLEAR INSTRUMENTS AND METHODS **13** (1961) 335–355; NORTH-HOLLAND PUBLISHING CO.

LES LENTILLES QUADRUPOLAIRES ELECTROSTATIQUES

A. SEPTIER et J. VAN ACKER

Faculté des Sciences de Paris, Labo. d'Electronique, BP9, Fontenay aux Roses, Seine

Reçu le 24 juin 1961

The expression for the potential $\Phi(x, y, z)$ within the useful zone of a quadrupole lens has been established not only when the excitation potentials are symmetrical with respect to earth, but also when these potentials are asymmetrical. New terms arise as a result of this asymmetry, which have a pronounced effect upon both the sense and the size of the aperture aberration.

In the second part we recapitulate the first order optical properties and the results of an experimental study, the object of which is to determine the equivalent length of the lenses and to establish the quantitative behaviour of a doublet.

Next the results of research which has been devoted to measuring and correcting the aperture aberration are given, and several methods of correcting this aberration which are equally valid in stigmatic and in astigmatic operation are suggested.

Finally the so-called "third-order" equations of motion have been established for excitations of both kinds and with the aid of these equations we can calculate the spherical aberration in any system of electrostatic quadrupole lenses. For a doublet this calculation has been performed numerically, and the values obtained agree well with the experimental results.

1. Introduction

Alors que de très nombreux travaux ont été consacrés aux lentilles quadrupolaires magnétiques, on trouve peu de renseignements sur les propriétés optiques des lentilles électrostatiques, en particulier sur les aberrations.

A priori, les lentilles électrostatiques présentent pourtant des avantages certains:

elles sont plus légères,

elles sont insensibles au rapport e/m des particules injectées,

pour des particules non-relativistes, elles peuvent être rendues insensibles aux fluctuations de la tension d'accélération Φ_0 des particules, si on prend soin de les alimenter à partir de la source fournissant cette tension. Dans ce cas, l'alimentation est dite "dissymétrique" car deux électrodes sont reliées à la masse et les deux autres à une tension $2\Phi_1$ proportionnelle à Φ_0 et prélevée par exemple sur un potentiomètre.

elles ne présentent pas de rémanence vers les excitations faibles.

La limite de leur convergence pour des particules d'énergie élevée, est due aux phénomènes de claquage entre les électrodes, et le long des supports isolants: il semble difficile de maintenir des différences de potentiel supérieures à 100 kV entre des surfaces métalliques distantes de 1 à 2 cm, si on recherche une bonne sécurité de fonctionnement.

Dans ces conditions, la tension Φ_1 caractéristique de la lentille est 50 kV et, comme nous le verrons plus loin, on ne pourra atteindre de fortes convergences avec des particules d'énergie supérieure à 10 MeV. Mais pour des particules lourdes ou très lourdes, de quelques MeV, elles pourraient dans certains cas se montrer supérieures aux lentilles magnétiques.

L'étude que nous avons effectuée porte sur les points suivants:

calcul de la fonction potentiel $\Phi(x, y, z)$,

détermination de la longueur efficace des lentilles,

mesure des aberrations d'ouverture des lentilles, en vue de comparer leurs performances avec celles des lentilles magnétiques de caractéristiques identiques.

correction des aberrations par différentes méthodes;

détermination des équations du mouvement dites "au 3ème ordre" permettant le calcul des aberrations

d'ouverture dans les cas d'excitation symétrique ou dissymétrique des électrodes, et détermination du taux d'aberration d'ouverture dans un cas particulier.

2. Le Potentiel dans les lentilles

2.1. CARACTERISTIQUES GEOMETRIQUES DES LENTILLES UTILISEES

Les électrodes sont identiques à celles des lentilles magnétiques étudiées précédemment[1]): rayon de cercle de gorge $a = 4$ cm, électrodes de section circulaire de rayon $R = 1.15\ a = 4.6$ cm, longueur des électrodes $l = 15$ cm (fig. 1a).

Les quatres électrodes sont assemblées, grâce à des isolateurs de plexiglas, sur des anneaux de duralumin. Elles sont réunies deux à deux ainsi qu'aux entrées de tension par des câbles isolés au polythène, qui traversent la paroi cylindrique de l'enceinte à vide. Le diamètre extérieur des lentilles ainsi construites

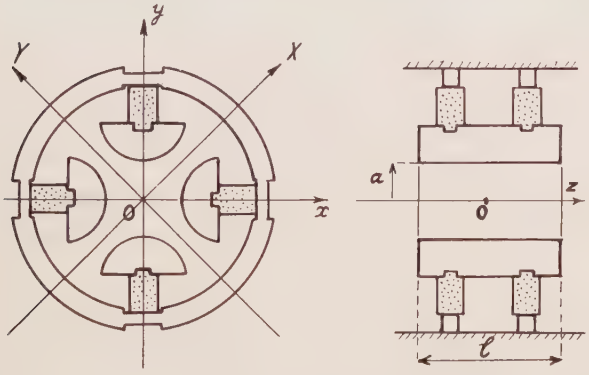

Fig. 1. (a) Schéma d'une lentille quadrupolaire électrostatique $a = 4$ cm; $l = 15$ cm.

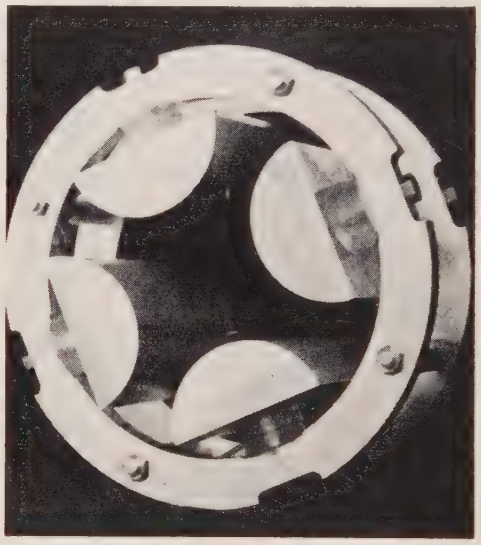

Fig. 1. (b) Photographie d'une des lentilles étudiées.

($D = 256$ mm) a été ajusté pour qu'elles puissent entrer à frottement doux dans l'enceinte à vide, ce qui permet l'alignement automatique de plusieurs lentilles. La figure 1b est une photographie d'une des lentilles utilisées.

2.2. POTENTIEL DANS UNE LENTILLE A EXCITATION SYMETRIQUE

Dans la zone centrale, si on rapporte à des axes Ox et Oy situés dans les plans de symétries xOz et yOz coupant les électrodes, et si $2\Phi_1$ représente la différence de potentiel entre deux électrodes voisines le potentiel $\Phi(x, y)$ dans l'espace utile en $z = 0$, est donné par l'expression:

$$\Phi(x, y) = -\frac{\Phi_1}{a^2}(x^2 - y^2) + \ldots$$

dans le cas de l'alimentation symétrique telle que les électrodes situées sur Ox soient portées au potentiel $-\Phi_1$ par rapport à la masse ($\Phi = 0$). On néglige les termes d'ordre supérieur, du sixième degré en x et y.

Si on tient compte des champs de fuite d'extrémité, on obtient l'expression plus générale

$$\Phi(x, y, z) = -\frac{\Phi_1}{a^2}(x^2 - y^2)\,k(z) + \frac{\Phi_1}{a^2}\frac{k''(z)}{12}(x^4 - y^4) - \ldots$$

[1]) P. Grivet et A. Septier, Nucl. Instr. et Meth. **6** (1960) 126; 243.

dans laquelle $k(z)$ représente la "fonction caractéristique" de la lentille, égale à l'unité dans la zone centrale, et $k''(z)$ sa dérivée seconde en z.

2.3. CAS DES LENTILLES A EXCITATION DISSYMETRIQUE

Lorsque l'alimentation en tension est dissymétrique par rapport à la masse (une paire d'électrodes à la masse) l'expression du potentiel est beaucoup plus complexe.

En première approximation, pour le calcul des grandeurs optiques au premier ordre, il suffit de considérer une répartition quadrupolaire du type précédent, à laquelle on superpose une répartition à symétrie de révolution du type

$$\varphi(x, y, z) = \pm \Phi_1 k(z)$$

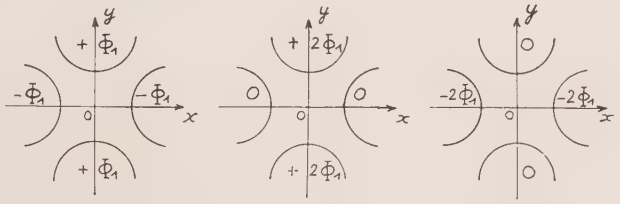

Fig. 2. Différents cas d'excitation électrique des électrodes.

d'où, au premier ordre:

$$\Phi(x, y, z) = -\frac{\Phi_1}{a^2} k(z) (x^2 - y^2 \mp a^2) .$$

Le signe $(-)$ correspond dans cette expression a des tensions nulles en Ox, et positives $(+ 2\Phi_1)$ en Oy; nous dénommerons ce cas "dissymétrique positif" ou D.P. Le signe $(+)$ au contraire donne $\Phi = 0$ en $y = \pm a$ et $\Phi = -2\Phi_1$ en $x = \pm a$; c'est le cas "dissymétrique négatif" ou D.N.

En réalité cette loi du potentiel n'est qu'approchée et, si on veut tenir compte des termes d'ordre supérieur, on doit utiliser l'expression complète du potentiel dans les systèmes à 2 plans de symétrie:

$$\Phi(x, y, z) = \varphi_0 \left[k(z) - \frac{k''(z)}{4} (x^2 + y^2) + \frac{k''''(z)}{64} (x^4 + y^4) \right]$$

$$+ \varphi_1 \left[k(z) (x^2 - y^2) - \frac{k''(z)}{12} (x^4 - y^4) \right]$$

$$+ \varphi_2 \left[k(z) (x^4 - 6x^2y^2 + y^4 - a^4) \right]$$

soit: $$\Phi(x, y, z) = \Phi_0(z) + \Phi_1(z) + \Phi_2(z) .$$

La lentille est alors équivalente à une lentille quadrupolaire symétrique caractérisée par $\Phi_1(z)$, à laquelle se superposent une lentille de révolution $(\Phi_0(z))$, et une lentille octopolaire $(\Phi_2(z))$.

Dans le cas D.P., on a:

$$\varphi_0 = + \Phi_1 , \qquad \varphi_1 = -\frac{\Phi_1}{a^2} \text{ et } \varphi_2 = \frac{\Phi_2}{a^4} > 0 .$$

Dans le cas D.N.:

$$\varphi_0 = - \Phi_1 , \qquad \varphi_1 = -\frac{\Phi_1}{a^2} \text{ et } \varphi_2 = -\frac{\Phi_2}{a^4} < 0 .$$

La constante Φ_2 représente en première approximation la moitié de la différence de potentiel existant, sur un cercle de rayon a, entre les électrodes de la lentille, portées toutes au potentiel $+\Phi_1$, et les points situés sur OX et OY; Cette d.d.p. est accessible de façon approchée par une mesure effectuée à la cuve rhéographique sur un modèle. Dans nos lentilles, on trouve par exemple

$$\lambda = \frac{\Phi_2}{\Phi_1} \simeq 0.3 \times 10^{-2} .$$

Pour le calcul des aberrations, nous aurons besoin de l'expression du potentiel total au point considéré, en tenant compte du potentiel accélérateur Φ_0. On a alors l'expression suivante de $\Phi(x, y, z)$ dans les 3 cas:

Cas S:

$$\Phi(x, y, z) = \Phi_0 - \frac{\Phi_1}{a^2} k(z) (x^2 - y^2) + \frac{\Phi_1}{a^2} \frac{k''(z)}{12} (x^4 - y^4)$$

soit

$$\Phi(x, y, z) = \Phi_0 \left[1 - \beta^2 k(z) (x^2 - y^2) + \beta^2 \frac{k''(z)}{12} (x^4 - y^4) \right] .$$

Cas D.P. (correspondant à une lentille accélératrice pour la particule incidente négative)

$$\Phi(x, y, z) = \Phi_0 - \frac{\Phi_1}{a^2} k(z) (x^2 - y^2) + \frac{\Phi_1}{a^4} \frac{k''(z)}{12} (x^4 - y^4)$$

$$+ \Phi_1 k(z) - \Phi_1 \frac{k''(z)}{4} (x^2 + y^2)$$

$$+ \frac{\Phi_2}{a^4} k(z) (x^4 - 6x^2y^2 + y^4 - a^4)$$

en négligeant la dérivée quatrième de $k(z)$ et les termes de degré supérieur au 4e. On peut écrire

$$\Phi(x,y,z) = \Phi_0 \left[1 - \beta^2 k(z) (x^2 - y^2 - a^2) - \beta^2 a^2 \frac{k''(z)}{4} (x^2 + y^2) + \beta^2 \frac{k''(z)}{12} (x^4 - y^4) + \lambda \frac{\beta^2}{a^2} k(z) (x^4 - 6x^2y^2 + y^4 - a^4) \right]$$

avec $\lambda \simeq 0.3 \times 10^{-2}$ dans notre cas.

Cas D.N. On aurait de même

$$\Phi(x,y,z) = \Phi_0 \left[1 - \beta^2 k(z) (x^2 - y^2 + a^2) + \beta^2 a^2 \frac{k''(z)}{4} (x^2 + y^2) + \beta^2 \frac{k''(z)}{12} (x^4 - y^4) - \lambda \frac{\beta^2}{a^2} k(z) (x^4 - 6x^2y^2 + y^4 - a^4) \right] .$$

2.4. MODELE RECTANGULAIRE ET MODELE EVOLUE

La fonction $k(z)$, qui ne dépend que de la géométrie des électrodes, est la même dans tous les cas. On la représentera, comme dans les lentilles magnétiques:

soit par un modèle évolué, (fig. 3a) formé d'un plateau de longueur $2z_0$ situé entre deux demi-cloches d'équation[1])

$$k(z) = \left[1 + \left(\frac{z \pm z_0}{b} \right)^2 \right]^{-2}$$

ce modèle permet de tenir compte des termes en $k'(z)$ et $k''(z)$, et par suite de calculer les aberrations.

soit par un modèle simple rectangulaire (fig. 3b); on a $k(z) = 1$ sur une longueur L dite "longueur équivalente", définie par la relation

$$L = \frac{1}{E_0} \int_{-\infty}^{+\infty} E_t \, dz$$

E_t est le champ électrique transversal et E_0 sa valeur en $z = 0$.

2.5. LONGUEUR EQUIVALENTE

On peut définir sur des parallèles à Oz des longueurs équivalentes relatives aux deux composantes E_x et E_y de E_t.

$$L_x = \frac{1}{E_x(x, y, 0)} \int_{-\infty}^{+\infty} E_x(x, y, z)\, dz$$

$$L_y = \frac{1}{E_y(x, y, 0)} \int_{-\infty}^{+\infty} E_y(x, y, z)\, dz\,.$$

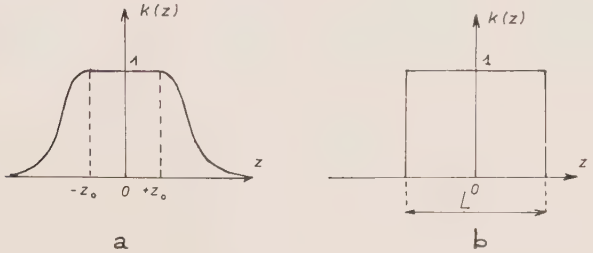

Fig. 3. Fonction caractéristique $k(z)$. (a) Modèle évolué proche de la courbe expérimentale. (b) Modèle rectangulaire simple.

Par suite des différentes symétries, on peut écrire, avec P. Lapostolle[2]):

$$+\frac{E_x(x, y, 0)\cdot L_x(x, y)}{} = A_0 + A_4\,(x^4 - 10x^2y^2 + 5y^4) + A_8\,(x^8 - 36x^6y^2 + 126x^4y^4 - 84x^2y^6 + 9y^8)$$

$$-\frac{E_y(x, y, 0)\cdot L_y(x, y)}{y} = A_0 + A_4(5x^4 - 10x^2y^2 + y^4) + A_8(9x^8 - 84x^6y^2 + 126x^4y^4 - 36x^6y^2 + y^8)\,.$$

Si on suppose que la lentille donne en $z = 0$ un champ parfaitement quadrupolaire on a:

$$E_x(x, y, 0) = Kx$$

$$E_y(x, y, 0) = -Ky$$

et on peut écrire

$$L_x(x, y) = L_0 + A(x^4 - 10x^2y^2 + 5y^4) + B(x^8 - 36x^6y^2 + 126x^4y^4 - 84x^2y^6 + 9y^8)$$

$$L_y(x, y) = L_0 + A(5x^4 - 10x^2y^2 + y^4) + B(y^8 - 36y^6x^2 + 126x^4y^4 - 84y^2x^6 + 9x^8)$$

En particulier, dans les plans de symétrie L_x et L_y ont la même valeur.

$$\text{sur } Ox \qquad L_x = L_0 + Ax^4 + Bx^8$$

$$Oy \qquad L_y = L_0 + Ay^4 + By^8$$

$$\text{sur } OX \qquad \begin{cases} L_x = L_0 - AX^4 + BX^8 \\ L_y = L_0 - AX^4 + BX^8 \end{cases} \text{ ou } L_y = L_0 - AX^4 + BX^8$$

x et X désignent la distance à l'axe et L_0 la longueur équivalente sur l'axe. Si $A > 0$ et $B \neq 0$, on voit que L_x et L_y croissent en Ox et Oy, et décroissent suivant OX et OY. Par contre, si $A = 0$ et $B \neq 0$, leur variation est identique dans tous les plans.

On ne peut ici détermier commodément les valeurs de L en tous points, les mesures de champ

[2]) P. Lapostolle, Quelques propriétés des champs de fuite et des longueurs équivalentes dans les déflecteurs magnétiques et les lentilles quadrupolaires CERN–PS. Int. LIN. 59–5 (1959).

électrique étant pratiquement irréalisables. On peut seulement déduire L_0 de mesures effectuées sur une lentille à l'aide d'un faisceau de particules chargées, comme nous le verrons plus loin.

Il est difficile de prévoir à priori une similitude complète entre lentille magnétique et lentille électrostatique car, dans le cas magnétique l'influence du champ de fuite des bobines dans les zones d'extrémité est mal connue.

3. Eléments Optiques au premier Ordre

3.1. COEFFICIENT CARACTERISTIQUE

Rappelons rapidement les formules donnant les éléments optiques d'une lentille. Les équations du mouvement, rapportées aux axes Ox et Oy sont identiques à celles du cas magnétique, relatives aux axes OX et OY. Dans le cas symétrique S, on obtient:

$$\begin{cases} x'' + \dfrac{\Phi_1}{a^2\Phi_0^*}\, k(z)\, x = 0 \\ y'' - \dfrac{\Phi_1}{a^2\Phi_0^*}\, k(z)\, y = 0 \end{cases}$$

Φ_0^* est la tension d'accélération des particules, avec correction relativiste:

$$\Phi_0^* = \Phi_0 \left(1 + \frac{e\Phi_0}{m_0c^2}\right)\left(1 + \frac{2e\Phi_0}{m_0c^2}\right)^{-1}$$

a le rayon du cercle de gorge,

$$x'' = \frac{\mathrm{d}^2x}{\mathrm{d}z^2}\,, \qquad y'' = \frac{\mathrm{d}^2y}{\mathrm{d}z^2}\,,$$

et $(2\Phi_1)$ = d.d.p. entre les électrodes voisines. Pour des électrons de 50 kV,

$$\frac{2e\Phi_0}{m_0c^2} = 9.8 \times 10^{-2} \text{ d'ou } \Phi_0^* = 0.955\, \Phi_0\,.$$

Dans l'approximation du modèle rectangulaire, $k(z) = 1$ dans toute la lentille et on pose

$$\frac{1}{a^2}\frac{\Phi_1}{\Phi_0^*} = \beta^2\,,$$

coefficient caractéristique de la lentille; β^2 dépend de la lentille et de son excitation relative. Pour des particules non relativistes, β^2 est indépendant du rapport e/m c'est à dire de la nature de la particule, propriété commune à toutes les lentilles électrostatiques.

Avec une excitation dissymétrique, on aurait pour β^2 l'expression

$$\beta'^2 = \frac{1}{a^2}\frac{\Phi_1}{\Phi_0^* \pm \Phi_1}$$

(signe + pour le cas D.P., signe − pour le cas D.N.)
c'est à dire

$$\beta'^2 = \frac{\beta^2}{1 \pm \beta^2 a^2}\,.$$

3.2. ELEMENTS CARDINAUX

Comme pour les lentilles magnétiques on obtient les expressions des deux distances focales:

$$f_x = (\beta \sin \beta L)^{-1}, \qquad f_y = -(\beta \operatorname{sh} \beta L)^{-1}$$

de l'abscisse des foyers image F'_x et F'_y par rapport à la face de sortie A de la lentille (fig. 4)

$$s_x = \frac{\cos \beta L}{\beta \sin \beta L}, \qquad s_y = \frac{\operatorname{ch} \beta L}{\beta \operatorname{sh} \beta L}$$

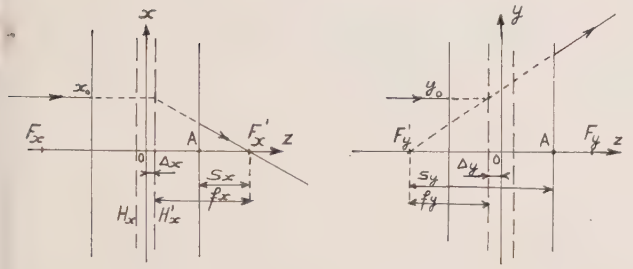

Fig. 4. Eléments cardinaux d'une lentille. (a) Plan convergent. (b) Plan divergent.

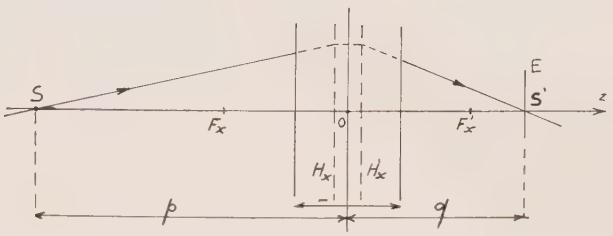

Fig. 5. Trajet d'un rayon dans le plan convergent: S, point objet; S' focale image.

de celle des plans principaux H'_x et H'_y par rapport au centre de la lentille

$$\Delta_x = \overline{OH'_x} = \overline{OF'_x} + \overline{F'_x H'_x} = \frac{L}{2} + \frac{\cos \beta L - 1}{\beta \sin \beta L}$$

$$\Delta_y = \overline{OH'_y} = \overline{OF'_y} + \overline{F'_y H'_y} = \frac{L}{2} + \frac{1 - \operatorname{ch} \beta L}{\beta \operatorname{sh} \beta L}.$$

3.3. DETERMINATION DE L

En utilisant les formules ci-dessus, et en mesurant Φ_1 et Φ_0, il est possible de calculer L lorsqu'on connait les positions respectives d'un point objet situé sur l'axe Oz de la focale image réellefournie par la lentille. Cette détermination a été effectuée sur le banc d'optique spécial décrit précédemment[1,3]). Si on nomme p la distance de l'objet S au centre O de la lentille, q celle de l'écran où se forme la focale pour une excitation donnée caractérisée par β^2(ou β'^2), on applique la relation de Newton (voir fig. 5):

$$\overline{SF} \cdot \overline{S'F'} = f_x^2$$

$$\left[\left(p - \frac{L}{2}\right) - \frac{\cos \beta L}{\beta \sin \beta L}\right]\left[\left(q - \frac{L}{2}\right) - \frac{\cos \beta L}{\beta \sin \beta L}\right] = \frac{1}{\beta^2 \sin^2 \beta L}$$

et on résout numériquement, l'inconnue étant L, pour différentes valeurs de p et q. L a été ainsi calculée avec 2 valeurs de p et de q pour les lentilles Q_1 et Q_2 décrites en § 2.1, dans les cas S, DP et DN. On trouve dans les 3 cas la même valeur, à la précision des mesures près (0.5×10^{-2} environ):

$$L_0 \approx 185 \text{ mm}$$

valeur égale à celle que le même calcul donnait pour les lentilles magnétiques[1]), tandis que les mesures de champ conduisaient à $L_0 \approx 194$ mm. La longueur équivalente L_0 d'une lentille électrostatique est donc identique à celle d'une lentille magnétique de même géométrie.

Lorsque les lentilles sont munies de diaphragnes d'entrée et de sortie plans réunis à la masse, dont le

[3]) A. Septier, C. R. Ac. Sc. Paris **245** (1957) 1406.

trou central a un rayon $r = 4$ cm, et situés à une distance d de l'extrémité des électrodes (fig. 6), L est réduite et tend vers la longueur mécanique l.

$$\begin{aligned} \text{pour} \quad d &= \infty & L_0 &\approx 185 \text{ mm} \\ d &= 50 \text{ mm} & L_0 &\approx 175 \text{ mm} \\ d &= 10 \text{ mm} & L_0 &\approx 155 \text{ mm} \\ \text{avec } l &= 150 \text{ mm}. \end{aligned}$$

3.4. ABAQUES DE FONCTIONNEMENT D'UN DOUBLET

Pour un doublet formé de 2 lentilles Q_1 et Q_2 identiques sans diaphragme, distantes de $O_1O_2 = 50$ cm, nous avons cherché les valeurs des excitations β_1^2 (sur Q_1) et β_2^2 (sur Q_2) qui amènent successivement sur l'écran la première puis la seconde focale correspondant à un point objet S situé sur l'axe en avant du doublet à la distance D_1 (fig. 7). La figure 8 montre les résultats obtenus pour deux distances objet

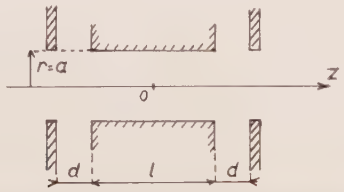

Fig. 6. Schéma d'une lentille munie de diaphragmes.

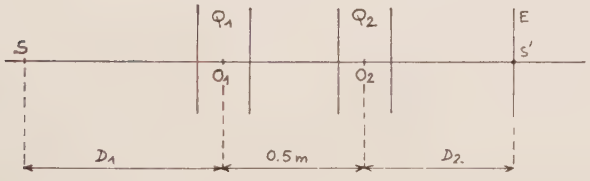

Fig. 7. Doublet quadrupolaire: S, point objet; S' focale image.

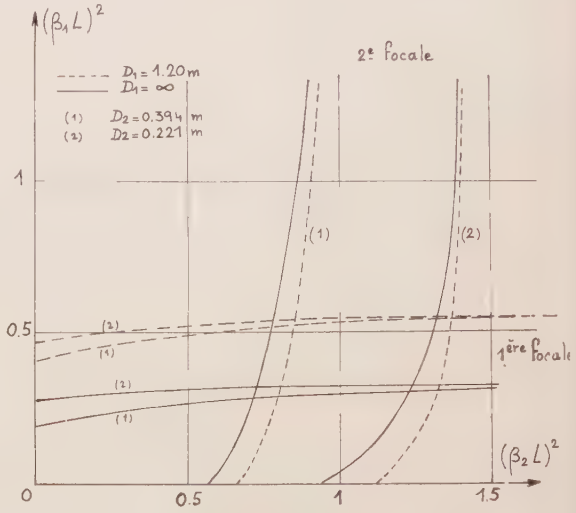

Fig. 8.
Abaque de fonctionnement d'un doublet. Point image à l'infini.

$O_1S = 120.5$ cm et $Q_1S = \infty$ et, dans chaque cas, deux valeurs de la distance image $O_2S = 39.4$ cm et $O_2S = 22.1$ cm. Les coordonnées sont les facteurs sans dimensions $(\beta_1 L)^2$ et $(\beta_2 L)^2$, avec $L = 19.4$ cm. En particulier pour $\beta_1 = \beta_2$ (doublet symétrique), on obtient la première focale sur l'écran pour $(\beta L)^2 = 0.245$ soit $\beta \simeq 2.66$ m^{-1} et la seconde focale pour $(\beta L)^2 = 0.840$ soit $\beta \simeq 4.35$ m^{-1} lorsque $O_2E = 0.39$ m et l'objet situé à l'infini, ce qui correspond à des distances focales du doublet de $F_x \simeq 1.25$ m et $F_y \simeq 0.16$ m (on peut utiliser la formule qui donne la distance focale $F_x = F_y = F$ d'un doublet symétrique:

$$\frac{1}{F} = -\beta \{ \cos \beta L \operatorname{sh} \beta L - \sin \beta L \operatorname{ch} \beta L - \beta(D - L) \sin \beta L \operatorname{sh} \beta L \} .$$

4. Mesures et Correction de l'Aberration d'Ouverture

4.1. MESURE DE L'ABERRATION TRANSVERSALE D'UN DOUBLET[4])

4.1.1. *Cas symétrique*

Les deux lentilles Q_1 et Q_2, placées sur Oz avec $O_1O_2 = 0.5$ m, et telles que $O_2E = 0.394$ m, subissent même excitation. Un faisceau incident creux cylindrique, parallèle à l'axe, de rayon R_0 variable, pénètre

[4]) A. Septier et J. Van Acker, C.R. Ac. Sc. Paris **251** (1960) 346.

dans le doublet. On règle l'excitation pour obtenir sur E la 1ère (ou 2ème) focale réelle du système, et on observe l'évolution de la forme de la section du faisceau quand Φ_1 varie légèrement.

On observe successivement les aspects représentés sur la fig. 9 lorsque Φ_1 croît; Pour Φ_1 fixé, on rencontrerait les figures 9 a b c d en s'éloignant du doublet, contrairement au cas des lentilles magnétiques[1]). Les lentilles électrostatiques, avec excitation symétrique, et les lentilles magnétiques, ont donc respectivement des aberrations d'ouverture de *signe opposé.*

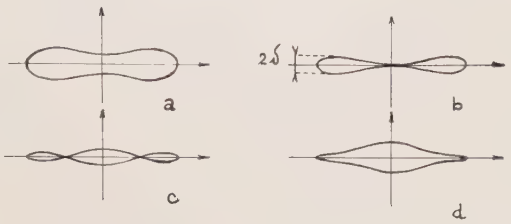

Fig. 9. Sections transversales du faisceau émergent au voisinage d'une focale: influence de l'aberration du 3ème ordre.

On définit ici encore le taux d'aberration transversale par la relation: (2δ représentant l'épaisseur maximum de la figure 9b.)

$$\tau = \frac{\delta}{R_0}.$$

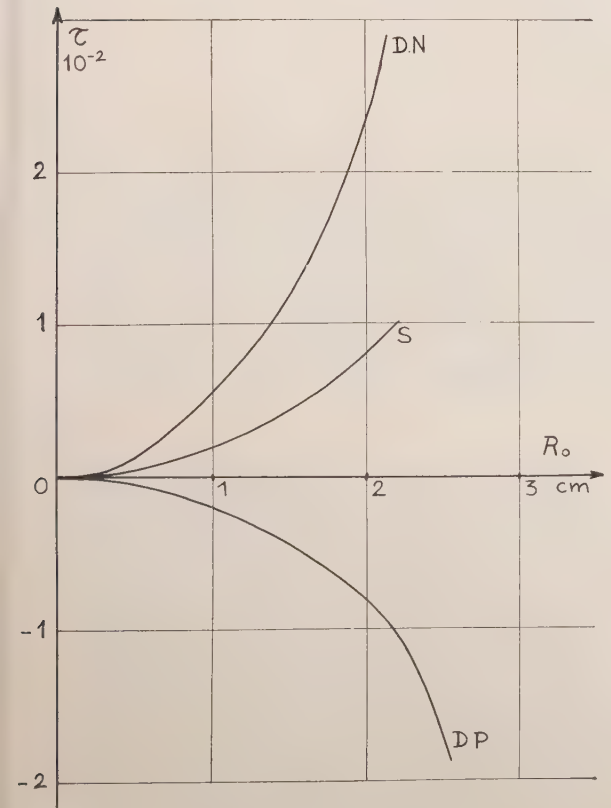

Fig. 10. Taux d'aberration d'une lentille unique dans les trois cas d'excitation de la figure 2, en fonction du rayon R_0 du faisceau creux incident.

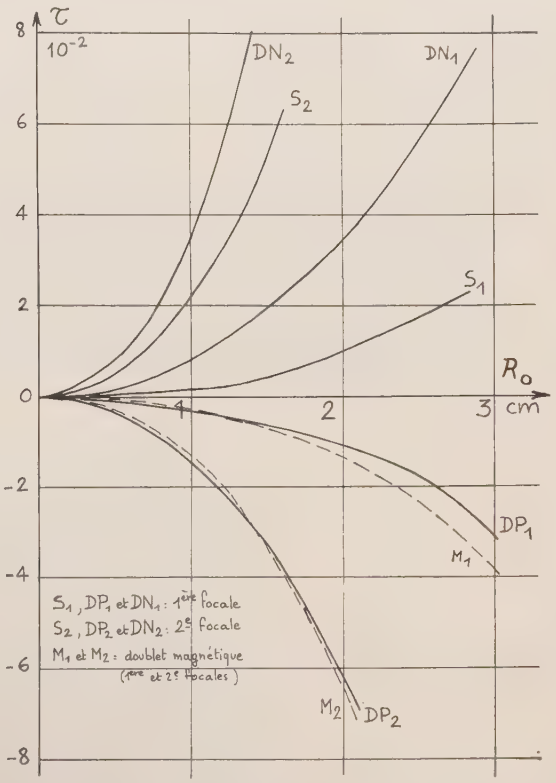

Fig. 11. Taux d'aberration d'un doublet symétrique.

La valeur de τ a été mesurée

pour Q_2 seule (une seule focale réelle) située à 39.4 cm de E

pour le doublet (deux focales réelles)

La figure 10 donne la courbe d'aberration de Q_2 seule; la fig. 11 celles du doublet pour la 1ère et la 2e focale amenées sur E (courbes S).

4.1.2. *Cas dissymétriques*

Dans le cas D.N., l'évolution est la même que précédemment, mais l'aberration est considérablement renforcée. τ est donné par les courbes D.N. des fig. 10 et 11. Dans le cas D.P., l'aberration est du même ordre de grandeur que le cas S, *mais le sens de l'aberration est inversé*: les figures défilent sur l'écran de (d) à (a) lorsque Φ_1 croît. On a alors les courbes D.P. des fig. 10 et 11. Nous avons porté pour comparaison sur ces figures les courbes relatives à un doublet magnétique[1]). On voit que dans le cas S et D.P. le taux d'aberration est pratiquement le même que celui du doublet magnétique.

Pour la première focale, la distance focale du doublet est de $F \approx 1.25$ m et pour la seconde: $F \approx 0.16$ m.

Lorsque la distance focale diminue (par exemple lorsqu'on observe les focales sur l'écran situé à 22 cm de Q_2), l'aberration croît dans tous les cas (S, D. P. ou D.N.) en valeur absolue, mais le sens reste le même dans chaque cas. Comme dans le cas magnétique, la variation de τ avec F suit sensiblement la loi: $\tau(F) \simeq 1/F$. Ce qui permet de prévoir, pour $F = 3.6$ m (c'est-à-dire $\beta = 2\ \mathrm{m}^{-1}$) et $R_0 = 3$ cm.

$\tau \approx 8 \times 10^{-3}$ dans le cas S et $\tau \simeq 10^{-2}$ dans les cas D.P. pour la 1ère focale.

Les aberrations d'ouverture ont été calculées dans le cas du doublet magnétique[1]) et dans le cas du doublet électrostatique (voir plus loin) pour cette valeur $\beta = 2\ \mathrm{m}^{-1}$.

4.2. INFLUENCE DE DIFFERENTES PERTURBATIONS DES CHAMPS DE FUITES

4.2.1. *Influence de diaphragmes d'entrée et de sortie*

Les valeurs de τ_x et τ_y ont été mesurées pour le doublet symétrique muni des diaphragmes décrits en § 3.3., dans les 3 cas. La figure 12 montre les variations de τ_x (1ère focale, $F \approx 1.25$ m) pour $d = \infty$, $d = 50$ mm et $d = 10$ mm, dans les 3 cas., et le tableau 1 donne un ordre de grandeur de τ_x (1ère focale) pour $R_0 = 2$ cm et de τ_y (2e focale, $F \simeq 0.16$ m) pour $R_0 = 1$ cm, lorsque $O_1O_2 = 50$ cm et $O_2E = 39$ cm.

Tableau 1

		cas S	cas D.P.	cas D.N.
τ_x ($R_0 = 2$ cm)	$d = \infty$	10^{-2}	-10^{-2}	3.5×10^{-2}
	$= 50$ mm	2×10^{-2}	-2×10^{-2}	4×10^{-2}
	$= 10$ mm	3×10^{-2}	-7×10^{-2}	10.5×10^{-2}
τ_y ($R_0 = 1$ cm)	$d = \infty$	2×10^{-2}	-10^{-2}	3.5×10^{-2}
	$= 50$ mm	2.5×10^{-2}	-1.5×10^{-2}	5.5×10^{-2}
	$= 10$ mm	9×10^{-2}	-16×10^{-2}	25×10^{-2}

L'accroissement est surtout important lorsque d passe de 50 mm à 10 mm: il peut atteindre un facteur compris entre 3 et 10 selon le type d'excitation et la convergence.

4.2.2. *Rapprochement des lentilles* Q_1 et Q_2

La lentille Q_1 a été rapprochée de Q_2 de façon à obtenir $O_1O_2 = 18.6$ cm avec $O_2E = 22$ cm. Dans une première expérience, les lentilles Q_1 et Q_2 étaient munies des diaphragmes situés à $d = 10$ mm, puis ces diaphragmes ont été enlevés.

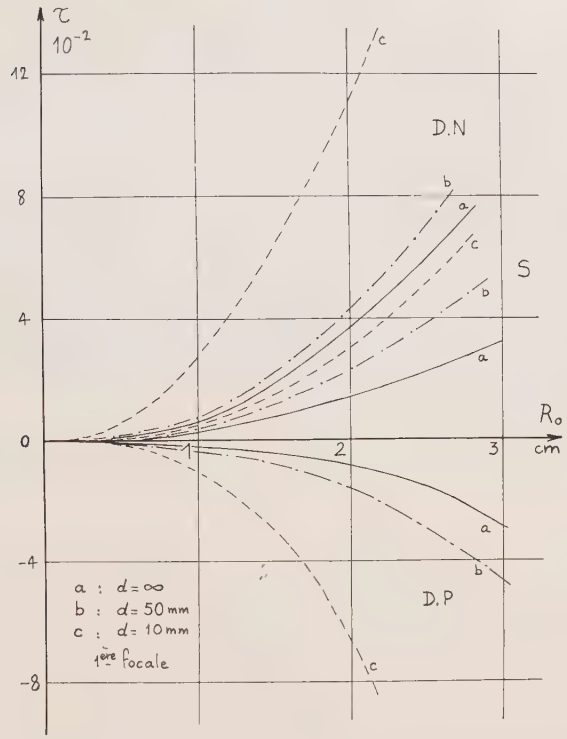

Fig. 12. Influence des diaphragmes sur le taux d'aberration.

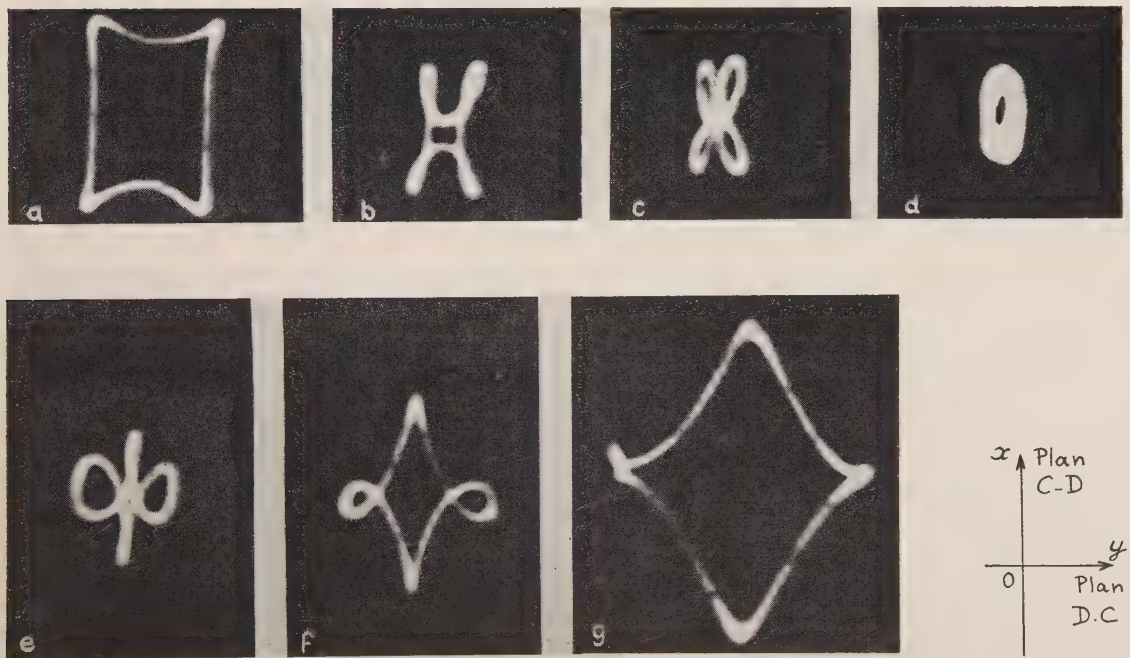

Fig. 13. Sections transversales du faisceau émergent dans le cas d'un fonctionnement pseudo-stigmatique (excitation dissymétrique négative).

Si l'excitation est symétrique, les aberrations restent inchangées dans les deux séries d'expériences, aussi bien pour τ_x que pour τ_y.

Excitation D.N.: il en est de même, les valeurs de τ_x et τ_y étant maintenant très grandes pour $R_0 = 2$ cm, $\tau_x \simeq 25 \times 10^{-2}$ et pour $R_0 = 1$ cm $\tau_y \simeq 10 \times 10^{-2}$ (alors qu'on a $\tau_x \simeq 3.5 \times 10^{-2}$ et $\tau_y \simeq 9 \times 10^{-2}$ dans le cas S). D'autre part l'écart entre τ_x et τ_y, correspondant à une même valeur de R_0, est plus faible pour $O_1O_2 = 18.6$ cm que pour $O_1O_2 = 50$ cm.

Excitation D.P.: si les lentilles portent des diaphragmes, les courbes $\tau_x(R_0)$ et $\tau_y(R_0)$ sont très proches l'une de l'autre, avec $\tau_y \simeq 4 \times 10^{-2}$ pour $R_0 = 1$ cm et $\tau_x \simeq 14 \times 10^{-2}$ pour $R_0 \simeq 2$ cm. Mais si on enlève les diaphragmes les aberrations de la 2e focale sont beaucoup plus faibles que celles de la première. Pour $R_0 = 2$ cm, on aurait $\tau_x \simeq 14 \times 10^{-2}$, mais pour $R_0 = 1$ cm, $t_y \simeq 10^{-2}$ au lieu de 4×10^{-2} précédemment. Ces anomalies sont certainement dues aux très grandes perturbations subies par les champs de fuites.

Notons ici que toutes ces variations du taux d'aberrations se font, pour un même type d'excitation, sans changement de signe de l'aberration elle-même. Mais de toute manière il sera préférable de séparer au maximum les lentilles, ou, si on les rapproche, d'utiliser une excitation symétrique.

4.3. FIGURES D'ABERRATION EN REGIME PSEUDO-STIGMATIQUE

Il est possible, en excitant différemment Q_1 et Q_2 ($(\beta.L)_2^2 = 0.74$, $(\beta L)_1^2 = 0.33$), de faire coïncider sur E les 2 focales. Les grandissements G_x et G_y étant différents dans les 2 plans xOz et yOz, le système est dit "pseudo-stigmatique". Nous avons observé sur l'écran, pour $R_0 = 2$ cm, l'évolution de la section du faisceau au voisinage de la pseudo-focale double. Les figures obtenues sont représentées sur la fig. 12 dans le cas D.N.; elles défilent de (a) à (g) lorsque la tension croît.

Burfoot[5]) a décrit le premier les figures d'aberration des systèmes optiques à 2 plans symétrie, mais seulement dans le cas où $G_x = G_y = G$. On peut obtenir dans le plan image de Gauss (correspondant à des rayons incidents très voisins de l'axe) soit un cercle, comme pour les systèmes de révolution, soit une étoile à quatre pointes, soit une rosette (fig. 14) soit enfin une figure complexe due à la superposition de ces

Fig. 14. Les trois composantes fondamentales de l'aberration du 3ème ordre. (a) Cercle (aberration sphérique pure). (b) Etoile pure. (c) Rosette pure.

trois aberrations élémentaires. Les sections représentées fig. 13 montrent que notre doublet, avec $R_0 = 2$ cm, (ce qui correspond à des trajectoires très éloignées de l'axe dans le plan "divergent-convergent" yOz: $y_{max} \simeq 4$ cm) ne possède pratiquement que des aberrations du 3e ordre. Les aberrations dues aux non linéarités du gradient peuvent être négligées. A partir de la figure 13e, observée dans le plan de Gauss, on pourrait calculer les coefficients d'aberration du doublet.

En excitation symétrique S, on observe des figures rigoureusement identiques, mais 3 fois plus petites pour la même valeur de R_0 (La figure 13e est telle que $x = \pm 3.5$ mm et $y = \pm 3$ mm).

Dans les cas D.P. l'évolution est inversée lorsque l'excitation croît; les aberrations sont faibles, et le défaut d'alignement permet difficilement de reconnaître les figures typiques du troisième ordre (fig. 15 abcde).

[5]) J. C. Burfoot, Proc. Phys. Soc. B **67** (1954) 523.

On peut donc envisager de corriger les aberrations d'un système quadrupolaire à l'aide de lentilles octopolaires, créant des perturbations du troisième degré en R_0. Nous verrons que dans le cas du fonctionnement astigmatique (focales séparées), une seule lentille octopolaire permet de corriger la focale observée sur l'écran.

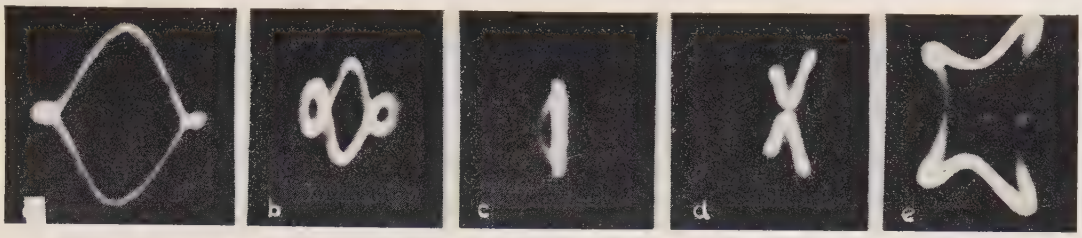

Fig. 15. Fonctionnement pseudo-stigmatique, excitation dissymétrique positive.

4.4. TENTATIVE DE CORRECTION DE L'ABERRATION D'OUVERTURE EN FONCTIONNEMENT ASTIGMATIQUE[6])

4.4.1. *Modification des pôles*

La correction de l'aberration d'ouverture a pu être effectuée sur des lentilles magnétiques par modification de la section des pôles[1]). Cette modification, qui consiste à réduire les entrefers latéraux entre pôles adjacents, provoque un accroissement de la longueur équivalente de la lentille dans les plans respectivement convergent et divergent zOX et zOY, et une diminution de cette longueur dans les plans zOx et zOy qui coupent les pôles. Cet effet a donc une symétrie octopolaire; les variations de convergence ainsi obtenues ne sont pas rigoureusement proportionnelles à r^3 mais l'expérience montre qu'on peut arriver à une compensation presque totale des aberrations pour toutes les valeurs de R_0, dans un domaine relativement large de convergence.

Dans une lentille électrostatique, les plans convergent et divergent sont respectivement zOx et zOy. Une modification identique des pôles, sur une aberration de même signe que celle des lentilles magnétiques (cas D.P.), aura un effet inverse, mais aura le même effet sur une aberration de signe contraire (cas S et D.N.)

Nous avons tenté cette correction sur une lentille unique, munie successivement des pôles représentés sur la fig. 16a. Dans le cas S on obtient effectivement, en allant du pôle plan au pôle circulaire, les courbes de la fig. 16b: il existe bien une configuration assez proche de l'hyperbole théorique, mais située à l'extérieur de celle-ci, pour laquelle l'aberration est pratiquement nulle. Avec les électrodes planes, l'aberration est sensiblement la même et a le même signe pour tous les cas d'excitation; la section du faisceau est très perturbée (fig. 17), et nous définissons le taux d'aberration à partir de la largeur du premier maximum. Les boucles d'extrémité dont dues aux non-linéarité du champ, et le croisement indique que les aberrations supplémentaires ainsi mises en évidence sont de signe contraire à l'aberration normale d'ouverture. Notons encore que les pôles formés de facettes planes, se rapprochant de l'hyperbole donne des aberrations plus faibles que les pôles circulaires.

Dans le cas D.N, on obtient la correction pour un pôle très extérieur à l'hyperbole. Dans le cas D.P. la compensation se produit seulement pour des pôles très étroits; mais les non-linéarités provoquent alors des aberrations d'ordre supérieur importantes. Pratiquement, l'aberration ne peut être corrigée par cette technique que dans le cas S en utilisant des pôles légèrement extérieurs à l'hyperbole théorique.

4.4.2. *Dissymétrie d'excitation*

L'expérience a montré que le passage du cas S au cas D.P. provoquait un changement de signe de l'aberration; l'introduction d'un certain taux de dissymétrie positive doit permettre la correction. Si on

[6]) A. Septier et J. Van Acker, C.R. Ac. Sc. Paris **251** (1960) 1750.

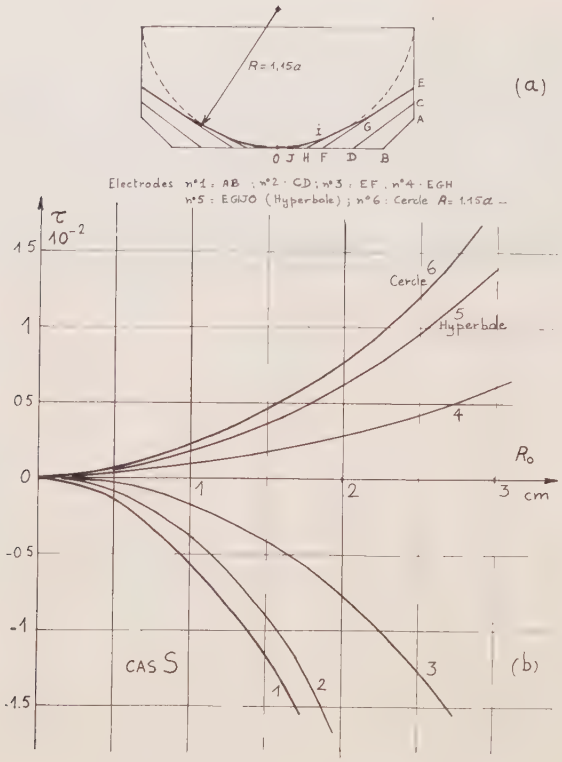

Fig. 16. (a) Coupe transversale des différentes électrodes utilisées. (b) Variation du taux d'aberration avec la forme des électrodes.

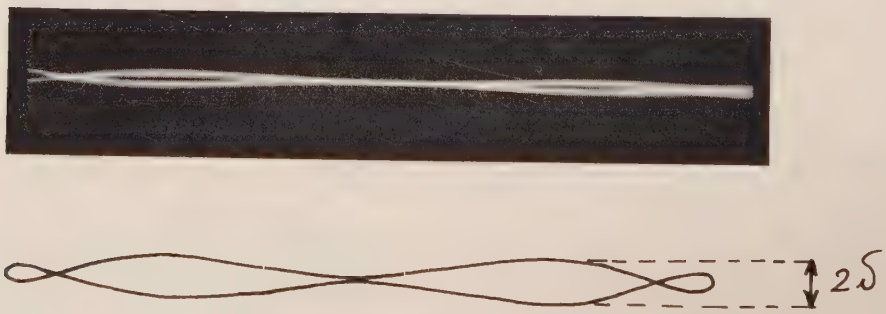

Fig. 17. Influence de l'aberration du 5ème ordre sur la forme de la pseudo-focale.

applique une tension $-\Phi'_1$ sur deux des pôles, $+\Phi_1$ sur les deux autres pôles, on peut caractériser la dissymétrie par le facteur $\mu = |\Phi'_1/\Phi_1|$; si $\mu = 0$ on retrouve le cas D.P., si $\mu = 1$, on a le cas S.

Les courbes de la figure 18 ont été obtenues avec une lentille unique. Pour $\mu \simeq 0.5$, la correction est totale de $R_0 = 0$ à $R_0 = 3$ cm, pour $f_x \simeq 40$ cm. On a pu de même corriger un doublet symétrique. La valeur de μ varie évidemment lorsqu'on passe de la 1ere focale ($F_x \simeq 1.25$ m) à la 2e focale ($F_y \simeq 0.16$ m).

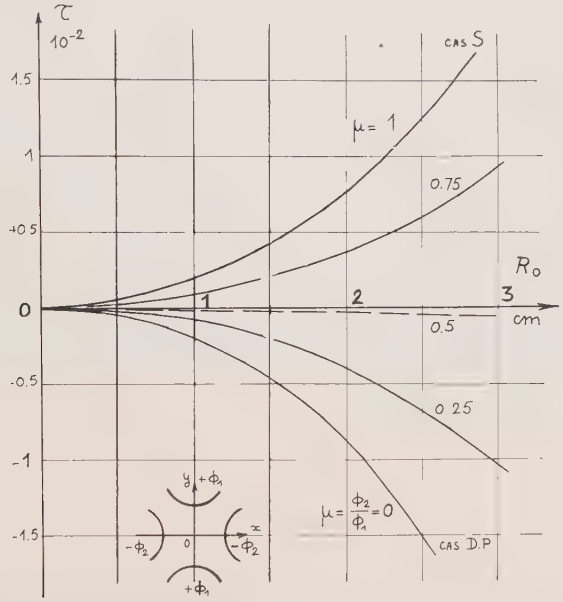

Fig. 18. Correction de l'aberration du 3ème ordre par dissymétrie d'excitation.

4.4.3. *Correction d'un doublet symétrique par une lentille octopolaire*

Cette lentille est formée d'électrodes de section cylindrique de rayon $r = 2$ cm, de longueur $l = 10$ cm, tangentes à un cercle de gorge de rayon $a' = 5$ cm (fig. 19). Elle est placée à la suite du doublet, avec son centre Oz à 20 cm de Q_2. Ses 4 plans de symétrie géométriques coïncident avec ceux du doublet. Son action sur la forme de la 2e focale ($F_y \simeq 0.16$ m) est représentée sur la fig. 20 ; on nomme ici λ le rapport de la tension $(-2\Phi_2)$ appliquée à 4 des électrodes de l'octopole, à la tension $(-2\Phi_1)$ appliquée aux lentilles du doublet, lorsque toutes les autres électrodes sont reliées à la masse (cas D.N.).

Si $\Phi_2 = 0$, on obtient, pour $R_0 = 1.5$ cm, la fig. 20a ; si la tension $(-2\Phi_2)$ est appliquée sur les 4 électrodes situées en zOX et zOY (octopole convergent dans ces 2 plans), on obtient une correction totale pour $\lambda \simeq 0.5$ (fig. 20b) ; puis l'aberration réapparaît en changeant de signe (fig. 20c) ; si au contraire $(-2\Phi_2)$ est appliquée en zOx et zOy (octopole divergent en zOX et zOY), l'aberration augmente : fig. 20 d et e.

Des essais ont été tentés pour la correction de la figure d'aberration obtenue on fonctionnement pseudo-stigmatique, lorsqu'on fait apparaître sur l'écran la rosette dissymétrique de la fig. 13c. On ne peut obtenir ici de correction totale par suite de l'astigmatisme résiduel, (le faisceau issu du doublet n'est pas de révolution) mais on améliore de façon très sensible la qualité du doublet ; la figure 21a montre l'évolution de la section du faisceau lorsque l'excitation des lentilles croît (cas D.N.), en laissant le rapport $\Phi_{Q1}/\Phi_{Q2} = 0.44$ constant, ainsi que le rayon du faisceau incident, avec l'octopole non excité. La figure 21c montre les figures obtenues lorsque la tension de l'octopole est égale à Φ_{Q2}, mais avec les plans convergents de l'octopole situés à 45° des plans zOx et zOy. La tache de moindre confusion (21c n° 4) a une étendue beaucoup moindre. Si l'octopole est convergent en zOx et zOy, les aberrations sont renforcées (21b).

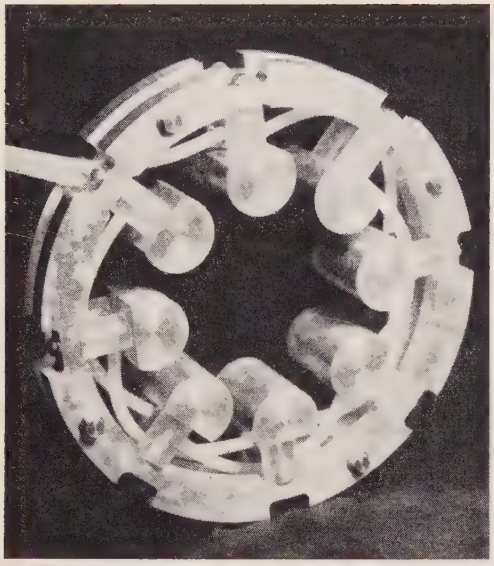

Fig. 19.

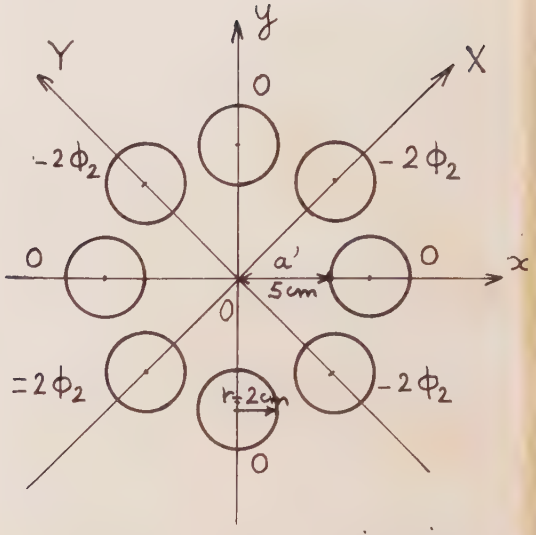

Fig. 19. Lentille octopolaire.

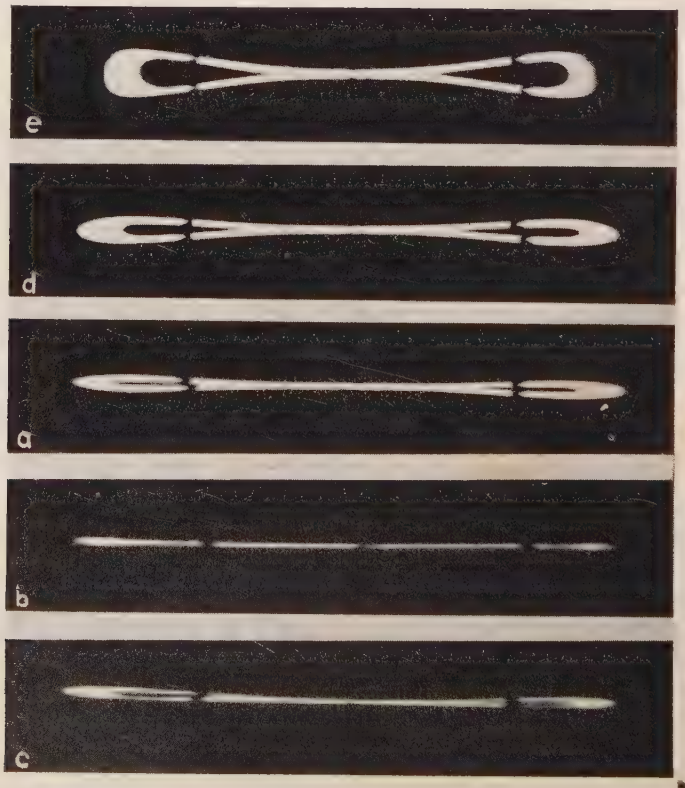

Fig. 20. Correction de l'aberration du 3ème ordre grâce a une lentille octopolaire (excitation dissymétrique négative).

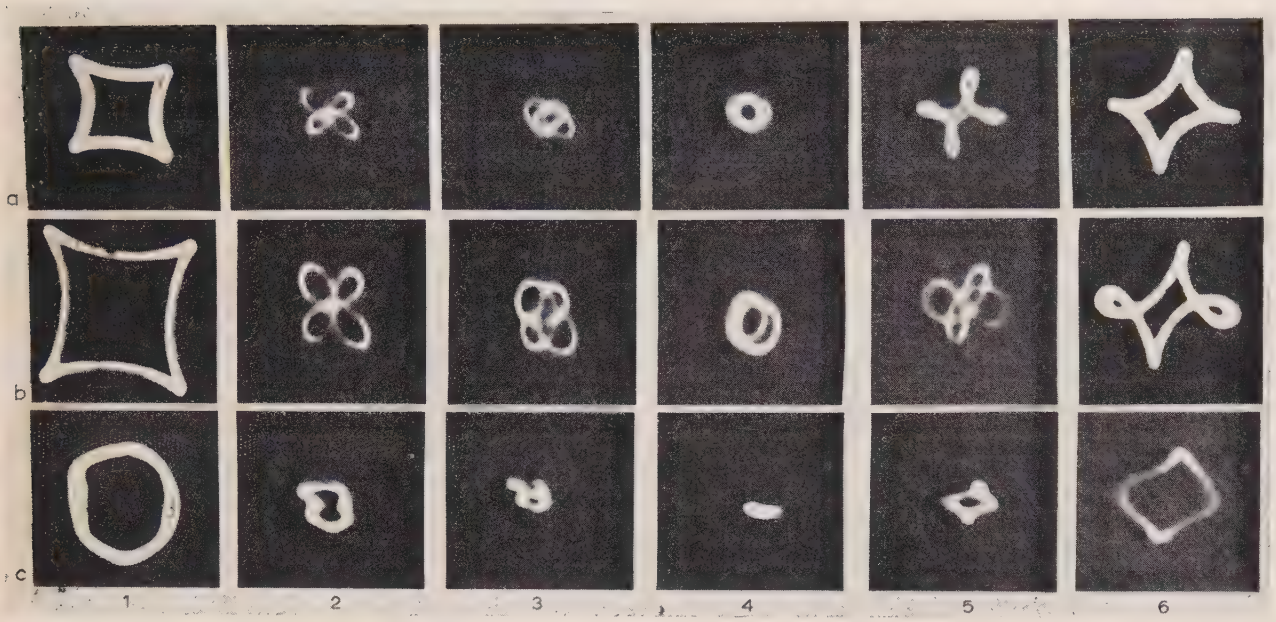

Fig. 21. Influence d'une lentille octopolaire sur l'aberration du 3ème ordre (excitation D.N.) en fonctionnement pseudo-stigmatique. (a) Lentille octopolaire non excitée. (b) Lentille octopolaire excitée renforçant l'aberration. (c) Lentille excitée convenablement: l'aberration diminue.

Des essais seront entrepris sur un triplet symétrique, dans le cas d'un fonctionnement réellement stigmatique (système de grandissement unité); un tel ensemble corrigé pourrait être utilisé comme système optique d'un séparateur H.F. de particules relativistes, du type de celui qui est prévu au CERN.

4.5. MECANISME DE LA CORRECTION

Les différents résultats expérimentaux permettent d'interpréter simplement le mécanisme des différentes méthodes de correction de l'aberration d'ouverture.

La correction par dissymétrie d'excitation est équivalente à la correction par octopole. En effet, l'expression du potentiel $\Phi(x, y, z)$ contient, on l'a vu, dès qu'on sort du cas S un terme à symétrie octopolaire, dont l'amplitude peut être caractérisée par le facteur $\lambda = \Phi_2/\Phi_1$. Pour des pôles hyperboliques de dimensions infinies, ce terme serait négligeable, même dans les cas D.P. ou D.N.: le calcul donne $\lambda \leqslant 10^{-4}$. Mais avec des pôles de dimensions finies, placés dans une enceinte portée au potentiel $\Phi = 0$ située à une distance relativement faible de l'espace utile, on atteint facilement $\lambda \simeq 0.3 \times 10^{-2}$. Chaque lentille quadrupolaire à excitation dissymétrique (figure 22a) est donc équivalente à la superposition d'une lentille quadrupolaire symétrique, d'une lentille de révolution, et d'une lentille octopolaire faible (figure 22b).

Dans le cas D.N., l'octopole équivalent renforce l'aberration du cas S, car il est divergent en OX, OY (figure 23a). Dans le cas D.P. au contraire, il est convergent en OX, OY (figure 23b), mais cette convergence est trop forte: il y a sur-correction. Si on diminue λ aux environs de $\lambda \simeq 0.1 \times 10^{-2}$, en introduisant un taux de dissymétrie positive inférieur à 1, on obtient la correction totale (voir § 4.4.2).

La compensation par modification de la forme des pôles fait intervenir les termes d'ordre supérieur du champ. Si on réduit l'écart entre les pôles, on accroît la convergence (ou la divergence) en OX et OY, et on la diminue en Ox et Oy[1]). Dans le cas S, on pourra donc compenser l'aberration en utilisant des pôles dont la méridienne est extérieure au cercle, ou même à l'hyperbole théorique. Dans le cas D.N. la compensation sera obtenue en agissant dans le même sens; on réduit en même temps la valeur de λ, et

l'influence défavorable de ce facteur. Dans le cas D.P., un élargissement des pôles diminue également λ, (ce qui fait décroître l'aberration), mais l'influence, défavorable ici, des variations de convergence l'emporte et l'aberration croît, en gardant le même signe. Pour la compenser, il faut au contraire diminuer la largeur des pôles, c'est à dire diminuer la convergence en OX, OY et l'accroître en Ox, Oy; le terme octopolaire ne croît pas suffisamment vite, et une compensation est possible pour des pôles très étroits.

La correction d'un ensemble de lentilles quadrupolaires en fonctionnement stigmatique nécessite

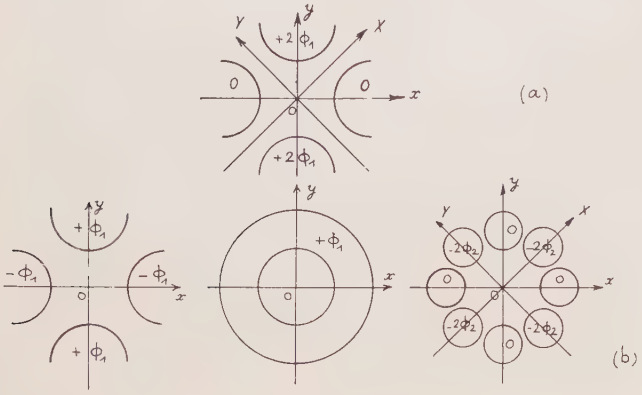

Fig. 22. (a) Lentille quadrupolaire avec excitation dissymétrique positive. (b) Les trois lentilles simples dont la superposition équivaut à la lentille précédente.

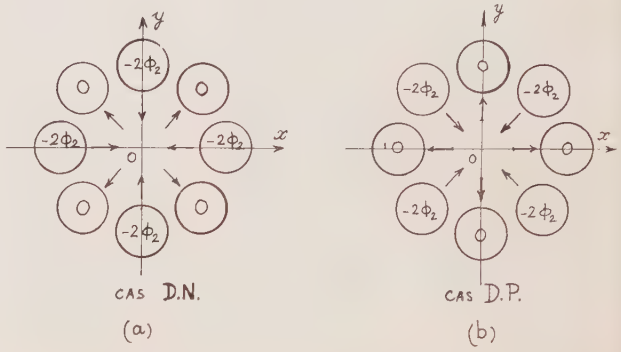

Fig. 23. Lentille octopolaire fictive équivalente à l'action d'une dissymétrie d'excitation du quadrupole. (a) Cas D.N. (b) Cas D.P.

théoriquement la présence de trois octopoles indépendants, car l'aberration d'ouverture est caractérisée ici par trois coefficients différents[5]): on peut donc envisager la correction d'un triplet symétrique en introduisant dans les trois lentilles des taux de dissymétrie différents.

5. Calcul de l'Aberration d'Ouverture en fonctionnement astigmatique[7])

5.1. EQUATION DU MOUVEMENT "AU 3 ORDRE"

Pour des particules incidentes non relativistes, en partant de l'équation générale

$$\frac{\mathrm{d}}{\mathrm{d}t}(m\boldsymbol{v}) = e\boldsymbol{E} \tag{1}$$

et de l'expression de la vitesse longitudinale

$$\left(\frac{\mathrm{d}z}{\mathrm{d}t}\right)^2\left(1+\left(\frac{\mathrm{d}x}{\mathrm{d}z}\right)^2+\left(\frac{\mathrm{d}y}{\mathrm{d}z}\right)^2\right)=\Phi\, 2e(x,y,z) \tag{2}$$

on arrive à la relation

$$\frac{\mathrm{d}}{\mathrm{d}z}\left[\left(\frac{\Phi(x,y,z)}{1+x'^2+y'^2}\right)^{\frac{1}{2}}\frac{\mathrm{d}\boldsymbol{s}}{\mathrm{d}z}\right]=\frac{\boldsymbol{E}}{2}\left(\frac{1+x'^2+y'^2}{\Phi(x,y,z)}\right)^{\frac{1}{2}}. \tag{3}$$

Dans le cas relativiste, on aurait

$$\frac{\mathrm{d}}{\mathrm{d}z}\left[\left(\frac{\Phi(x,y,z)\,(1+\varepsilon\Phi(x,y,z))}{1+x'^2+y'^2}\right)^{\frac{1}{2}}\frac{\mathrm{d}\boldsymbol{s}}{\mathrm{d}z}\right]=(1+2\varepsilon\Phi(x,y,z))\left(\frac{1+x'^2+y'^2}{\Phi(x,y,z)\,(1+\varepsilon\Phi(x,y,z))}\right)^{\frac{1}{2}}\frac{\boldsymbol{E}}{2} \tag{4}$$

avec $\varepsilon = |e|/2m_0c^2$, $|e|$ désignant la valeur absolue de la charge électrique.

$\mathrm{d}\boldsymbol{s}$ représente un élément de trajectoire, x', y' les projections de la pente de la trajectoire sur les plans xOz et yOz respectivement, et $\Phi(x,y,z)$ le potentiel total, dont l'expression a été donnée au § 2.3.

[7]) A. Septier, C.R. Ac. Sc. Paris **252** (1961) 285.

Les équations du mouvement au 3e ordre ont été déterminées pour des particules non relativistes, grâce à la relation précédente projetée sur xOz et yOz.

Remarque: On peut y parvenir également en partant de la relation algébrique

$$\frac{\mathrm{d}^2x}{\mathrm{d}z^2} = \frac{\dfrac{\mathrm{d}^2x}{\mathrm{d}t^2} - \dfrac{\mathrm{d}x}{\mathrm{d}z}\cdot\dfrac{\mathrm{d}^2z}{\mathrm{d}t^2}}{\left(\dfrac{\mathrm{d}z}{\mathrm{d}t}\right)^2} \tag{5}$$

qui, pour des particules non relativistes s'écrit simplement:

$$x'' = \frac{x'E_z - E_x}{2\Phi(x, y, z)}(1 + x'^2 + y'^2)\,. \tag{6}$$

On arrive finalement aux expressions suivantes, en négligeant les termes d'ordre supérieur au 3e:

cas S
$$\begin{cases} x'' + \beta^2 kx = -\beta^2\left[kx(x'^2 + y'^2) - \dfrac{k'x'}{2}(x^2 - y^2) + \beta^2k^2x(x^2 - y^2) - \dfrac{k''}{6}x^3\right] \\ y'' - \beta^2 ky = +\beta^2\left[ky(x'^2 + y'^2) + \dfrac{k'y'}{2}(x^2 - y^2) + \beta^2k^2y(x^2 - y^2) - \dfrac{k''}{6}y^3\right] \end{cases} \tag{7}$$

cas D.P
$$\begin{cases} x'' + \beta^2 kx = -\beta^2\left[kx(x'^2 + y'^2) - \dfrac{k'x'}{2}(x^2 - y^2 - a^2) + \beta^2k^2x(x^2 - y^2 - a^2) - k''x\left(\dfrac{x^2}{6} - \dfrac{a^2}{4}\right)\right. \\ \qquad\qquad \left. - 2\lambda kx\left(\dfrac{x^2 - 3y^2}{a^2}\right)\right] \\ y'' - \beta^2 ky = +\beta^2\left[ky(x'^2 + y'^2) + \dfrac{k'y'}{2}(x^2 - y^2 - a^2) + \beta^2k^2y(x^2 - y^2 - a^2) - k''y\left(\dfrac{y^2}{6} + \dfrac{a^2}{4}\right)\right. \\ \qquad\qquad \left. - 2\lambda ky\left(\dfrac{3x^2 - y^2}{a^2}\right)\right] \end{cases} \tag{8}$$

et une équation du même type dans le cas D.N.

La valeur de β^2 utilisée ici est donnée dans tous les cas par

$$\beta^2 = \frac{1}{a^2}\frac{\phi_1}{\phi_0^*} \tag{9}$$

5.2. CALCUL DES ABERRATIONS

Pour intégrer les équations précédentes, on considère les aberrations comme de faibles perturbations apportées aux trajectoires du premier ordre. On pose

$$\begin{aligned} x_3 &= x + \varepsilon\,, & x_3' &= x' + \varepsilon' \\ y_3 &= y + \eta\,, & y_3 &= y' + \eta' \end{aligned} \tag{10}$$

où x et y, x' et y' sont les solutions des équations sans second membre =

$$\begin{cases} x'' + \beta^2 k x = 0 \\ y'' - \beta^2 k y = 0 \end{cases} \tag{11}$$

et x_3, y_3 les solutions des équations complètes du 3e ordre.

On peut alors, pour chaque valeur de z, calculer le second membre des équations précédentes, en y portant les valeurs de x et y. On arrive alors des relations du type:

$$\begin{cases} (x + \varepsilon)'' + (x + \varepsilon)\beta^2 k = -\beta^2 P(z) \\ (y + \eta)'' - (y + \eta)\beta^2 k = +\beta^2 Q(z) \end{cases} \tag{12}$$

soit finalement:

$$\begin{cases} \varepsilon'' + \beta^2 k \varepsilon = -\beta^2 P(z) \\ \eta'' - \beta^2 k \eta = +\beta^2 Q(z) \end{cases} \tag{13}$$

($-\beta^2 P(z)$ et $\beta^2 Q(z)$ sont les seconds membres de (7) ou (8)).

Ces équations sont valables dans une lentille où zOx est le plan convergent pour la particule incidente. Dans la 2e lentille d'un doublet il faut, dans chaque equation, remplacer $+\beta^2$ par $-\beta^2$ et $+a^2$ par $-a^2$.

5.3. RESULTATS POUR UN DOUBLET SYMETRIQUE

Le calcul a été effectué pour comparer les résultats, d'une part aux résultats obtenus avec un doublet magnétique, d'autre part aux résultats expérimentaux, à l'aide d'une machine électronique IBM 650 pour le doublet symétrique (Q_1 et Q_2 ont la même excitation, et $O_1O_2 = 50$ cm) avec $\beta = 2\ \mathrm{m}^{-1}$ et un faisceau creux incident parallèle à l'axe, de rayon $R_0 = 3$ cm

5.3.1. *Excitation symétrique*

Les quatre trajectoires calculées sont définies à l'entrée de Q_1 par

$$\begin{cases} x_0 = & 3\ \mathrm{cm} & 2.4495 & 1.7319 & 0 \\ y_0 = & 0 & 1.7319 & 2.4495 & 3 \end{cases}$$

$$\text{et} \quad x'_0 = 0\,, \qquad y'_0 = 0\,.$$

Le calcul au premier ordre fournit la position des 2 focales. Celle du plan convergent-divergent, est située dans le plan yOz, en $z_1 = 220.95$ cm et celle du plan divergent-convergent, dans le plan xOz en $z_2 = 527.07$ cm. Les plans z_1 et z_2 sont donc les plans images de Gauss du doublet, correspondant à un point objet situé à l'infini. La distance focale calculée est, dans ces conditions: $F_x = F_y \simeq 3.6$ m.

En tenant compte de l'aberration d'ouverture, les pseudo-focales sont situées en réalité en avant des plans de Gauss en $(z_1)_3 = 216.55$ cm et $(z_2)_3 = 509$ cm. Leur forme est donnée fig. 9b, et, en s'éloignant des lentilles, la section du faisceau prend successivement les formes a) b) c) d) de la figure 9, contrairement au cas des lentilles magnétiques où l'ordre est inversé $\simeq$ l'aberration des lentilles électrostatiques symétriques est de signe contraire à celle des lentilles magnétiques, ce qui est conforme à l'expérience. On définit le taux d'aberration transversale τ à partir de la figure 9b

$$\tau = \frac{\delta}{R_0}$$

et on trouve, pour $\beta = 2\ \mathrm{m}^{-1}$

$$1^{\mathrm{ere}}\ \text{focale}: \tau_x = 0.7 \times 10^{-2} \qquad \text{soit } \frac{\tau_y}{\tau_x} \approx 3\ .$$
$$2^{\mathrm{e}}\ \text{focale}\ \tau_y = 2.04 \times 10^{-2}$$

Les expériences ont conduit à la valeur $\tau_x \simeq 0.8 \times 10^{-2}$ (voir § 4.1.2).

Les lentilles magnétiques avaient donné $\tau_x = 0.5 \times 10^{-2}$, c'est-à-dire une valeur légèrement inférieure[1]).

5.3.2. *Excitation dissymétrique positive*

Le calcul a été effectué en 2 temps

1) en négligeant dans l'expression du potentiel $\Phi(x, y, z)$ le terme à symétrie octopolaire, pour juger de l'importance des aberrations supplémentaires apportées par le terme à symétrie de révolution. On trouve

$$\tau_x \approx 0.71 \times 10^{-2} \qquad \tau_y \approx 2.1 \times 10^{-3}$$

c'est-à-dire des valeurs identiques aux précédentes.

Le sens de l'aberration ainsi calculée est identique à celui du cas symétrique, ce qui est contraire aux résultats expérimentaux. Le terme a symétrie de révolution n'apporte donc pas d'aberration supplémentaire et son influence se limite aux propriétés optiques du premier ordre.

2. en tenant compte du terme octopolaire avec $2\lambda = 0.5 \times 10^{-2}$. L'aberration calculée *change de sens, conformément à l'expérience* et on obtient:

$$\tau_x = 1.4 \times 10^{-2}$$
$$\tau_y = 1.2 \times 10^{-2}\ .$$

Ces résultats sont très proches des résultats expérimentaux, qui ont fourni $\tau_x \approx 10^{-2}$. On voit ici l'influence primordiale du terme à symétrie octopolaire; c'est bien lui qui intervient pour la correction de l'aberration en fonctionnement partiellement dissymétrique.

6. Conclusion

Nous avons étudié les propriétés optiques, et en particulier les aberrations d'ouvertures de lentilles quadrupolaires électrostatiques.

Cette étude montre que leurs aberrations propres, en excitation symétrique, sont un peu supérieures à celles des lentilles magnétiques de mêmes caractéristiques géométriques, et de signe contraire. La possibilité d'introduire une certaine dissymétrie dans l'alimentation permet de réduire considérablement l'aberration d'ouverture; cette méthode de correction, qui n'a pas son équivalent dans le cas magnétique, conserve les caractéristiques géométriques des lentilles et n'introduit pas de termes d'ordre supérieur dans la topographie du champ.

Nous donnons également une méthode de calcul des aberrations du 3e ordre dans un système quadrupolaire, dans tous les cas d'excitation. Les calculs effectués sur un doublet astigmatique avec les équations que nous avons déterminées sont en très bon accord avec l'expérience, et montrent l'importance fondamentale des potentiels correcteurs à symétrie octopolaire.

Ce travail a été effectué au Laboratoire d'Electronique de la Faculté des Sciences de Paris, en liaison avec la division du Synchrotron à protons du CERN (Genève). Nous sommes heureux de remercier Monsieur J. B. Adams, Directeur Général du CERN, et Monsieur P. Lapostolle avec qui nous avons eu de fructueuses discussions tout au long de cette étude.

NUCLEAR INSTRUMENTS AND METHODS 13 (1961) 356–358; NORTH-HOLLAND PUBLISHING CO.

PRECISION MEASUREMENTS OF NUCLEAR g-FACTORS BY THE TIME-TO-PULSE-HEIGHT CONVERTER METHOD

ECKART MATTHIAS and TORSTEN LINDQVIST

Institute of Physics, University of Uppsala, Uppsala

Received 11 August 1961

A method is suggested where the differential angular correlation technique is used in combination with a time-to-pulse-height converter and a multi-channel analyzer. In this way it is possible to study carefully how the angular correlation pattern varies with the time during a precession caused by an external magnetic field. As the precession can be followed for several turns the accuracy of the g-factor measurement is correspondingly higher.

Nuclear g-factors of excited states can be measured by studying the behaviour of the angular correlation of a gamma cascade in an externally applied magnetic field[1,2]).

The rotation and attenuation of the angular correlation pattern give an information about the quantity $\omega_L \tau_N$, where $\omega_L = (g \cdot H/\hbar)\, \mu_n$ is the Larmor frequency of the spin axis precession and τ_N is the life time of the excited state. With the knowledge of τ_N and the magnetic field strength H, the nuclear g-factor can be obtained.

Corresponding to the experimental technique, one can distinguish between two methods of measuring the angular correlation. If the resolving time, $2\tau_0$, of the coincidence system is long compared to the mean life time, i.e. $2\tau_0 \gg \tau_N$, the integral correlation is obtained. If this method is used for g-factors measurements the possible rotation angle $\Delta\theta$ is $0 < \Delta\theta < \pi/4$ and the attenuation factor $1/[1 + (k \cdot \omega_L \tau_N)^2]$ destroys the anisotropy for high magnetic fields.

The integral correlation method has been used by several groups and has lead to valuable information about the magnetic properties of nuclear excited states. However, the accuracy of the method is unsatisfactory for drawing any definite conclusions by comparing with theoretical predictions. The limits of error in the experimental measurements are of the order of 10% and it is very difficult to get them smaller than 5% even in the most favourable cases. There are mainly two reasons for this situation. Firstly, the experimentally determined perturbation—really a second order effect—is obtained as a difference between two experimental angular correlations. In other words, one has to measure the rotation of the angular correlation pattern by the angle $\Delta\theta \simeq \omega_L \tau_N$. With detectors of practical size such a rotation may be obtained to a precision of about two degrees, which for a typical rotation of $\Delta\theta \approx 40°$ gives a limiting accuracy of 5%.

Secondly, in each case where the mean life time τ_N permits the measurement of the g-factor, the angular correlation can also be perturbed by internal electric or/and magnetic fields[3]), originating from a certain source structure. Thus, the measurement of the pure magnetic interaction strength, ω_L, requires either the elimination of internal fields through a suitable choice of source structure or a separate measurement of the internal field interaction, both procedures are difficult to realize.

The second method, where $2\tau_0 \ll \tau_N$, is called the differential method and seems to offer a possibility to increase the accuracy. In spite of this fact up to now this method has not been used for determination of g-factors, as far as the authors know. The apparent advantage of the differential method is

[1]) R. M. Steffen, Advances in Physics 4 (1955) 293.

[2]) E. Heer and T. B. Novey, Solid State Physcis, Vol. 9 (Academic Press Inc., New York, 1959) p. 199

[3]) A. Abragam and R. V. Pound, Phys. Rev. 92 (1953) 943.

that the correlation pattern will not be smeared out even for large rotation angles $\Delta\theta$. Thus, as the absolute error in the determination of $\Delta\theta$ is independent of the size of $\Delta\theta$, a large $\Delta\theta$ means a small relative limit of error. This fact was used in the famous "g – 2" experiment[4]) at CERN for measuring the magnetic moment of the μ-meson.

Differential measurements with an ordinary fast-slow coincidence system do not work because of the low coincidence counting rate and, in the case of very short life times, because of difficulty in obtaining $2\tau_0 \ll \tau_N$. However, with the help of a time-to-pulse-height converter in combination with a multichannel analyzer the first of these difficulties can be overcome and one obtains an ideal tool for detecting the differential angular correlation.

The measurement of the differential angular correlation means to investigate the time spectrum $C(\theta, t)$ of the coincidence counting rate given by

$$C(\theta, t) = \text{const. exp } (-t/\tau_N) \cdot W(\theta, t) \qquad (1)$$

where θ is the angle between the detectors, the exponential factor takes the life time of the excited state into account and $W(\theta, t)$ is the differential correlation function.

With reference to eq. (1) it has been pointed out by Simms and Steffen[5]) that life time measurements can be falsified by an internal perturbation, making the correlation function time-dependent. This time dependency even when caused by external fields can be used to follow the Larmor precession over several periods and thus obtain a large rotation angle $\Delta\theta$, which will, as mentioned above, increase the accuracy in the measurement of $\Delta\theta$.

The differential correlation perturbed by an external magnetic field applied perpendicular to the plane of the detectors is given by[2])

$$W(\theta, t) = \sum_k A_k P_k \, [\cos (\theta - \Delta\theta)] \qquad (2)$$

where

$$\Delta\theta = \omega_L \, t = 2\pi \frac{t}{\tau_L} \qquad (3)$$

and τ_L is the time for one turn of the spin axis rotation. From equations (2) and (3) is obvious that, for a fixed angle θ, the differential correlation function is reproduced with a period of $t = \lambda\tau_L$, where λ is an integer.

If now the time-to-pulse-height converter is adjusted so that the resolving time is very small compared to the mean life time τ_N, it can be seen

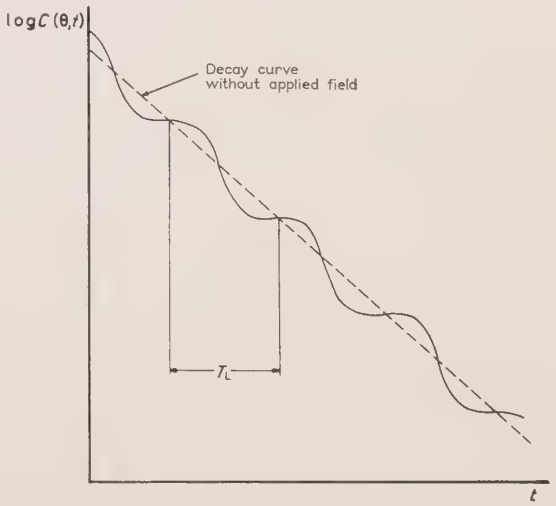

Fig. 1. Modulated decay curve. Modulation caused by the spin axis precession in the external magnetic field. T_L = time for one half turn of precession.

from eqs. (1) and (2) that the correlation function $W(\theta, t)$ will modulate the exponential decay pattern with a period, given by the Larmor frequency ω_L. The amplitude of this modulation is proportional to the anisotropy of the angular correlation. In the case of dominant A_2-term, the modulation amplitude will have two maxima and two minima during one turn of the spin axis rotation; if the angular correlation is given mainly by the A_4-term, the number of maxima and minima is doubled. The theoretical behaviour of the experimental decay curve when modulated of the static perturbing interaction can be seen in fig. 1. The main advantage with this method is, as already mentioned, the fact that the spin axis rotation can be followed for several turns and thus the total $\Delta\theta$ is large. As a consequence the determination of $\Delta\theta$ can be done with high accuracy. Another advantage is the simple experimental set up required. The detectors are in fixed positions and the angle between them does not have to be known with high precision. In

[4]) G. Charpack *et al.*, Phys. Rev. Letters **6** (1961) 128.

[5]) P. C. Simms and R. M. Steffen, Phys. Rev. **108** (1957) 1459.

some extreme cases only one detector will be sufficient for the experiment. Furthermore, the measurements are not affected by time independent effects as e.g. scattering.

As in the integral method internal perturbations in the source may appear superposed on the Larmor precession[3]). The perturbing interaction can be of static or time-dependent nature. In the first case the time spectrum also shows a periodic behaviour, which means that this interaction can be studied separately and corrected for when the external field is applied. In the second case the time-dependent interaction will vary the exponential decay pattern. However, it will not smear out or falsify the periodic modulation pattern caused by the external field, ϕ except for a damping of the modulation amplitude.

To summarize, the differential method can be performed with liquid sources as well as with solid sources. The internal interaction strength, however should not be strong compared to the magnetic dipole interaction ω_L.

The range of life times to be considered for the differential method depends on various parameters. A lower limit can be estimated in the following way. With an ordinary detector geometry a sector of about $\pi/5$ is "watched" by each detector. The highest efficiency is obtained if the prompt resolving curve of the coincidence circuit $2\tau_0$ had a width corresponding to $\pi/5$, i.e. the time required by the rotating nucleus to pass through the sector $\pi/5$. If it is required that the nucleus should rotate at least half a turn (π) per half life it turns out that the lower limit of life times would be of the order of $10\tau_0$.

The upper limit will probably be determined by the presence of depolarizing effects of relaxation processes and the ratio of total to chance coincidences.

Note added in proof: By a private communication of Dr. A. Hrynkiewicz the authors were informed, that the proposed method already has been used for the determination of the magnetic moments of the 81 keV state in Cs^{133} and the 482 keV state in Hf^{181}. The measurements had been carried out by M. Deutsch, A. Hrynkiewicz and R. F. Stiening in the Laboratory for Nuclear Science, MIT, Cambridge.

NUCLEAR INSTRUMENTS AND METHODS 13 (1961) 359–360; NORTH-HOLLAND PUBLISHING CO.

INEXPENSIVE TARGET CHAMBER WITH PORT MOVABLE THROUGH ZERO DEGREES UNDER VACUUM†

J. R. ERSKINE and C. P. BROWNE

University of Notre Dame, Notre Dame, Indiana

Received 31 July 1961

A simple and inexpensive target chamber with an exit port that can be moved under vacuum through angles from — 5 to 140 degrees is described. The movable seal is made by a spring steel tape sliding against a rubber gasket. A novel method of moving this tape is presented. The chamber was built for use with a broad-range spectrograph but would be suitable for use with other detecting devices.

1. Introduction

A target chamber with an exit port that can be moved under vacuum through angles from — 5 to 140 degrees has been built for use with a broad-range magnetic spectrograph. This target chamber is less complicated and less expensive to build than other target chambers reported in the literature that have this feature of continuous rotation through zero degrees. The most difficult part to construct, the central body, was machined by a commercial shop for $ 150.00. Another advantage is that the body of the chamber is fixed as are the top and bottom cover plates and these are free for the mounting of equipment.

Conventional chambers allowing rotation under vacuum usually have the axis of the exit port set at an angle to the axis of the input port thus limiting the minimum angle of observation. Chambers have been made which allow observation at zero degrees but they require either, that the axis of the entrance port not be in a horizontal plane, or that the detector not rotate in a horizontal plane. For use with a heavy spectrograph and a horizontal beam from an accelerator, these are serious disadvantages. A chamber without these disadvantages has been reported, but it is relatively complicated and expensive[1]). A target chamber with a sliding seal based on the principle of the present chamber and having an exit port large enough to accomodate a photomultiplier tube has been built[2]) but it required rather difficult and tedious spot welding and the method of rotating the seal under vacuum was not described.

Although the principle of operation of the present target chamber is the same as that of others previously used with broad-range spectrographs[3]), as no detailed description of these other chambers has appeared and as considerable interest has developed in this chamber. the following brief description is thought worthwhile. A novel method of moving the exit port is presented. The chamber can be rotated under vacuum independently of the spectrograph and would be equally convenient for use with other apparatus.

2. Description

The sliding vacuum-seal mechanism is shown schematically in fig. 1. Here, the chamber itself is indicated by dotted lines, because details of the chamber are irrelevant to this discussion. A 2.86 cm wide slot, extending for 158 degrees around the 28.26 cm diameter target chamber, is milled through the 1.90 cm aluminum wall. This slot is covered by

† This work has been supported in part by the joint program of the Office of Naval Research and the U.S. Atomic Energy Commission.

Now at the Laboratory for Nuclear Science, Massachusetts Institute of Technology, Cambridge, Massachusetts.

[1]) R. L. Clarke, Nucl. Instr. and Meth. **3** (1958) 233.

[2]) F. I. Loucks, Rev. Sci. Instr. **28** (1957) 468.

[3]) C. P. Browne and W. W. Buechner, Rev. Sci. Instr. **27** (1956) 899;
S. Hinds and R. Middleton, Proc. Phys. Soc. (London) **74** (1959) 196.

a spring steel tape 10 cm wide and 0.25 mm thick. The seal is made with a 0.353 cm "rotary seal compound" 0-ring set into a 0.261 cm deep 0-ring groove around the edge of the slot. The 0-ring is lubricated with "Apiezon N" vacuum grease. A pair of 5.0 cm diameter rollers press the tape against the 0-ring at both ends of the slot. These rollers are supported by ball bearings mounted in the top and bottom cover plates of the chamber which have a larger diameter than the body of the chamber in order to take these bearings mounts. The bearing mounts have a screw adjustment in the radial direction to permit adjusting the squeeze on the ends of the 0-ring. For easy access to the interior of the chamber, without disturbing the roller adjustment, the central part of the top cover is made as a separate, removable plate, sealed to the outer portion of the cover with an 0-ring. The curvature of the scattering chamber, the stiffness of the spring steel, and the width of the tape combine to keep the tape from being pushed through the slot by the outside air pressure. An exit path is provided through a flexible metal bellows fastened around a hole in the steel tape with an 0-ring seal.

The observation angle is changed by pulling the tape one way or the other with a system of cables and the length of the tape is sufficient for the angular range required. The sheaves, cable drum, and worm-gear reducer for this system are supported by a welded aluminum channel frame (not shown in fig. 1) bolted to the bottom of the chamber. The entire assembly may then be insulated from the support post so that the beam current into the chamber can be measured. To make the frame compact, it is desirable to make the device for attaching the cables to the tape as small as possible. In the scheme used, the end of the tape is clamped between two 1.90 cm × 1.59 cm × 10 cm steel pieces which also clamp the cable in a conical hole. A small steel insert is embedded in the center of the cable to spread the strands and wedge them in the hole. The cable is 0.635 cm diameter wire rope, the sheaves are 5.72 cm diameter, and the gear box has a ratio of 30:1. The cable tension required to move the tape with a vacuum in the chamber is about 30 kg.

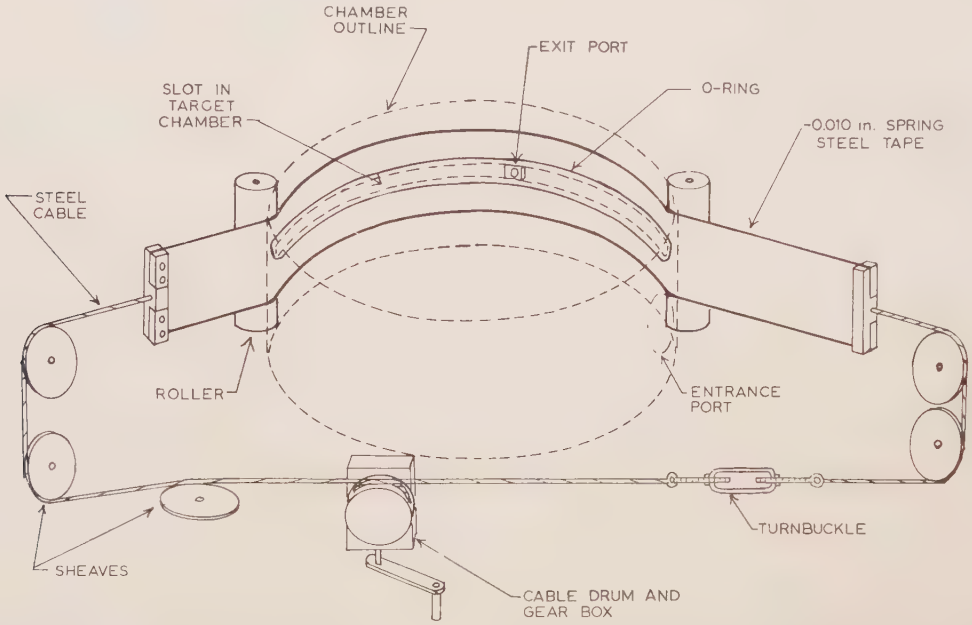

Fig. 1. Schematic drawing of target chamber showing the sliding seal made with a spring steel tape and the mechanism for moving the exit port of the target chamber. The angle of observation can be changed without breaking the vacuum.

To allow moving the tape without leakage of air, it is necessary to keep the tape and 0-ring clean and to have the rollers properly adjusted. Too much compression with the rollers causes rapid wear of the 0-ring. Two years experience with the chamber has shown it to be efficient and easy to operate.

AUTHOR INDEX

Adler, A., M. Palmai and V. Perez-Mendez, 100 Mc/s tunneldiode discriminator and pulse-shaper 197
Alexander, T. K. and F. S. Goulding, An amplitude-insensitive system that distinguishes pulses of different shapes 244
Alexander, T. K. and D. R. Heywood, A twenty-Mc/s transistor decade scaler 83
Anderson, Carl E., D. A. Bromley and M. Sachs, Simultaneous nuclide identification and energy measurement of nuclear reaction products 238
Anderson, D. W. and J. McKenzie, A propane bubble chamber with mechanical expansion 231
Armbruster, R., *see* Gorodetzky
Azuma, R. E., *see* Currie

Batchelor, R., W. B. Gilboy, J. B. Parker and J. H. Towle, The response of organic scintillators to fast neutrons 70
Berényi, D. and Gy. Máthé, Experiences in the use of scintillation detector in a β-spectrometer of toroid-sector type 161
Berglund, S. and S. Svennerstedt, Some characteristics of a toroidal pinch with a reversed field 201
Blosser, H. G. and M. M. Gordon, Performance estimates for injector cyclotrons 101
Bok, J. et J. P. Noel, Diode a barrière de surface pour la détection de particules nucléaires 206
Bret, Georges C. and Erwin F. Shrader, Fast tunnel diode circuits for NaI(Tl) detectors 177
Bromley, D. A., *see* Anderson, Carl E.
Browne, C. P., *see* Erskine
Bruninx, E. and G. Rudstam, Electro-spraying: A method of making samples for β counting allowing accurate correction for self-scattering and self-absorption 131

Cedarlund, R., A. Horn and M. Scolnick, Solid-state detector for monitoring 14-MeV neutron production 305
Chrien, R. E., *see* Zimmerman
Cindro, N., A possible method for distinguishing charged particles with semiconductor detectors (Letter to the Editor) 99
Culwick, B. B. and S. J. Goldsack, Measuring machine for bubble chamber photographs 118
Currie, W. M., R. E. Azuma and G. M. Lewis, Measurements of instrumental time delay and resolution in a fast coincidence system 215

Daly, N. R., *see* Wilson
Deckers, Hans, Calculation of recoil spectra induced by fast neutron spectra in nuclear emulsions 224
De Vries, L. J. and F. Udo, A fast pulse-shape discriminator with applications as a spectrometer and sensitive monitor for 1–30 MeV neutrons 153
Dodd, W. P., G. A. Doran, J. B. Kinson, L. Riddiford and B. Tallini, Operation of a 9-inch bubble chamber with deuterium 127
Doke, Tadayoshi, *see* Ogawa
Doran, G. A., *see* Dodd
Doran, G. A. and M. Jobes, An automatic track following device 124

Erskine, J. R. and C. P. Browne, Inexpensive target chamber with port movable through zero degrees under vacuum 359

Fink, R. W., *see* Kantele
Firk, F. W. K., G. G. Slaughter and G. J. Ginther, An improved Li^6-loaded glass scintillator for neutron detection 313
Fuketa, Toyojiro, Paired-chamber type pile oscillator 35

Gersch, H. U., Berechung der Polschuhoberflächen eines magnetischen Teilchen spektrometers 297
Gilboy, W. B., *see* Batchelor
Ginther, G. J., *see* Firk
Goldsack, S. J., *see* Culwick
Gopalan, K. and E. S. Rajagopal, An instantaneous pulse frequency meter for random pulses 253
Gordon, M. M., *see* Blosser
Gorodetzky, S., A. Muser, J. Zen et R. Armbruster, Sur un circuit rapide de mise en forme à seuil règlable utilisant des diodes tunnel. 282
Goulding, F. S., *see* Alexander
Gupta, S. L. and N. K. Saha, Spark counter as a fast pulse generator 258

Hardy, R. W. D., *see* Wilson
Hazoni, Y., A fast flip-flop circuit utilizing tunnel diodes (Letter to the Editor) 95
Heywood, D. R., *see* Alexander
Hickman, G. D., A miniature fast fission counter 190
Horn, A., *see* Cedarlund
Howe, F. A., *see* Muggleton

Infante, C., A constant input impedance plug-in for the Tektronix 581 oscilloscope (Letter to the Editor) . . 264

Jarczyk, L., H. Knoepfel, J. Lang, R. Müller and W. Wölfli, The nuclear reactor as a high intensity source for discrete gamma rays up to 11 MeV . . . 287
Jennings, R. E. and R. E. Rand, Elimination of the dead space between channels in a Hutchinson-Scarrott pulse height analyser (Letter to the Editor) 97
Jobes, M., *see* Doran

Kantele, J. and R. W. Fink, Coincidence summing and nonlinearity studies with a two-crystal scintillation gamma spectrometer 141

KERN, JEAN, Détecteur G.M. pour un spectromètre bêta 50
KINSON, J. B., *see* DODD
KNOEPFEL, H., *see* JARCZYK
KONRAD, M. and B. TURKO, Sorting of two coincident pulses according to their amplitudes 29

LAMDEN, R. J., A random pulse generator with provision for excursions 247
LANG, J., *see* JARCZYK
LARSSON, E. INGEMAR, *see* MCCALL
LEWIS, G. M., *see* CURRIE
LINDQVIST, TORSTEN, *see* MATTHIAS
LINDQVIST, TORSTEN, *see* SCHNEIDER

MÁTHÉ, GY., *see* BERÉNYI
MATTHIAS, ECKART and TORSTEN LINDQVIST, Precision measurements of nuclear *g*-factors by the time-to-pulse-height converter method 356
MARTIN, G. R., The estimation of the resolving time of a counting apparatus (Letter to the Editor) 263
MCCALL, RICHARD C. and E. INGEMAR LARSSON, A low priced automatic printout system for the Hutchinson Scarrott analyser (Letter to the Editor) 92
MCCORMACK, J. D., *see* MCCORMICK
MCCORMICK, R. D. and J. D. MCCORMACK, Hydrogen and carbon target preparation for a positive ion accelerator 147
MCKENZIE, J., *see* ANDERSON, D. W.
MUGGLETON, A. H. F. and F. A. HOWE, The preparation of thin self supporting boron films 211
MÜLLER, R., *see* JARCZYK
MUNRO, R., *see* WILSON
MUSER, A., *see* GORODETZKY

NILSSON, GÖSTA, Improved fission counting method for uranium isotope analysis 183
NOACK, C. und W. ROETHER, Ein Kabelverstärker für Impulse grosser Amplitude 261
NOEL, J. P., *see* BOK

OGAWA, IWAO, TADAYOSHI DOKE and MASAHIRO TSUKUDA, The double-grid ionization chamber 169
OLSEN, W. C., *see* ZIMMERMAN

PALEVSKY, H., *see* ZIMMERMAN
PALMAI, M., *see* ADLER
PARKER, J. B., *see* BATCHELOR
PEREZ-MENDEZ, V., *see* ADLER
PETERS, C. W. and A. L. SNYDER, Optimum location of BF_3 counters in a neutron moderator 309

RAJAGOPAL, E. S., *see* GOPALAN
RAND, R. E., *see* JENNINGS
REISER, MARTIN, Ioneneinfang und Anfangsbahnen im Isochron-Zyklotron Karlsruhe 55
RIDDIFORD, L., *see* DODD
ROETHER, W., *see* NOACK
RUDSTAM, G., *see* BRUNINX

SACHS, M., *see* ANDERSON, CARL E.
SAHA, N. K., *see* GUPTA
SAHA, N. K., *see* SINGH
SCHNEIDER, WERNER and TORSTEN LINDQVIST, Automatic analysis of beta-ray spectra 21
SCOLNICK, M., *see* CEDARLUND
SEPTIER, A. et J. VAN ACKER, Les lentilles quadrupolaires électrostatiques 335
SHRADER, ERWIN F., *see* BRET
SINGH, GURBAX and N. K. SAHA, A new design of a multiple-wire spark counter and some studies with the single wire-plate spark counter 321
SINGH, P. P., *see* ZIMMERMAN
SLAUGHTER, G. G., *see* FIRK
SNYDER, A. L., *see* PETERS
SPROKEL, G. J., An automatic sample changer 330
SVENNERSTEDT, S., *see* BERGLUND
SWEETMAN, D. R., The achievement of very high pumping speeds in the ultra-high vacuum region 317

TALLINI, B., *see* DODD
TANAKA, EIICHI, A low background beta-ray scintillation spectrometer using a coincidence method with a Geiger counter 43
TOWLE, J. H., *see* BATCHELOR
TSUKUDA, MASAHIRO, *see* OGAWA
TURKO, B., *see* KONRAD

UDO, F., *see* DE VRIES

VAN ACKER, J., *see* SEPTIER

WESTCOTT, C. H., *see* ZIMMERMAN
WILSON, H. W., R. MUNRO, R. W. D. HARDY and N. R. DALY, A two stage mass spectrometer for nuclear physics applications 269
WÖLFLI, W., *see* JARCZYK

ZEN, J., *see* GORODETZKY
ZIMMERMAN, R. L., H. PALEVSKY, R. E. CHRIEN, W. C. OLSEN, P. P. SINGH and C. H. WESTCOTT, The U.S.-Canadian fast chopper installation at Chalk River 1

SUBJECT INDEX

Accelerators and Reactors

The U.S.-Canadian fast chopper installation at Chalk River, R. L. Zimmerman, H. Palevsky, R. E. Chrien, W. C. Olsen, P. P. Singh and C. H. Westcott . . . 1
Ioneneinfang und Anfangsbahnen im Isochron-Zyklotron Karlsruhe, Martin Reiser . . . 55
Performance estimates for injector cyclotrons, H. G. Blosser and M. M. Gordon . . . 101
Hydrogen and carbon target preparation for a positive ion accelerator, R. D. McCormick and J. D. McCormack . . . 147
Simultaneous nuclide identification and energy measurement of nuclear reaction products, Carl E. Anderson, D. A. Bromley and M. Sachs . . . 238
The nuclear reactor as a high intensity source for discrete gamma rays up to 11 MeV, L. Jarczyk, H. Knoepfel, J. Lang, R. Müller and W. Wölfli . . . 287
Les lentilles quadrupolaires électrostatiques, A. Septier et J. van Acker . . . 335

Detectors

Détecteur G.M. pour un spectromètre bêta, Jean Kern . . . 50
The response of organic scintillators to fast neutrons, R. Batchelor, W. B. Gilboy, J. B. Parker and J. H. Towle . . . 70
Operation of a 9-inch bubble chamber with deuterium, B. Tallini . . . 127
Experiences in the use of scintillation detector in a β-spectrometer of toroid-sector type, D. Berényi and Gy. Máthé . . . 161
The double-grid ionization chamber, Iwao Ogawa, Tadayoshi Doke and Masahiro Tsukuda . . . 164
Improved fission counting method for uranium isotope analysis, Gösta Nilsson . . . 183
A miniature fast fission counter, G. D. Hickman . . . 190
Diode a barrière de surface pour la détection de particules nucléaires, J. Bok et J. P. Noel . . . 206
A propane bubble chamber with mechanical expansion, D. W. Anderson and J. McKenzie . . . 231
Solid-state detector for monitoring 14-MeV neutron production, R. Cedarlund, A. Horn and M. Scolnick . . . 305
Optimum location of BF_3 counters in a neutron moderator, C. W. Peters and A. L. Snyder . . . 309
An improved Li^6-loaded glass scintillator for neutron detection, F. W. K. Firk, G. G. Slaughter and R. J. Ginther . . . 313
A new design of a multiple-wire spark counter and some studies with the single wire-plate spark counter, Gurbax Singh and N. K. Saha . . . 321

Instruments and Methods for Nuclear Spectroscopy

Automatic analysis of beta-ray spectra, Werner Schneider and Torsten Lindqvist . . . 21
A low background beta-ray scintillation spectrometer using a coincidence method with a Geiger counter, Eiichi Tanaka 43
Electro-spraying: A method of making samples for β counting allowing accurate correction for self-scattering and self-absorption, E. Bruninx and G. Rudstam . . . 131
Coincidence summing and non-linearity studies with a two-crystal scintillation gamma spectrometer, J. Kantele and R. W. Fink . . . 141
The preparation of thin self-supporting boron films, A. H. F. Muggleton and F. A. Howe . . . 211
Calculation of recoil spectra induced by fast neutron spectra in nuclear emulsions, Hans Deckers . . . 224
A two stage mass spectrometer for nuclear physics applications, H. W. Wilson, R. Munro, R. W. D. Hardy and N. R. Daly 269
Berechnung der Polschuhoberflächen eines magnetischen Teilchen spektrometers, H. U. Gersch . . . 297
The achievement of very high pumping speeds in the ultra-high vacuum region, D. R. Sweetman . . . 317
An automatic sample changer, G. J. Sprokel . . . 330
Precision measurements of nuclear g-factors by the time-to-pulse-height converter method, Eckart Matthias and Torsten Lindqvist . . . 356
Inexpensive target chamber with port movable through zero degrees under vacuum, J. R. Erskine and G. P. Browne . 359

Instruments and Methods for High Energy Physics

Measuring machine for bubble chamber photographs, B. B. Culwick and S. J. Goldsack . . . 118

Letters to the Editor

A low priced automatic printout system for the Hutchinson-Scarrott analyser, Richard C. McCall and E. Ingemar Larsson . . . 9
A fast flip-flop circuit utilizing tunnel-diodes, Y. Hazoni . . . 9
Elimination of the dead space between channels in a Hutchinson-Scarrott pulse height analyser, R. E. Jennings and R. E. Rand . . . 9
A possible method for distinguishing charged particles with semiconductor detectors, N. Cindro . . . 9
The estimation of the resolving time of a counting apparatus, G. R. Martin . . . 26
A constant input impedance plug-in for the Tektronix 581 oscilloscope, C. Infante . . . 26

Nuclear Electronics

Sorting of two coincident pulses according to their amplitudes, M. Konrad and B. Turko . . . 2
Paired-chamber type pile oscillator, Toyojiro Fuketa . . . 3
A twenty-Mc/s transistor decade scaler, T. K. Alexander and D. R. Heywood . . . 8
An automatic track following device, G. A. Doran and M. Jobes . . . 12
A fast pulse-shape discriminator with applications as a spectrometer and sensitive monitor for 1–30 MeV neutrons, L. J. de Vries and F. Udo . . . 15
Fast tunnel diode circuits for NaI(Tl) detectors, Georges C. Bret and Erwin F. Shrader . . . 17
100 Mc/s tunnel-diode discriminator and pulse-shaper, A. Adler, M. Palmai and V. Perez-Mendez . . . 19
Measurements of instrumental time delay and resolution in a fast coincidence system, W. M. Currie, R. E. Azuma and G. M. Lewis . . . 21
An amplitude-insensitive system that distinguishes pulses of different shapes, T. K. Alexander and F. S. Goulding . . . 24
A random pulse generator with provision for excursions, R. J. Lamden . . . 24
An instantaneous pulse frequency meter for random pulses, K. Gopalan and E. S. Rajagopal . . . 25
Spark counter as a fast pulse generator, S. L. Gupta and N. K. Saha . . . 25
Ein Kabelverstärker für Impulse grosser Amplitude, C. Noack und W. Roether . . . 26
Sur un circuit rapide de mise en forme à seuil règlable utilisant des diodes tunnel, S. Gorodetzky, A Muser, J. Zen et R. Armbruster . . . 28

Plasma Physics

Some characteristics of a toroidal pinch with a reversed field, S. Berglund and S. Svennerstedt . . . 20

News Items

Conference on sector-focused cyclotrons (17–20 April, 1962) . . . 26
International conference on the physics of semiconductors (16–20 July, 1962) . . . 26

Book Reviews

Safe operation of critical assemblies and research reactors, IAEA, Vienna, 1961 (Torsten Lindqvist) . . . 26
Huber, P. and K. P. Meyer (editors) Proceedings of the international symposium on polarization phenomena of nucleons, Basel, July 4–8, 1960 (Arne Johansson) . . . 26
Gorter, C. J. (editor) Progress in low temperature physics, Volume III (O. Beckman) . . . 26
Chase, R. L. Nuclear pulse spectrometry (P. A. Tove) . . . 26
Nuclear propulsion. Bibliographical series No. 3, International Atomic Energy Agency, Vienna, 1961 (N. Robert Nilsson) 26
Regulations for the safe transport of radioactive materials, International Atomic Energy Agency, Vienna, 1961 (Börje Larsson) . . . 26
Hyder, H. R. McK. (editor) Progress in nuclear energy, Ser. II: Reactors, Volume 2 (Torsten Lindqvist) . . . 26
Small and Medium Power Reactors, Volume I, Conference Proceedings Vienna, 5–9 September 1960, IAEA, Vienna 1961, STI/PUB/30. Pp. 617, US $ 9.–, (Torsten Lindqvist) . . . 26
Kiefer, H. and R. Maushart, Überwachung der Radioaktivität in Abwasser und Abluft, (Teubner Verlagsgesellschaft, Stuttgart 1961), (Börje Larsson) . . . 26

402

DATE DUE

GAYLORD

PRINTED IN U.S.A.